Effects of Chromium and Silicon on Corrosion of Iron Alloys in Lead-Bismuth Eutectic

by

JEONGYOUN LIM

Submitted to the Department of Nuclear Science and Engineering
in partial fulfillment of the requirements for the degree of

DOCTOR OF SCIENCE IN NUCLEAR SCIENCE AND ENGINEERING

at the

MASSACHUSETTS INSTITUTE OF TECHNOLOGY

February 2006

©2006 Massachusetts Institute of Technology, All rights reserved.

Author:_____
Department of Nuclear Science and Engineering
September 19, 2005

Certified by:_____
Ronald G. Ballinger
Professor of Nuclear Science and Engineering
Professor of Materials Science and Engineering
Thesis Supervisor

Accepted by:_____
Dr. Ning Li
Project Leader, Lead-Alloy Coolant & Materials Development
Materials Science and Technology Division
Los Alamos National Laboratory
Thesis Reader

Accepted by:_____
Jeffrey A. Coderre
Associate Professor of Nuclear Science and Engineering
Chairman, Department Committee on Graduate Students

MASSACHUSETTS INSTITUTE OF TECHNOLOGY
OCT 12 2007
LIBRARIES

ARCHIVES

Effects of Chromium and Silicon on Corrosion of Iron Alloys in Lead-Bismuth Eutectic

by

Jeongyoun Lim

Submitted to the Department of Nuclear Science and Engineering
on September 19, 2005, in partial fulfillment of the requirements for the degree of

Doctor of Science in Nuclear Science and Engineering

ABSTRACT

The high power densities and temperatures expected for next generation nuclear applications, including power generation and transmutation systems, will require new types of heat transport systems to be economic. Present interest in heavy liquid metal coolants, especially in lead and lead-bismuth eutectic, originates from such requirements as increased heat removal capacity and enhanced safety features. However, corrosion of structural metals represents a major limiting factor in developing advanced liquid Pb-alloy coolant technology. In fact, the development of advanced structural and cladding alloys that are resistant to corrosion over a wide range of oxygen potentials in this environment would represent the enabling technology for these systems.

The goal of this research was to develop a class of Fe-Cr Si alloys that are resistant to corrosion in Pb and Pb alloys at temperatures of 600°C or higher. As a necessary part of this development effort, an additional goal was to further develop the fundamental understandings of the mechanisms by which corrosion protection is achieved.

A series of alloys based on the Fe-Cr-Si system were proposed as potential candidates for this application. These alloys were then produced and evaluated. The results of this evaluation verified the hypothesis that an Fe alloys with suitable levels of Cr (>12 wt%) and Si (> 2.5 wt%) will be protected by either a tenacious oxide film (over a wide range of oxygen potentials above the formation potential for Cr and Si oxides) or by a low solubility surface region (at low oxygen potentials)

Experimental results obtained from model alloys after lead-bismuth eutectic exposure at 600°C demonstrated the film formation process. The hypothesis that Si addition would promote the formation of a diffusion barrier was confirmed by the actual reduction of oxide thickness over time. The Si effect was magnified by the addition of Cr to the system. Based on a kinetic data assessment on the experimental results of Fe-Si and Fe-Cr-Si alloys, the synergetic alloying effect of Cr and Si was revealed. An improved understanding on the kinetic process and its dependence on the alloying elements has been achieved.

Thesis Supervisor: Ronald G. Ballinger
Title: Professor of Nuclear Engineering and Materials Science and Engineering

Table of Contents

Chapter 1: Introduction 12

1.1 Lead-Alloy Coolant Technology 12

1.1.1 Properties of Pb-alloy Coolants 13

1.1.2 Material Compatibility Issues of Pb-alloy Coolant Technology 14

1.1.3 Selection Guide for Candidate Materials 17

1.2 Objectives of Research 19

1.3 Outline and Keypoints 20

1.4 References 22

Chapter 2: Background 24

2.1 Thermodynamic Principles in Liquid Metal Corrosion 25

2.1.1 Solid-Liquid Metal System 25

2.1.2. Solubility of Oxygen in Liquid Pb-alloys 28

2.1.3 Principles of Oxygen Control in Liquid Pb-alloys 31

2.2 Kinetics of Liquid Metal Corrosion 39

2.2.1 Kinetic Process of Dissolution in Liquid Pb-alloys 39

2.2.2 Oxidation Characteristics of Iron Based Alloy 43

2.3 References 49

Chapter 3: Experimental Procedures 54

3.1 Material 54

3.2 System Description 57

3.3 Testing and Analysis Procedures 59

Chapter 4: Results 62

4.1 Samples Tested in the Cover Gas Condition 62

4.2 Dissolution of Elements 65

4.3 Corrosion Behavior of Fe-Cr Alloys 66
4.3.1 Fe-1%Cr 66
4.3.2 Fe-2.25%Cr 70
4.3.3 Fe-9%Cr 72
4.3.4 Fe-12%Cr 75
4.3.5 Fe-18%Cr 82
4.3.6 Summary of Fe-Cr Test Results 84
4.4 Corrosion Behavior of Fe-Si Alloys 85
4.4.1 Fe-2.55%Si and Fe-3.82%Si After 100-hour Test 85
4.4.2 Fe-1.25%Si, Fe-2.55%Si and Fe-3.82%Si After 300-hour Test 88
4.4.3 Summary of Fe-Si Test Results 90
4.5 Corrosion Behavior of Fe-Cr-Si alloys 91
4.5.1 Fe-2.25%Cr-0.5%Si and Fe-2.25%Cr-1.25%Si 91
4.5.2 Fe-12%Cr-0.5%Si 94
4.5.3 Fe-12%Cr-1.25%Si 96
4.5.4 Fe-18%Cr-0.5%Si 98
4.5.5 Fe-18%Cr-1.25%Si and Fe-18%Cr-2.55%Si 100
4.5.6 Summary of Fe-Cr-Si Test Results 107
4.6 References 108

Chapter 5: Discussion 109
5.1 Effect of Alloying on LBE Corrosion 110
5.1.1 External vs. Internal Oxidation (Fe-Cr alloys) 110
5.1.2 Internal and Grain Boundary Oxidation
(Fe-Si and Fe-Cr-Si with low Cr alloys) 120
5.1.3 Effect of Alloying Si (Fe-Cr-Si with high Cr alloys) 125
5.2 Summary of Experimental Results 127
5.3 References 129

Chapter 6: Conclusions and Future Work 131
6.1 Overall Summary 131

6.2 Conclusions 132
6.3 Contributions 132
6.4 Future Work 133

List of Figures

1-1	Pb-Bi phase diagram	13
1-2	Schematic of thermal gradient mass transfer in a liquid metal circuit	16
2-1	Isotherms of the Ternary Fe-Bi-Pb liquidus	27
2-2	Solubilities for Cr and Ni in liquid Pb, Bi and Pb-Bi eutectic (LBE)	28
2-3	Ellingham diagram for selected metal-metal oxide systems	33
2-4	Diagram showing corrosion behavior of steels in flowing oxygen-containing lead for 3000 h at 550°C	36
2-5	Effect of alloying elements on low alloy steel corrosion in Pb-Bi at 600°C and flow rate 6 m/s	38
2-6	Diffusion coefficients of O, Fe and Cr in liquid Pb-alloys	41
2-7	Variation of the mechanism of flow accelerated corrosion (FAC) as a function of the fluid velocity	42
2-8	The iron-oxygen phase diagram	43
2-9	Schematic showing the effect of chromium in Fe-Cr alloys on oxidation rate and oxide scale structure based on isothermal oxidation studies	46
2-10	Diffusion coefficients of selected iron based materials and oxides	48
3-1	Schematic diagram of experimental facility	59
4-1	Visual observation of samples tested in cover gas condition at 600°C	62
4-2	XRD patterns for oxide film formed on the Fe-18%Cr-2.55%Si sample tested in cover gas atmosphere	64
4-3	XPS survey spectra for Fe-18%Cr-2.55%Si sample tested in cover gas condition	64
4-4	XPS high-resolution spectra of (a) Cr and (b) Si obtained from Fe-18%Cr-2.55%Si tested in cover gas condition for 250 hours at 600°C	65
4-5	ICP-MS analysis data on solidified LBE bath after 100-hour 600°C test	66

4-6 SEM and EPMA results of Fe-1%Cr after exposure at 600°C for 100 hours 68

4-7 SEM and X-ray maps of Fe-1%Cr sample after exposure at 600°C for 250 hours 69

4-8 SEM image of Fe-1%Cr sample after exposure at 600°C for 500 hours 69

4-9 EPMA results on Fe-2.25%Cr sample after exposure at 600°C for 500 hours 70

4-10 SEM images of Fe-2.25%Cr material after exposure at 600°C for (a) 100 hours (b) 250 hours and (c) 500 hours 71

4-11 SEM images of Fe-9%Cr material, after exposure at 600°C for (a) 100 hours, (b) 300 hours, and (c) 500 hours 73

4-12 EPMA data of Fe-9%Cr material after exposure at 600°C for 100 hours 74

4-13 EPMA data of Fe-9%Cr material after exposure at 600°C for 300 hours 74

4-14 SEM and X-ray maps of Fe-9%Cr material after exposure at 600°C for 250 hours 75

4-15 SEM and EPMA results of Fe-12%Cr material after exposure at 600°C for 100 hours 76

4-16 SEM, EDX and EPMA results of Fe-12%Cr after exposure at 600°C for 250 hours 77

4-17 SEM images of Fe-12%Cr material after exposure at 600°C for (a) 300 hours and (b) 500 hours 78

4-18 XRD spectra of Fe-12%Cr material showing the existing phase peak after 500-hour, 600°C LBE exposure 80

4-19 XRD spectra of Fe-12%Cr material after exposure at 600°C for 500 hours 80

4-20 XPS survey spectra for Fe-12%Cr material after exposure at 600°C for 500 hours 81

4-21 XPS high-resolution spectra of (a) Fe and (b) Cr from Fe-12%Cr material after exposure at 600°C LBE for 500 hours 81

4-22 SEM image of Fe-18%Cr material after exposure at 600°C for 300 hours 83

4-23 SEM and EPMA results of Fe-18%Cr material after exposure at 600°C for 500 hours 83

4-24 SEM image and X-ray maps of Fe-18%Cr after exposure at 600°C for 250 hours 84

4-25 SEM and EPMA results of Fe-2.55%Si material after exposure at 600°C for 100 hours 86

4-26 SEM and EPMA results of Fe-3.82%Si material after exposure at 600°C for 100 hours 87

4-27 SEM and EPMA results of Fe-1.25%Si material after exposure at 600°C for 300 hours 88

4-28 SEM and EPMA results of Fe-2.55%Si material after exposure at 600°C for 300 hours 89

4-29 SEM and EPMA results of Fe-3.82%Si material after exposure at 600°C for 300 hours 90

4-30 SEM image of Fe-2.25%Cr-0.5%Si material after exposure at 600°C for 100 hours 92

4-31 SEM and EDX results of Fe-2.25%Cr-0.5%Si after exposure at 600°C for 250 hours 92

4-32 SEM image and X-ray maps of Fe-2.25%Cr-1.25%Si material after exposure at 600°C to LBE for 250 hours 93

4-33 SEM image of Fe-2.25%Cr-1.25%Si material after exposure at 600°C for 300 hours 93

4-34 SEM and EPMA results of Fe-12%Cr-0.5%Si after exposure at 600°C for 100 hours 94

4-35 SEM image and X-ray maps of Fe-12%Cr-0.5%Si after exposure at 600°C for 250 hours 95

4-36 SEM and EPMA results of Fe-12%Cr-0.5%Si after exposure at 600°C for 500 hours 95

4-37 SEM and EPMA results of Fe-12%Cr-1.25%Si after exposure at 600°C for 100 hours 96

4-38 SEM image and X-ray maps of Fe-12%Cr-1.25%Si after exposure at 600°C for 250 hours 97

4-39 SEM and EPMA results of Fe-12%Cr-1.25%Si after exposure at 600°C for 500 hours 98

4-40 SEM and EPMA results of Fe-18%Cr-0.5%Si after exposure at 600°C for 100 hours 99

4-41 SEM and EPMA results of Fe-18%Cr-0.5%Si after exposure at 600°C for 500 hours 100

4-42 SEM image and X-ray maps of Fe-18%Cr-1.25%Si after exposure at 600°C for 500 hours 102

4-43 XPS survey spectra for Fe-18%Cr-1.25%Si after exposure at 600°C for 500 hours 103

4-44 XPS high-resolution spectra of (a) Cr and (b) Si obtained from Fe-18%Cr-1.25%Si material tested in 600°C LBE for 500 hours 103

4-45 XRD spectra of Fe-18%Cr-1.25%Si material showing the existing phase peak after exposure at 600°C for 500 hours 104

4-46 Detailed peak identification of XRD spectra of Fe-18%Cr-1.25%Si material tested in LBE at 600°C for 500-hour 104

4-47 SEM image of Fe-18%Cr-2.55%Si material showing a very thin interaction layer formed during the 250-hour exposure to 600°C LBE 105

4-48 XPS survey spectra for Fe-18%Cr-2.55%Si after exposure at 600°C for 250 hours 105

4-49 XPS high-resolution spectra of (a) Cr and (b) Si obtained from Fe-18%Cr-2.55%Si material after exposure at 600°C for 500 hours 106

4-50 Detailed peak identification of XRD spectra of Fe-18%Cr-2.55%Si material after exposure at 600°C for 500 hours 106

4-51 SEM image of heavily cold worked, small grain sized material with the same composition as Fe-18%Cr-2.55%Si 107

5-1 The growth of oxide layer formed on Fe-Cr alloys after 600°C LBE static test 114

5-2 Comparison between the reported diffusion coefficients and the calculated diffusion coefficient of Cr in Fe-18wt% Cr after 500-hour exposure at 600°C 119

5-3 The growth of interaction layer thickness on Fe-Cr-Si with high Cr content 126

List of Tables

1-1	Properties of liquid metals	14
2-1	Analytical representation of experimental data on solubility of solid metal in liquid metal of Pb, Pb-Bi eutectic and Bi	27
2-2	The standard Gibbs free energy changes for oxidation reactions, the equilibrium P_{O_2}, and the corresponding ratio of P_{H_2} / P_{H_2O} (at 600°C) for selected metals	32
3-1	Nominal compositions of selected alloys for Pb-Bi eutectic corrosion tests	56
3-2	Chemistry data of Fe-Si and Fe-Cr-Si alloys	57
3-3	Chemistry data of high purity Pb and Bi	57
3-4	Summary of static LBE test matrix conducted at 600°C under controlled atmosphere of $P_{H_2} / P_{H_2O} \sim 1000$	61

Acknowledgements

Many people have touched my life during my stay at MIT and made those days memorable. I owe special thanks to them for their encouragement and friendship leading me to the completion of this long endeavor.

I am deeply grateful to my thesis advisor, Professor Ronald G. Ballinger, for his guidance and unwavering support throughout my stay at MIT. He has always supported my research work even at times when I doubted its merits. I owe special thanks to my thesis reader Dr. Ning Li, for his guidance and invaluable insight covering many areas of my research. I would like to thank my thesis committee members in Department of Nuclear Science and Engineering for their counsel and advice that helped me bring my research to final fruition.

Special thanks must be given to Dr. Nilanjan Chatterjee, for his sincere help and training for EPMA. I would also like to thank the research staff of the Shared Experimental Facilities (SEF) in the MIT Center for Materials Science and Engineering (CMSE), especially Dr. Anthony Garratt-Reed, Mr. Mike Frongilo, Mr. Joseph Adario and Ms. Elizabeth Shaw, for their training and help with important materials characterization tools including SEM, TEM, XRD, and XPS.

I sincerely thank to the staff at the Plasma Science Fusion Center (PSFC), especially Mr. Pete Stahle, Mr. Dave Tracy and Ms. Barbara Keesler for their technical and administrative assistance. They made the laboratory experience as well as my stay in the office fun and rewarding.

The work presented in this thesis has been sponsored by Idaho National Engineering and Environmental Laboratory (INEEL), Japan Nuclear Cycle Development Institute (JNC), and Los Alamos National Laboratory (LANL).

None of this would have been possible without prayer of my parents who have always stood by my side with their never-ending love and unshakable trust in me. I owe them so much.

CHAPTER 1

INTRODUCTION

1.1. Lead-Alloy Coolant Technology

The high power densities and temperatures expected for next generation nuclear applications, including power generation and transmutation systems, will require new types of heat transport systems to be economic. Present interest in heavy liquid metal coolants, especially in lead and lead-bismuth eutectic, originates from such requirements as increased heat removal capacity and enhanced safety features.

Lead (Pb) and lead-bismuth eutectic (LBE) coolants exhibit favorable thermo-physical and chemical properties. Their low melting temperatures and wide margins to boiling have advantages over conventional coolants such as water and sodium, providing additional safety during postulated accident scenarios. Low vapor pressure and chemical inertness with respect to reaction with air and water eliminate a significant combustion hazard present in sodium-cooled nuclear power plants. Their favorable neutronic properties, such as high spallation neutron yields, and low neutron moderation and capture, make them excellent candidate materials for use as high power spallation targets in an accelerator-driven, waste transmutation system (ADS). This system is designed to burn actinides and long-life fission products from the spent fuel of light water reactors, in order to reduce the ultimate disposal volume.

The development of Pb-alloy coolant technology will allow for successful applications with maximized efficiency and enhanced safety. However, the issue of material compatibility, arising from the interaction between the Pb-alloy coolant and structural materials at the higher temperatures that will be necessary for economic operation represents a critical challenge for the technology. In spite of decades-long studies on this issue, the lack of systematic understandings limits the R&D efforts towards technological advances. This thesis will focus on the characterization and mitigation of liquid Pb-alloy corrosion by seeking fundamental understandings on its mechanisms.

1.1.1 Properties of Pb-alloy Coolants

A binary alloy of lead (Pb) and bismuth (Bi) has a melting point of 125.5°C when 44.8 wt% of Pb and 55.2 wt% Bi are mixed. As shown in the phase diagram in Figure 1-1[1]. This composition of Pb-Bi alloy is the eutectic composition and is designated as LBE in this thesis. Pure Pb has a boiling temperature of 1750°C and pure Bi a boiling temperature of 1564°C, while LBE boils at 1670°C. The wide margin between melting and boiling enhances safety by assuring a liquid phase coolant even under postulated accident scenarios. The high boiling point also eliminates the requirement for pressurization which is an added bonus for the use of this coolant type. Unlike sodium or other alkali metal coolant, Pb-alloy coolants do not react with air and water, thus eliminating the need for protection system against fire and an intermediate heat transport loop. Table 1-1 summarizes thermal, physicochemical and nuclear properties of Pb, Bi and LBE along with those of sodium for comparison purposes.

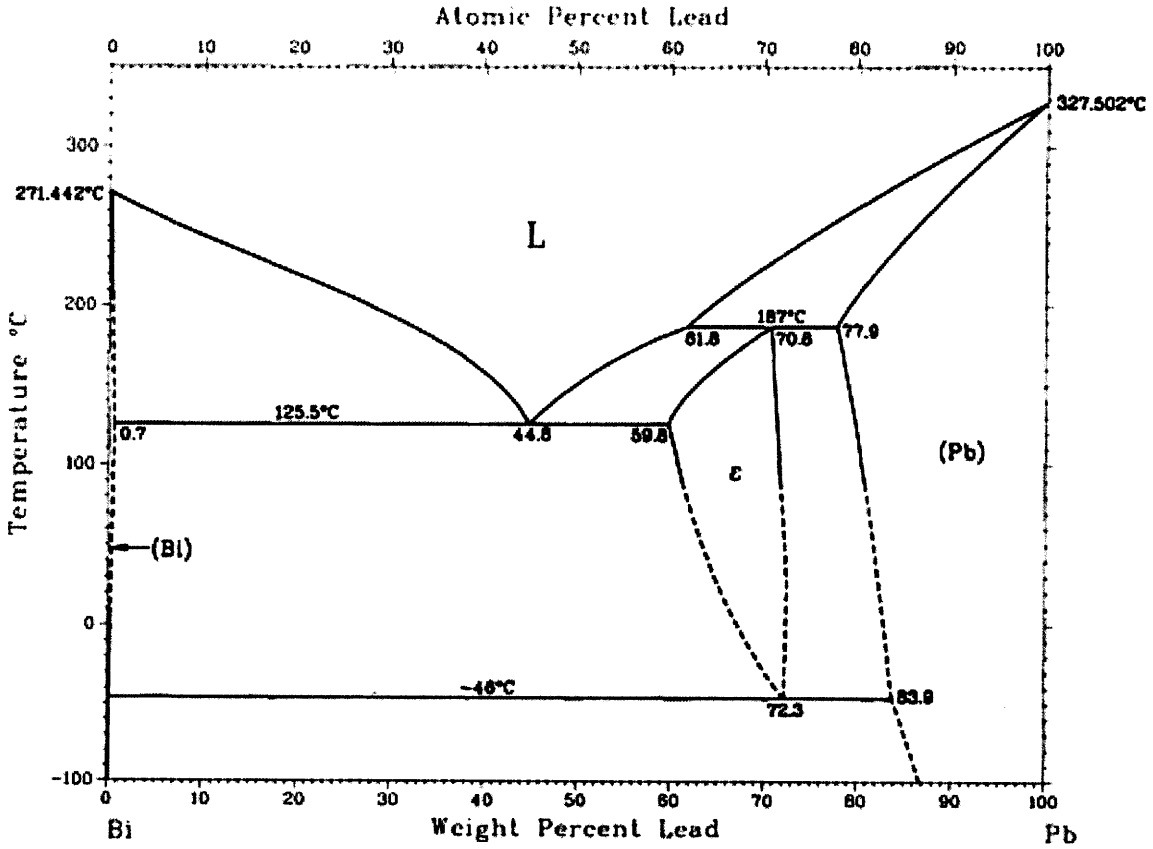

Figure 1-1 Pb-Bi phase diagram [1].

Table 1-1 Properties of liquid metals [2-4].

Liquid Metal	Pb	LBE	Bi	Na
Atomic number	82	-	83	11
Atomic weight (amu)	207.2	~208	208.9804	23.0
Melting Point (°C)	327.5	125.5	271.4	97.8
Boiling Point (°C)	1750	1670	1564	883
Density (g/cm^3 at 600°C)	10.27	9.91	9.66	0.83
Viscosity (cP at 600°C)	1.556	1.170	1.049	0.207
Vapor Pressure (mmHg at 600°C)	0.0004	NA	0.08723	23.70
Thermal Neutron Cross Section (barns)	0.17	0.094	0.034	0.53
Chemical Reactivity (with air and water)	Inert	Inert	Inert	Highly reactive

1.1.2 Material Compatibility Issues of Pb-alloy Coolant Technology

A long recognized limitation of the use of liquid Pb-alloys as coolant is the corrosive nature of the coolant toward cladding and structural materials. Due to the importance of structural materials selection which will help guarantee the integrity of system with all the benefits of Pb-alloy coolant, the corrosion phenomena by liquid Pb-alloy are briefly addressed here. For other engineering issues such as core neutronic design, coolant activation and plant engineering, a detailed review can be found in the literature [3].

In general, corrosion of structural materials by liquid Pb-alloys forms a sub-category of liquid metal corrosion and exhibits the following phenomena common to this type of corrosion [5].

- Dissolution
- Impurity reactions

- Chemical reduction
- Alloying with other elements in the system

The literature, the above classifications may be taken as somewhat arbitrary, since the individual reactions do not necessarily occur independently. Among those listed, the first two phenomena are worth special attentions in liquid the Pb-alloy environment.

When solid metals are placed in contact with liquid Pb-alloy in the absence of any impurity, a simple solution process, governed by the elemental solubilities specific to each solid-liquid system, will occur. Subsequent atomic transfer of species into the liquid metal will then ensue. In an isothermal system, dissolution of solid metal will cease upon reaching the equilibrium condition where elemental solubility reaches its thermodynamic saturation value in the liquid metal.

However, in a system containing a thermal gradient with flowing liquid metal, the temperature dependent nature of the solubility results in a removal of materials from hotter zone where the solubility is greater than the bulk, to the colder zone where deposition transported elements occur due to the reduced solubility. This process is of prime concern in developing Pb-alloy coolant as it will determine the service life span of structural materials in a non-isothermal, forced convection loop system. Figure 1-2 shows a schematic of such a mass-transfer process [5].

Considerations of selected impurity reactions have lead to possible remedies for liquid Pb-alloy corrosion. In this discussion, "impurity" refers to a non-metallic light element such as oxygen, carbon, or nitrogen, present in the structural materials or in the liquid metal. In many cases, where the solubilities of elements in structural metals are low in liquid metal, reactions involving light elements can alter or override the dissolution process by forming stable compounds that act as protective surface films.

Given the fact that the oxides formed by major alloying elements in structural metals have a lower equilibrium oxygen partial pressure than that of Pb or Bi oxides, strategic remedies have been proposed and are currently employed in many applications to protect structural metals from

liquid Pb-alloy corrosion. These include: (1) selecting such structural materials alloyed with elements to form more stable oxides other than Pb- or Bi oxides and (2) reducing the oxygen activity in liquid Pb-alloy to stabilize only the surface oxides of the structural metals while preventing formation of Pb- or Bi oxides that will result in sludge formation in the coolant system. Russian experience with liquid Pb-alloy coolant for nuclear submarines has lent credence to the validity of this approach and the control scheme of such selective oxidation has been reported along with candidate structural materials [6-7].

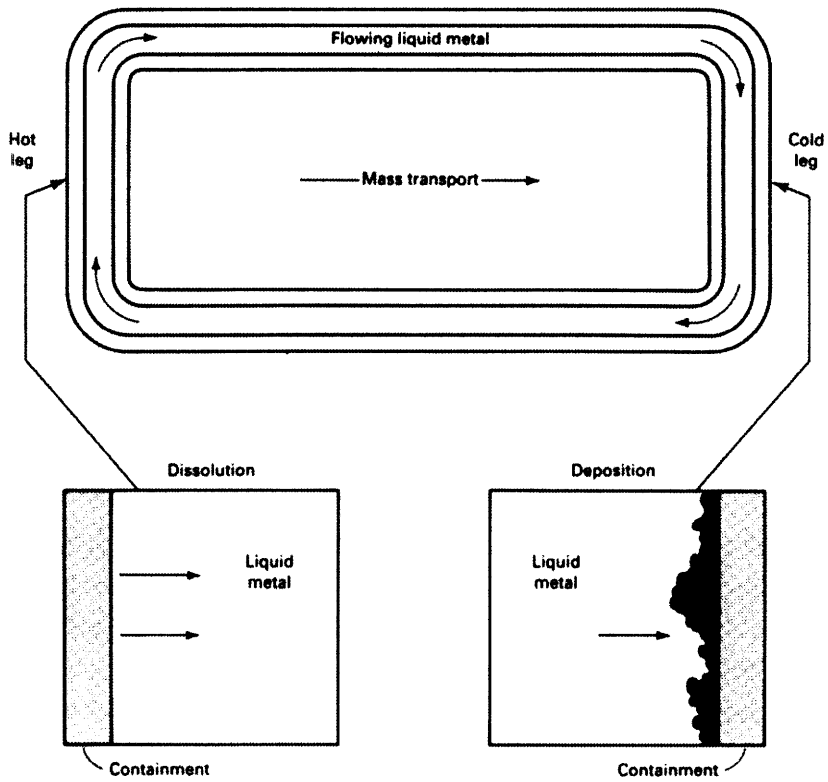

Figure 1-2 Schematic of thermal gradient mass transfer in a liquid metal circuit [5].

Other reactions such as compound reduction mainly occur in the oxide, carbide or nitride based ceramics exposed to liquid lithium system resulting in the loss of structural integrity. Most of structural ceramics in liquid Pb-alloy environment are not assumed to undergo such process.

Finally, the alloying interaction between atoms of the structural material component and those of the liquid metal can be a major concern when the resultant compounds formed on the

surface are very stable and have low thermal conductivity. Rather ironically, this reaction can also be used to protect the metal surface by intentionally adding certain elements to the liquid Pb-alloy so as to form a corrosion-resistant layer. Examples include the inhibition of corrosion by the addition of Zr or Ti to react with nitrogen and carbon in steel to form a nitride or carbide surface layer have been reported. However, the actual application of this strategy to a large scale system for a long term operation is fairly limited because of the difficulty in monitoring and controlling inhibitor concentrations.

1.1.3 Selection Guide for Candidate Materials

At relatively low temperatures (below 450°C) with small temperature gradient, corrosion by liquid Pb-alloys is often insignificant. However, in more demanding situations commonly encountered in advanced nuclear applications, where the coolant system is required to operate at higher temperature with larger temperature gradient, a long term safety becomes of paramount concern, making the material compatibility issue as a cornerstone in developing liquid Pb-alloy coolant system. In an effort to help select materials system that can possibly overcome the compatibility issue, this section will briefly review previous literature findings covering from commercial steel systems to ceramic materials.

Iron based alloys

Selective dissolution of nickel due to its high solubility in liquid Pb-alloys makes the use of austenitic grade stainless steels such as 316L highly unlikely except at low temperatures. At 420°C, when exposed to oxygen controlled, flowing (up to 2 m/s) LBE, AISI 316L does not show any sign of corrosion and is protected by thin oxide film on the surface. However, for exposure at 600°C, the surface exhibits a deep penetration zone by LBE accompanied by significant nickel depletion. Additionally, loss of material due to erosion was observed [8].

Chromium is known to be more soluble than iron in liquid Pb-alloys [2]. However, the mode of corrosion for Fe-Cr ferritic alloys is significantly affected by the oxygen concentration in the

liquid metal. In the absence of oxygen in the liquid, higher corrosion rates have been reported with increase in Cr content in iron alloys [9-10]. On the other hand, increased corrosion resistance was observed with higher Cr steels in the presence of dissolved oxygen [2, 12]. It is believed that the formation of protective chromium oxide can mitigate dissolution attack. The addition of elements such as Si and Al is also known to improve the overall corrosion resistance of ferritic steels, due to the formation of stable oxide films even at a very low oxygen concentrations [6-7, 12].

The effectiveness of oxygen control in liquid Pb-alloys has been discussed in many literature sources [7,9,13]. Some data indicate the formation of iron oxide can help prevent dissolution and are backed by the experimentally observed, lower than expected corrosions rate of steels tested at temperatures less then 550°C [14]. While these observations apparently support the general concept of the corrosion resistance of oxide films, a fundamental understandings of the stability of these films and the effect of alloying elements still remain preliminary when applied to the liquid Pb-alloy system. It would be worthwhile to develop systematic approach to the understanding of the oxidation characteristics of iron based alloys in contact with liquid Pb-alloys. Such an understanding would serve as the basis for the development of high temperature alloys utilizing the vast amount of accumulated data and favorable engineering properties of iron based alloys.

Refractory metals and alloys

Temperature limitations associated with the use of carbon steels have prompted research into the use of refractory materials such as molybdenum (Mo), tantalum (Ta), tungsten (W) and niobium (Nb) and their alloys. These materials are known to be corrosion resistant to liquid Bi at temperatures up to 700°C, including Mo, Ta-8wt%W-2wt%Hf, and Ta-10wt%W [10]. In liquid Pb, these alloys were considered as candidates for higher temperature application [9]. Molybdenum did not show any detectible attack when tested under pure, oxygen free lead at temperatures up to 1000°C [12]. However, the low melting temperature of Mo oxide can limit its use when there is oxygen present in the system., Additionally, Mo becomes too brittle under low-fluence proton irradiation [9]. Ta is corrosion resistant to high temperature Pb and Bi, but is

easily oxidized and has a high thermal neutron absorption cross-section [9]. W also has a high thermal neutron absorption cross-section [9] and can increase the cost of fabrication due to its poor machinability. Nb is susceptible to internal oxidation, making it problematic as a structural material in oxygenated environment. Lastly, these refractory metals and alloys are very expensive. The above considerations essentially eliminate these materials as the primary structural material in an oxygen controlled and radiation exposure environment.

Ceramics

Most oxide, carbide, and nitride ceramics are known to be compatible with Pb and Bi [2]. Alumina showed no wetting, visible attack or significant weight change at 700°C in liquid Pb after 88 days[12]. Carbides and nitrides, such as TiC, ZrC, WC , TiN and ZrN, are corrosion resistant to liquid Bi[2]. Silicon nitride appears to be compatible with liquid lead at 720°C without showing any sign of corrosion [12]. Graphite is considered as compatible with Pb and Bi up to 1000°C, provided no air ingress occurs during operation [2,12]. In spite of their advantages in corrosion resistance, these ceramic materials generally have very poor mechanical properties, making them not suitable as structural material unless used as a part of a functionally graded or composite material.

1.2 Objectives of research

Corrosion of structural metals represent a major limiting factor in developing advanced liquid Pb-alloy coolant technology. In fact, the development of advanced structural and cladding alloys that are resistant to corrosion over a wide range of oxygen potentials in this environment would represent the enabling technology for these systems. Previous efforts to identify candidate materials for the service have been marginally successful, in terms of narrowing down the range of applicable materials and of devising a feasible corrosion mitigating scheme. However, the nature of corrosion and protection mechanisms have not been fully explored enough to lead to the development of such system with engineering feasibility. The goal of this research is to develop a class of Fe-Cr Si alloys that are resistant to corrosion in Pb and Pb alloys at temperatures of 600°C or higher. As a necessary part of this development effort, an additional

goal is to further the fundamental understandings of the mechanisms by which corrosion protection is achieved.

As will be discussed further later in this thesis, the alloy development effort is based on the following set of assumptions and/or hypotheses:

1. Fe-based alloys have been shown to be resistant to Pb/Pb-Bi corrosion. However, the scientific basis has not been fully developed.
2. The Fe-based system can be optimized for Pb, Pb/Bi service.
3. Use of a low solubility matrix (Fe) can be augmented by the addition of Si and Cr to enhance corrosion resistance at both "reducing" and "oxidizing" potentials with respect to Fe_3O_4 (reducing) and SiO_2 and Cr_2O_3 (oxidizing).
4. For reducing conditions the Fe-Cr-Si matrix will dissolve with preferential enrichment of Si at the surface. Further dissolution will be inhibited by Si enrichment.
5. For oxidizing conditions the Fe-Cr-Si matrix will dissolve with preferential enrichment of Si at the surface. Depending on oxygen potential, a point will be reached where Si-oxide layer will become stable. Layer effectiveness will be augmented by Cr additions.

The validity of these assumptions will be discussed in subsequent chapters, particularly Chapter 3.

1.3 Outline and Keypoints

Chapter 2 presents a review of the basic thermodynamic and kinetic principles that are applicable to the liquid Pb-alloy corrosion. A brief review of the thermodynamic nature of liquid Pb-alloy corrosion is provided, along with the relevant literature data available on thermodynamic solubilities of various metal systems, which would set a criterion for selecting candidate metal system for further development. The literature review highlights the effectiveness of iron based alloy system associated with its low solubility in liquid Pb-alloy. A review of the kinetic process involved with dissolution follows later in the chapter. The literature review discusses transport process with respect to the flow conditions in liquid Pb-alloys. A detailed review of the oxygen control scheme is given from thermodynamic viewpoints, to

access its proposed validity as a key corrosion mitigation scheme. Based on this, major alloying elements for iron based system are determined as chromium and silicon and the characteristics of their oxide systems are further discussed.

Chapter 3 summarizes the selection and the development process of model alloys based on the iron system, Fe-Si, Fe-Cr and Fe-Cr-Si. Key points in designing the experimental facility are discussed thereafter, followed by a description of high temperature testing facility built to expose materials under well defined condition being a central focus on the method of oxygen control. In addition, the sample preparation and analysis procedure after experiment are discussed briefly.

Experimental results obtained from model alloys after LBE exposure at 600°C with varying durations are provided in Chapter 4. The corrosion data analysis exhibited clear distinctions between alloy groups as well as in the individual alloy. The behavior of Fe-Cr alloys showed changes in the oxidation modes and in the constituent oxide compositions depending on Cr concentration of each alloy. The instability and non-protectiveness of iron oxides are confirmed as expected under testing the conditions studied. Test results for Fe-Si alloys showed the formation of silicon oxide precipitates residing in the internal oxidation zone, which would act as an effective diffusion barrier hindering further oxidation and dissolution of base metals. The observed features in Fe-Cr-Si alloys will be categorized into two groups: (a) low Cr alloyed Fe-Cr-Si materials showed an extensive internal/grain boundary oxidation zone, while (b) high Cr alloyed materials showed an increased resistance to further oxidation.

Detailed analyses of the corrosion and/or oxidation behavior on the model alloys are provided in Chapter 5. Experimental data presented in Chapter 4 are reassessed from the viewpoint of kinetic models, in an effort to explain key processes governing the material diffusion observed during exposure. The observed reduction in parabolic reaction rate in Fe-Cr alloys with increase in Cr concentration was attributed as the effect of Cr in alloy. The hypothesis that Si addition would promote the formation of a diffusion barrier was confirmed by the actual reduction of oxide thickness over time. The Si effect was magnified by the addition of Cr to the system. Based on a kinetic data assessment on the experimental results of Fe-Si and Fe-Cr-Si (low Cr) alloys, the synergetic alloying effect of Cr and Si was revealed.

Lastly, Chapter 6 presents an overall summary of the current research and recommendations for future work from the viewpoint of new alloy development.

1.4 References

[1] Alloy Phase Diagrams, Vol. 3, Metals Handbook Desk Edition, Second Edition, ASM International, 1998, in ASM Handbooks Online, http://www.asmmaterials.info ASM International, 2004.

[2] J. R. Weeks, "Lead, Bismuth, Tin and Their Alloys as Nuclear Coolants", Nuclear Engineering and Design , 15 (1971), pp. 363-372.

[3] J. Buongiorno et al., "Design of an Actinide Burning, Lead or Lead-Bismuth Cooled Reactor that Produces Low Cost Electricity", FY-01 Annual Report, INEEL/EXT-01-01376, MIT-ANP-PR-083, October, 2001.

[4] C. L. Yaws (ed.), Chemical Properties Handbook, McGraw-Hill, 1999.

[5] P.F. Tortorelli and S.J. Pawel, "Corrosion by Liquid Metals", in Corrosion: Fundamentals, Testing, and Protection, Vol 13A, *ASM Handbook*, ASM International, 2003, p 129–134.

[6] I. V. Gorynin et al., "Structural Materials for Power Plants with Heavy Liquid Metals as Coolants", in Proceedings: Heavy Liquid Metal Coolants in Nuclear Technology, Vol. 1 (HLMC-98), Obninsk, Russia, 1998, pp. 120-132.

[7] G. S. Yachmenyov et al., "Problems of Structural Materials' Corrosion in Lead-Bismuth Coolant", in Proceedings: Heavy Liquid Metal Coolants in Nuclear Technology, Vol. 1 (HLMC-98), Obninsk, Russia, 1998, pp. 133-140.

[8] G. Muller et al., "Results of Steel Corrosion Tests in Flowing Liquid Pb/Bi at 420-600°C after 2000h", Journal of Nuclear Materials, 301 (2002) pp.40-46.

[9] J. J. Park, D. P. Butt, and C. A. Beard, "Review of Liquid Metal Corrosion Issues for Potential Containment Materials for Liquid Lead and Lead-Bismuth Eutectic Spallation Targets as a Neutron Source", Nuclear Engineering and Design, 196 (2000) pp. 315-325.

[10] P. F. Tortorelli and O. K. Chopra, "Corrosion and Compatibility Considerations of Liquid Metals for Fusion Reactor Applications", Journal of Nuclear Materials, 103&104 (1981) pp. 621-632.

[11] N. Li, "Active Control of Oxygen in Molten Lead-Bismuth Eutectic Systems to Prevent Steel Corrosion and Coolant Contamination", Journal of Nuclear Materials, 300 (2002) pp.73-81.

[12] R. C. Asher, D. Davies and S. A. Beetham, "Some Observations on the Compatibility of Structural Materials with Molten Lead", Corrosion Science, 17 (1977) pp. 545-557.

[13] G. Muller, G. Schumacher, and F. Zimmermann, "Investigation on Oxygen Controlled Liquid Lead Corrosion of Surface Treated Steels", Journal of Nuclear Materials, 278 (2000) pp. 85-95.

[14] H. Glasbrenner, J. Konys, G. Mueller, and A. Rusanov, "Corrosion Investigations of Steels in Flowing Lead at 400°C and 550°C", Journal of Nuclear Materials, 296 (2001) pp. 237-242.

[15] J. V. Cathcart and W. D. Manly, "The Mass Transfer Properties of Various Metals and Alloys in Liquid Lead", Corrosion, 12 (1956) pp. 43-47.

CHAPTER 2

BACKGROUND

The corrosion of structural materials has long been a recognized limitation to the use of heavy liquid metal as a coolant in nuclear power systems. Since corrosion limits the highest achievable operating temperatures, which in turn significantly compromises the economic viability, an understanding the principles of the corrosion process is essential in developing advanced materials for this service.

As mentioned in the previous chapter, corrosion of structural metal in contact with liquid Pb-alloys occurs primarily as a simple dissolution process related to its solubility in the liquid. The corrosion rate of the material increases with increasing temperature as its solubility and the subsequent diffusion process are strong functions of temperature. Thus, if a liquid Pb-alloy is used as a heat transfer medium flowing in a non-isothermal loop, continuous mass transfer from the hot zone to the cold zone will occur due to the existing thermal gradient. An increase in flow velocity can increase the rate of this transfer process and even exacerbate the material removal.

A protection scheme currently proposed for the iron-based structural materials relies on the oxygen exchange reaction between the liquid and solid metals [1-3]. This strategy utilizes the fact that the elements of interest (Fe, Cr, Si and Al) are able to form stable oxide films at much lower oxygen partial pressure than that for Pb and Bi oxides, and that selective oxidation of these elements can give adequate protection by providing diffusion barrier retarding dissolution of the base metal. Therefore, a successful implementation of an oxidation control system is a key step toward the enhanced system integrity.

In this chapter, the general principles of thermodynamics and kinetics of liquid metal corrosion will be presented and more specific features to the liquid Pb-alloy coolant system will be explored. As for the oxidation processes, oxide properties of relevant elements for iron based system will be reviewed with respect to their effectiveness in protecting the base metal.

2.1 Thermodynamic Principles in Liquid Metal Corrosion

2.1.1 Solid-Liquid Metal System

When solid metal B forms a dilute binary solution with liquid metal A, the thermodynamic equilibrium can be described by the following relationship

$$B(s) = \underline{B}_{\text{in A}} \tag{1}$$

where A and B stand for any liquid and solid metal, $\underline{B}_{\text{in A}}$ for the saturated solution of solid metal B in liquid metal A, and s for solid phase.

If the solution of pure solid metal in equilibrium with the liquid metal obeys Henry's law, the following expression is valid, provided the Henrian state is chosen as standard state.

$$\ln X_B = -\frac{\Delta G}{RT} = -\frac{\Delta H}{RT} + \frac{\Delta S}{R} = \alpha - \frac{\beta}{T} \tag{2}$$

where X_B is the mole fraction of solute, ΔG the Gibbs free energy change, ΔH the sum of the differential heat of solution and heat of fusion, R the gas constant, T the absolute temperature, ΔS the sum of entropy of fusion and the excess partial molar entropy, and α and β are constants.

Table 2-1 summarizes available solubility data for solid metals in liquid Pb, LBE and Bi, obtained from various literature sources [3-9]. The solubility equations are represented in weight percent (wt% solute). When the original literature data was represented in mole fraction, conversion to the weight percentage basis was carried out with the use of the following relationship [10] by assuming a very dilute concentration of solute B.

$$X_B = \frac{(C_{B,\,wt\%})}{M_B}\frac{M_A}{100} \tag{3}$$

where X_B is the mole fraction of solute, $C_{B,\,wt\%}$ is the concentration of solute B expressed in wt%, and M_A and M_B are the atomic weights of the solvent A and the solute B. Because the converted equations (wt% basis) have the same temperature dependence as shown in Eq. (2), only the values of α were altered by conversion. Atomic weight data of elements are obtained from Reference [11].

Using the data from Table 2-1, the solubilities of Fe, Cr and Ni in LBE at 600°C are approximately 9.8 ppm, 23.3 ppm, and 36674 ppm, respectively. Thus, the use of a Ni containing alloy at high temperatures should not be contemplated as its susceptibility to selective corrosion will be high and increases with increase in temperature. Ti and Zr have solubilities of 300 ppm and 328 ppm, respectively at 600°C LBE, which enable them to serve as inhibitors to form carbides and nitrides by reacting with steel components of nitrogen and carbon. Co, Cu and Al have substantial solubilities in liquid Bi when compared to that of Fe (50 ppm) in 600°C Bi. The solubility of Mo and W are below detection limit in Pb-alloys, even though their solubility equations do exist for liquid Pb. Metals having very low, or almost non-detectable solubility in liquid Bi include Si, Ta, Re, Ir, and Os according to Weeks [12]. Apart from exotic materials including refractory metals having fabricability issues as Mo, W and Ta, the logical choice is iron as a primary base metal for use in liquid Pb-alloy system, considering its reasonably low solubility, favorable neutronic and mechanical properties. Most of all, the vast amount of testing data on iron based materials will help us design iron based alloys suitably tailored for high temperature liquid Pb-alloy service. From that perspective, the continuing discussions will focus mainly on iron and its alloying elements.

Figures 2-1 shows the solubility curves for Fe in liquid Pb-alloys as a function of Bi content. The solubility curves for Cr and Ni in liquid Pb-alloys are shown in Figure 2-2 as a function of temperature. It can be noted that the solubilities of Fe, Cr or Ni are the highest in liquid Bi, the lowest in liquid Pb, and in the middle in Pb-Bi eutectic (LBE). The solubility data for Fe in a liquid Pb-Bi mixture shows a strong dependence on Bi concentration as depicted in Figure 2-1. Since no intermetallic compounds have been reported in the Fe or Cr ternary system with Pb-Bi [4], the solubility of Fe or Cr in Pb-Bi eutectic can be also obtained from a line interpolation of the binary solubilities in Bi and Pb [5].

Table 2-1 Analytical Representation of Experimental Data on Solubility of Solid Metal in Liquid Metal of Pb, Pb-Bi eutectic and Bi [3-9].

Liquid Metal / Solute	Pb		Pb-Bi eutectic(LBE)		Bi	
	Solubility Equation: $\log_{10}$ (C_B, wt % Solute) =α-β/T (T in K)					
	$\alpha_{\text{in Pb}}$	$\beta_{\text{in Pb}}$	$\alpha_{\text{in LBE}}$	$\beta_{\text{in LBE}}$	$\alpha_{\text{in Bi}}$	$\beta_{\text{in Bi}}$
Al	-	-	-	-	2.55	2110
Co	-	-	-	-	0.38	1520
Cr	3.87	6947	-0.02	2280	2.26	3580
Cu	-	-	-	-	2.30	1690
Fe	0.34*	3450*	2.01	4380	1.69**	3490**
Mo	2.92	10552	-	-	-	-
Ni	1.30	1381	1.53	843	2.38	1400
Ti	-	-	0.95	2160	2.04	2230
W	6.52	10070	-	-	-	-
Zr	-	-	2.15	3172	2.69	2780

* Applicable for $400 \le T \le 600^{\circ}C$. For $600 \le T \le 750^{\circ}C$, $\alpha_{\text{in Pb}}$ and $\beta_{\text{in Pb}}$ are 1.824 and 4860, respectively [5].
**Applicable for $T \le 700^{\circ}C$. For $T \ge 700^{\circ}C$, $\alpha_{\text{in Bi}}$ and $\beta_{\text{in Bi}}$ are 2.18 and 3980, respectively [9].

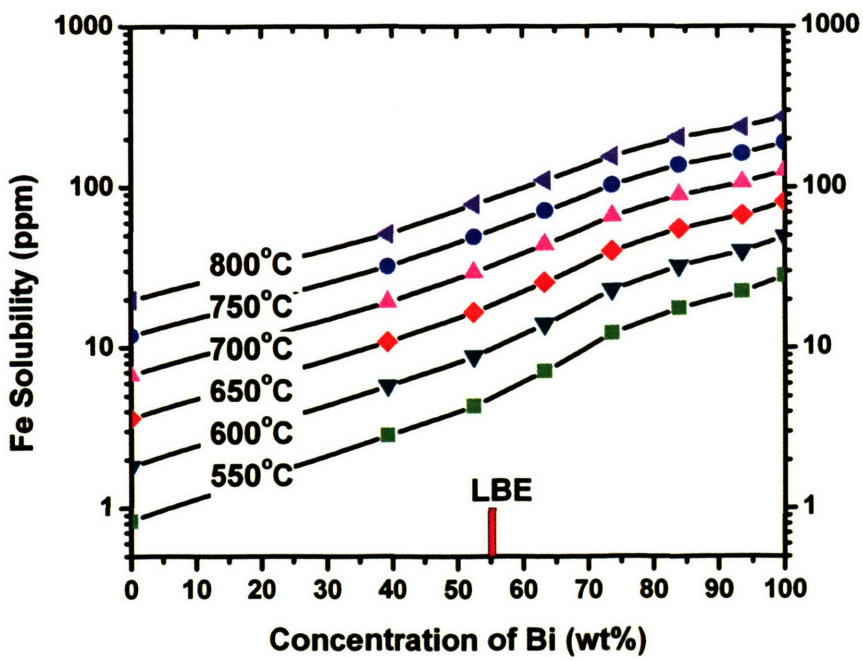

Figure 2-1 Isotherms of the Ternary Fe-Bi-Pb liquidus [5].

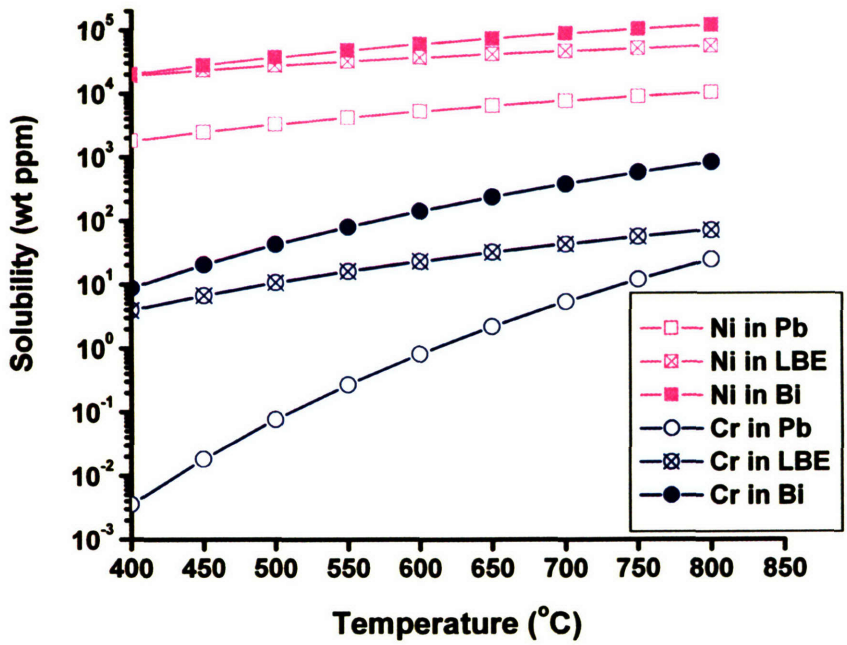

Figure 2-2 Solubilities for Cr and Ni in liquid Pb, Bi and Pb-Bi eutectic (LBE) [3-4,8].

2.1.2. Solubility of Oxygen in Liquid Pb-alloys

The oxygen molecule O_2 dissolves in liquid metal as atoms [10]. When pure liquid metal is brought into contact with oxygen gas at a relatively low pressure, oxygen molecules striking the liquid surface become adsorbed on the surface. The adsorbed molecules then dissociate to form adsorbed O atoms, then the diffusion of O atoms into bulk melt ensue [13]. When gaseous oxygen at 1 atm pressure is dissolved in a liquid metal (LM) at a concentration of 1 atomic percent (at%) under isothermal condition, the overall reaction can be written as

$$\frac{1}{2}O_2(g, P = 1\,\text{atm}) = \underline{O}_{(1\,\text{at\% in LM})} \tag{4}$$

The change in the molar Gibbs free energy can be represented as follows, provided a 1 at% standard state is chosen and a very dilute solution of O is assumed [13-15],

$$\Delta G^0_{\underline{O}_{(1\text{ at\% in LM})}} = RT\ln\frac{\gamma_O^\infty}{100} = -RT\ln K = -RT\ln\frac{a^H_{O(1\,\text{at\%})}}{P^{1/2}_{O_2}} \tag{5}$$

where γ_O^∞ is the activity coefficient of oxygen at infinite dilution, K the equilibrium constant, $a^H_{O(1\,at\%)}$ the activity of O with respect to the 1 at% standard state having unit activity, which is located at the point on the Henry's law line corresponding to a concentration of 1 at% O.

This result is approximate because the higher order self interaction coefficients of oxygen in the solution have been ignored. However, if the concentration of oxygen is quite small, which is the case for the most of oxygen-liquid metal systems, the self-interactions between oxygen atoms in solution can be ignored. Moreover, this self-interaction parameter contributes to the oxygen activity coefficient (and eventually to the change in Gibbs free energy) as a multiplied value with the concentration, which in turn can be considered negligible for a very dilute oxygen solution. In such cases, the assumption of $\ln\gamma_O \approx \ln\gamma_O^\infty$ is adequate.

The activity of oxygen with regard to the 1 at% standard state is

$$a^H_{O(1\,at\%)} = f_{O(1\,at\%)} \cdot C_{O,\,at\%} \tag{6}$$

where $f_{O(1\,at\%)}$ is the 1 at% activity coefficient, $C_{O,\,at\%}$ is the concentration of O in at%. In the range of compositions where the oxygen solute obeys Henry's law and exhibits Henrian ideality, $f_{O(1\,at\%)} = 1$ and hence $a^H_{O(1\,at\%)} = C_{O,\,at\%}$.

Combining Eqs (5) and (6), the solubility of oxygen in liquid metal can be expressed as the following relationship,

$$C_{O,\,at\%} = P_{O_2}^{1/2}\left(\frac{100}{\gamma_0^\infty}\right) = P_{O_2}^{1/2}\exp\left(-\frac{\Delta G^0_{\underline{O}(1\,at\%\,in\,LM)}}{RT}\right) \tag{7}$$

In actual experimental studies, many researchers used electrochemical methods to obtain the solubility of oxygen and the Gibbs free energy changes by measuring the EMF developed in electrochemical cells at equilibrium with a known reference value of P_{O_2}. Among them, two sets of oxygen solubility data are widely accepted, which were published by Alcock and Belford [16] in liquid Pb and by Fitzner [17] in liquid Bi. Again, original data reported in atomic %, can be converted to the wt% basis unit by use of the following relationship,

$$C_{O,wt\%} = \frac{100 \times C_{O,at\%} \times MW_O}{C_{O,at\%} \times MW_O + (100 - C_{O,at\%}) \times MW_{LM}} \quad (8)$$

where, MW_O is the atomic weight of oxygen and MW_{LM} is the atomic weight of the liquid metal. For solutions of oxygen in liquid Pb, LBE and Bi, 1 at% oxygen corresponds to 0.0779 wt%, 0.0776 wt% and 0.0773 wt%, respectively. The solubility data of oxygen in Pb-Bi eutectic (LBE) have been reported by IPPE and LANL [3].

Pb: $\log_{10}(C_{O,wt\%})$=3.44-5240/T [16]

LBE: $\log_{10}(C_{O,wt\%})$=1.20-3400/T [3]

Bi: $\log_{10}(C_{O,wt\%})$=3.85-5543/T [17]

Oxygen solubilities in equilibrium at 600°C (T=873K) with liquid Pb, LBE and Bi are calculated as 27.4 ppm, 20.2 ppm and 31.7 ppm, respectively.

The standard Gibbs free energy change data for the dissolution reaction of gaseous oxygen into liquid Pb or Bi can be found in the literature [14-21]. Chang et al.[14] summarized the Gibbs free energy data along with the interaction coefficients reported from a variety of sources, then examined their validity by comparing to the existing thermodynamic solution models applicable to binary and ternary systems. The following values of ΔG^0 are recommended for use in the binary solutions of Pb-O and Bi-O when 1 at% standard state is selected.

Pb-O system: $\Delta G^0_{\underline{O}\,(1\text{ at\% in Pb})} = -119100 + 14.6T(K)\ J/g \cdot atom\ O\ \ (510^oC \le T \le 1100^oC)$

Bi-O system: $\Delta G^0_{\underline{O}\,(1\text{ at\% in Bi})} = -99730 + 13.2T(K)\ J/g \cdot atom\ O\ \ (497^oC \le T \le 1200^oC)$

For LBE, interaction coefficient data are reported between 830°C and 900°C [23-24]. Although the data at 900°C were deemed meaningful by Chang et al. [14] and Hajra et al.[25], no adequate ΔG^0 data were reported below the melting temperature of PbO (872°C). Thus, no further attempt is made here to calculate ΔG^0 using the reported interaction coefficient data set.

2.1.3 Principles of Oxygen Control in Liquid Pb-alloys

The concept of oxygen control in liquid Pb-alloys originates from the varying degrees of thermodynamic stability of structural metal oxides. In terms of oxidation tendency, Pb and Bi are regarded as relatively inert when compared to iron and its major alloying elements. From this perspective, the oxygen control scheme aims to form a protective oxide film only on the solid metal surfaces, which will act as a diffusion barrier having adequate stability and which will hinder further dissolution of base metal into the liquid metal. With this perspective in mind, it is crucial to examine the relevant thermodynamic principles and apply them to experimental data, specifically obtained for liquid Pb-alloys. Again, with strong emphasis on iron based alloys considered as candidate structural materials, the following discussions will illustrate the optimum condition for oxygen control both thermodynamically and practically.

<u>Solid metal/metal oxide system</u>

The standard Gibbs free energy change data for the oxidation of selected solid metals are listed in Table 2-2, along with their equilibrium oxygen partial pressure values [13,15]. As a way to set oxygen partial pressure at a desired level, the well established method of controlling the ratio of the partial pressure of gaseous hydrogen with respect to moisture content is applicable for liquid Pb-alloy systems. The relevant relationships are given as follows:

$$H_2(g) + \frac{1}{2}O_2(g) = H_2O(g) \tag{14}$$

for which

$$\Delta G^0_{H_2O(g)} = -247500 + 55.85T \text{ (J)}$$

then, the oxygen partial pressure is obtained as

$$P_{O_2} = \left(\frac{P_{H_2}}{P_{H_2O}}\right)^{-2} \mathrm{Exp}\left(\frac{2\Delta G^0_{H_2O(g)}}{RT}\right) \tag{15}$$

At high temperatures, the reaction of Eq. (14) can be assumed to occur fast enough to assure that equilibrium is attained within a reasonably short time. The hydrogen to moisture ratios are also listed in Table 2-2, corresponding to the equilibrium oxygen partial pressure of each metal-metal oxide system calculated at 600°C. Figure 2-3 shows an Ellingham diagram for selected materials, depicting the domain of thermodynamic stability of their oxides in terms of temperature and oxygen partial pressure. The standard Gibbs free energy changes upon oxidation are calculated when solid metal is to react with 1 mole of O_2 . Lines indicating constant $P(H_2)/P(H_2O)$ ratios are superimposed for comparison purposes. This type of diagram offers a useful way to estimate the equilibrium condition of a metal/metal oxide. With the assumption of thermodynamic equilibrium, one can use this diagram to determine the required partial pressure ratio of hydrogen and moisture to reduce/oxidize certain metal-oxide/metal systems.

Table 2-2 The standard Gibbs free energy changes for oxidation reactions, the equilibrium P_{O_2}, and the corresponding ratio of P_{H_2} / P_{H_2O} (at 600°C) for selected metals [13,15]

Reaction	ΔG^0, Joules (T in K)	P_{O_2} (atm) (at 600°C)	$\frac{P_{H_2}}{P_{H_2O}}$
$2Bi(\ell) + 3/2O_2(g) = Bi_2O_3(s)$	−576932+265.4T	1.69×10^{-14}	9.87×10^{-6}
$Pb(\ell) + 1/2O_2(g) = PbO(s)$	−208700+91.8T	4.07×10^{-16}	6.35×10^{-5}
$Fe(s) + 1/2O_2(g) = FeO(s)$	−263700+64.4T	1.46×10^{-25}	3.35
$3Fe(s) + 2O_2(g) = Fe_3O_4(s)$	−1102200+307.4T	1.13×10^{-25}	3.81
$2Fe(s) + O_2(g) + SiO_2(s) = Fe_2SiO_4(s)$	−566095+143.9T	4.42×10^{-27}	19.3
$Fe(s) + 2O_2(g) + 2Cr(s) = FeCr_2O_4(s)$	−1435070+273.4T	1.61×10^{-36}	1.01×10^{6}
$2Cr(s) + 3/2O_2(g) = Cr_2O_3(s)$	−1159760+222.8T	3.13×10^{-39}	2.29×10^{7}
$Si(s) + O_2(g) = SiO_2(s)$	−907100+175.0T	7.32×10^{-46}	4.74×10^{10}

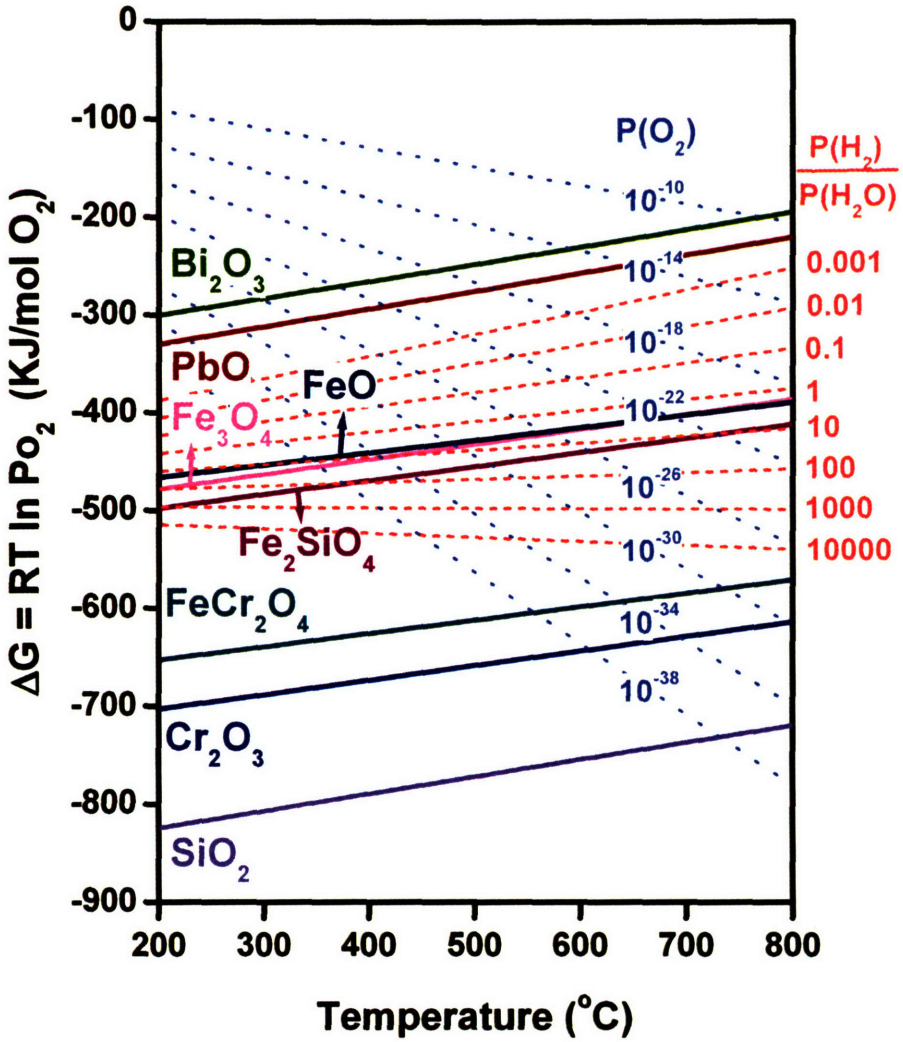

Figure 2-3 Ellingham diagram for selected metal-metal oxide systems.

Oxidation of Dissolved Fe in Liquid Pb

It is useful to have an exemplary calculation in order to illustrate the details of an oxygen control scheme. Because Pb/PbO has lower equilibrium oxygen partial pressure than Bi/Bi_2O_3 oxide, the formation of PbO is thermodynamically encouraged under high oxygen concentration. Therefore, in order to prevent the formation of PbO sludge and the resultant blockage of flow in LBE coolant system, the maximum allowable oxygen partial pressure should be limited with respect to the Pb/PbO equilibrium. Thus, the illustration on oxygen control will be focused on the liquid Pb case.

When Fe is dissolved in liquid Pb under a controlled oxygen environment, the oxidation of dissolved Fe may occur according to the relationship,

$$3\underline{Fe}_{(1\,wt\%\,in\,Pb)} + 4\underline{O}_{(1\,wt\%\,in\,Pb)} = Fe_3O_4(s) \tag{16}$$

which is the sum of the following equations for individual reactions, (a) dissolution of oxygen in Pb, (b) dissolution of Fe in Pb, and (c) oxidation of iron. If the 1 wt% standard state is selected, Eq. (4) can be rewritten as (with unit of ΔG^0 in joules),

$$\frac{1}{2}O_2(g, 1\,atm) = \underline{O}_{(1\,wt\%\,in\,Pb)} \tag{17}$$

By adding the following value to Eq. (5),

$$\Delta G_{(1\,at\% \to 1\,wt\%)} = RT\ln\frac{1\,at\%}{0.0779wt\%} = 21.1T \tag{18}$$

one can obtain the standard Gibbs free energy change for Eq. (17) from the following

$$\Delta G^0_{\underline{O}_{(1\,wt\%\,in\,Pb)}} = \Delta G^0_{\underline{O}_{(1\,at\%\,in\,Pb)}} + \Delta G_{(1\,at\% \to 1\,wt\%)} = -119100 + 35.7T \tag{19}$$

For the dissolution of iron, the iron solubility data listed in Table 2-1 can give the Gibbs free energy change for the following reaction, assuming $a^H_{Fe(1\,wt\%)} = C_{Fe,\,wt\%}$,

$$Fe(s) = \underline{Fe}_{(1\,wt\%\,in\,Pb)} \tag{20}$$

as

$$\Delta G^0_{\underline{Fe}_{(1\,wt\%\,in\,Pb)}} = -RT\ln(C_{Fe,\,wt\%}) = -2.303RT \times (0.34 - \frac{3450}{T}) = 66057.6 - 6.51T \tag{21}$$

With the equilibrium equation for solid iron when it forms magnetite (Fe_3O_4, solid) [13],

$$3Fe(s) + 2O_2(g) = Fe_3O_4(s) \tag{22}$$

for which

$$\Delta G^0_{Fe_3O_4(s)} = -1102200 + 307.4T \tag{23}$$

The overall change in Gibbs free energy corresponding to Eq. (16) can be calculated as

$$\Delta G^0_{Fe_3O_4(s)\,in\,Pb} = \Delta G^0_{Fe_3O_4(s)} - 3 \times \Delta G^0_{\underline{Fe}_{(1\,wt\%\,in\,Pb)}} - 4 \times \Delta G^0_{\underline{O}_{(1\,wt\%\,in\,Pb)}} = -823973 + 184.1T \tag{24}$$

and with the last part of Eq. (5) and assumptions of $a^H_{Fe(1\,wt\%)} = C_{Fe,\,wt\%}$, $a^H_{O(1\,wt\%)} = C_{O,\,wt\%}$, the Gibbs free energy change for Eq. (24) can be rewritten as

$$\Delta G^0_{Fe_3O_4(s)\,in\,Pb} = -RT\ln\frac{a_{Fe_3O_4(s)}}{(a^H_{Fe(1wt\%)})^3 \cdot (a^H_{O(1wt\%)})^4} = -RT\ln\frac{a_{Fe_3O_4(s)}}{(C_{Fe,\,wt\%})^3 \cdot (C_{O,\,wt\%})^4} \tag{25}$$

or, at 600°C (823K)

$$\frac{a_{Fe_3O_4(s)}}{(C_{Fe,\,wt\%})^3 \cdot (C_{O,\,wt\%})^4} = e^{91.38} \tag{26}$$

Thermodynamic saturation condition of the Pb melt with solid Fe_3O_4 occurs at $a_{Fe_3O_4(s)} = 1$. Although the interaction coefficients between Fe and O in solution are ignored, Eq. (26) is still valid as the dissolved solutes obey Henry's law and their interactions are negligible. At 600°C, the following equation is attained for equilibrium concentrations of dissolved Fe and O when liquid Pb is in thermodynamic equilibrium with Fe_3O_4

$$3\log_{10}(C_{Fe,wt\%}) = -4\log_{10}(C_{O,wt\%}) - 39.69 \tag{27}$$

With the solubility of Fe in liquid Pb at 600°C taken as 2.44 ppm (2.44×10^{-4} wt%), an oxygen concentration above 6.12×10^{-8} wt% at 600°C can be translated into the thermodynamic saturation condition for Fe_3O_4. To achieve this concentration of oxygen in liquid Pb, the oxygen partial pressure, calculated using the following modified version of Eq. (7) along with Eq. (19),

$$(C_{O,\,wt\%}) = P_{O_2}^{1/2} \exp\left(-\frac{\Delta G^0_{\underline{O}_{(1\,wt\%\,in\,Pb)}}}{RT}\right) = P_{O_2}^{1/2} \exp\left(\frac{119100 - 35.7T}{RT}\right) \tag{28}$$

can be obtained as $P_{O_2} = 1.13\times10^{-25}$ atm, and can be confirmed in Table 2-2. The corresponding P_{H_2}/P_{H_2O} is again obtained from Table 2-2 as 3.81. When P_{H_2}/P_{H_2O} is maintained above this value, the oxygen and iron concentrations dissolved liquid Pb vary according to Eq. (27) at 600°C, while maintaining the thermodynamic stability for solid Fe_3O_4. At the same time, the maximum oxygen content should also be kept below the saturation solubility in order not to form and stabilize the solid oxide of PbO which will degrade the quality of liquid Pb or LBE coolants as mentioned previously. In operating a flowing liquid Pb-alloy coolant system under a temperature gradient, the maximum oxygen content should not exceed the saturation value measured in the lowest temperature region. At the same time, the minimum content of oxygen must be maintained above the Fe_3O_4 saturation level measured in the highest temperature region, in order to provide a thermodynamically stable condition for Fe_3O_4 oxide to form as a protective oxide on the surface of iron based alloys.

Available experimental data reported by IPPE [26] is shown in Figure 2-3. It shows the transition of corrosion modes of two Fe-Cr-Ni steels tested in flowing liquid lead at 550°C. When the oxygen concentration is very low, only dissolution type of corrosion occurs. With increase in the oxygen content, the oxidation of iron mainly forming a protective Fe_3O_4 scale was attributed by authors as the major cause of preventing further dissolution.

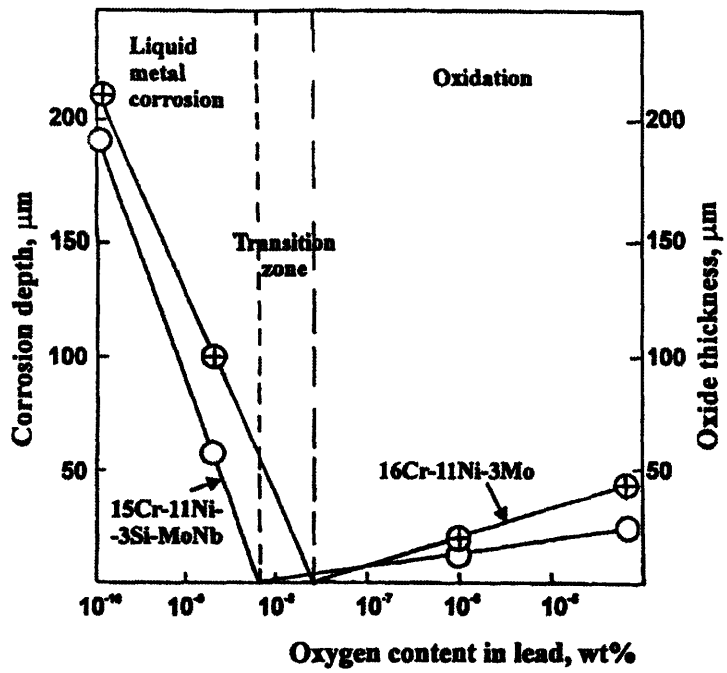

Figure 2-4 Diagram showing corrosion behavior of steels in flowing oxygen-containing lead for 3000 h at 550°C [26].

Effect of Cr Dissolution in Liquid Pb

Existence of Cr in liquid Pb or LBE can affect the dissolution process of iron in two ways: (a) by forming a surface oxide of Cr_2O_3 which is more stable and better diffusion barrier than iron oxide even at very low oxygen concentration as shown in Figure 2-3, or (b) by forming $FeCr_2O_4$ oxide reacting with dissolved iron in liquid Pb. The latter case will be examined here.

The overall reaction of forming $FeCr_2O_4$ from dissolved Fe, Cr and O can be expressed as

$$\underline{Fe}_{(1\,wt\%\,in\,Pb)} + 2\underline{Cr}_{(1\,wt\%\,in\,Pb)} + 4\underline{O}_{(1\,wt\%\,in\,Pb)} = FeCr_2O_4(s) \tag{29}$$

which can be calculated using the following equations as well as Eq. (17) & (20):

$$Fe(s) + 2O_2(g) + 2Cr(s) = FeCr_2O_4(s) \tag{30}$$

for which

$$\Delta G^0_{FeCr_2O_4(s)} = -1435070 + 273.4T \tag{31}$$

The ΔG^0 of the following equation is calculated using the Cr solubility in liquid Pb listed in Table 2-1 with the same assumptions as used in calculating $\Delta G^0_{\underline{Fe}_{(1\,wt\%\,in\,Pb)}}$,

$$Cr(s) = \underline{Cr}_{(1wt\%\,in\,Pb)} \tag{32}$$

as

$$\Delta G^0_{\underline{Cr}_{(1\,wt\%\,in\,Pb)}} = -RT\ln(C_{Cr,\,wt\%}) = -2.303RT \times (3.87 - \frac{6947}{T}) = 133015 - 74.10T \tag{33}$$

Thus, the ΔG^0 of the overall reaction in Eq.(29) is

$$\Delta G^0_{FeCr_2O_4(s)\,in\,Pb} = \Delta G^0_{FeCr_2O_4(s)} - 2\times\Delta G^0_{\underline{Cr}_{(1\,wt\%\,in\,Pb)}} - \Delta G^0_{\underline{Fe}_{(1\,wt\%\,in\,Pb)}} - 4\times\Delta G^0_{\underline{O}_{(1\,wt\%\,in\,Pb)}}$$

$$= -RT\ln\frac{a_{FeCr_2O_4(s)}}{(C_{Fe,\,wt\%})\cdot(C_{Cr,\,wt\%})^2\cdot(C_{O,\,wt\%})^4} = -1290760 + 285.3T \tag{34}$$

or, at 600°C(823K)

$$\frac{(C_{Fe,\,wt\%})\cdot(C_{Cr,\,wt\%})^2\cdot(C_{O,\,wt\%})^4}{a_{FeCr_2O_4(s)}} = e^{-143.5} \tag{35}$$

Again, the interactions between solute atoms are neglected under the assumption of Henry's law obedience. If the solid oxide of $FeCr_2O_4(s)$ is thermodynamically stable in liquid Pb, $a_{FeCr_2O_4(s)} = 1$, the relationship between the solubility of Fe, Cr and O in liquid Pb is given as

$$\log_{10}(C_{Fe,\,wt\%}) + 2\log_{10}(C_{Cr,\,wt\%}) = -4\log_{10}(C_{O,\,wt\%}) - 62.33 \tag{36}$$

indicating that the solubility of Fe is affected by the presence of Cr in the system. Therefore, when iron is alloyed with other elements which would form stable oxides combined with iron, the thermodynamic solubility of iron is affected with respect to the concentration of such elements. The beneficial alloying effects of elements added to iron result from the reduced

thermodynamic solubility of iron in liquid Pb-alloy with the presence of such element in solution, or their capability of forming more stable structural oxides even below the equilibrium oxygen potential for iron oxides. Such effect of alloying elements on the corrosion of low alloy steels in LBE is illustrated in Figure 2-5 as reported by IPPE [26].

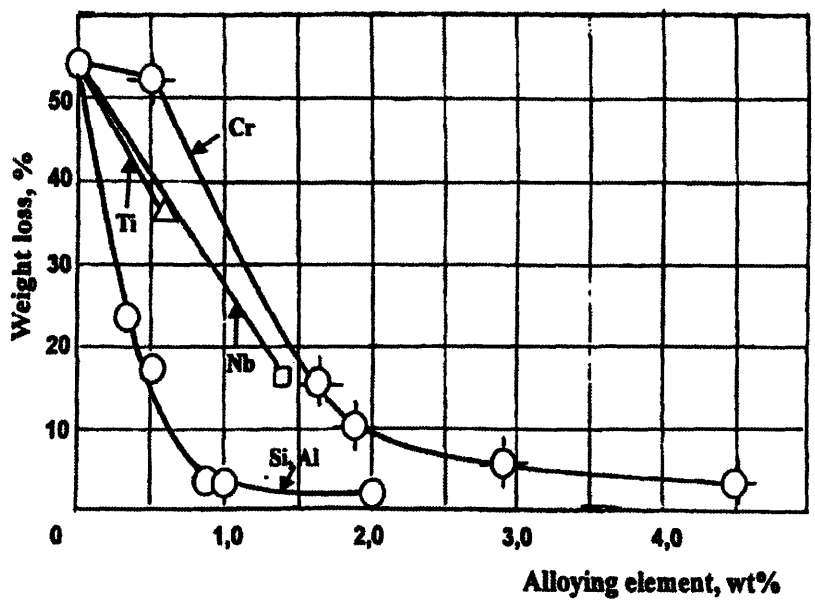

Figure 2-5 Effect of alloying elements on low alloy steel corrosion in Pb-Bi at 600°C and flow rate 6 m/s [26]

So far, the principles of oxygen control have been examined in the liquid Pb system as an example. In LBE and Bi, the same principles can be applied for the control of the oxygen content. The actual control of oxygen in a flowing liquid Pb system introduces additional complications, as there are more parameters to be considered, including: impurity effects, temperature gradient, precipitation and dissolution kinetics. Nonetheless, the reported experimental data [26-28] on steel systems tested below 550°C under an oxygen controlled environment still give credence to this approach. Thus, the central concept of oxygen control can be summarized as a way to keep the metal surface from dissolution by forming protective oxide films, of iron or other alloying elements, while avoiding the formation of solid PbO or Bi_2O_3 which will degrade the quality of coolants. From this perspective, the candidate alloying elements for iron were chosen as Cr and Si, based on the low solubility in liquid Pb-alloy, as well as the oxide stability even under very

low oxygen partial pressure condition. Therefore, the literature review in the following sections is focused on the characteristics of Fe, Cr and Si system in liquid Pb-alloy environment.

2.2 Kinetics of Liquid Metal Corrosion

2.2.1 Kinetic Process of Dissolution in Liquid Pb-alloys

In the absence of any impurity effect, the first step of solid metal dissolution occurs by the breaking of the metallic bonds between the surface atoms and the simultaneous formation of metallic bonds between the solute and solvent atoms[29]. Then the solute species diffuse through the interface layer of solid-liquid to the bulk where convection is dominant. This type of mass transfer is termed convective diffusion and the process is governed by the solubilities of solid metal elements in the liquid metal as well as the kinetics of the dissolution reaction. The rate, J, at which an elemental species enters solution, can be described as [30-31]:

$$J = K(C_0 - C) \tag{1}$$

where K is the effective solution rate constant, depending on hydrodynamic factors, C_0 is the solubility of an element in the liquid metal, C is its actual concentration in the bulk of the liquid.

Under isothermal conditions, the rate of dissolution would decrease with time as C increases and eventually become zero after the actual elemental concentration reaches the solubility limit. On the contrary, in a non-isothermal system where the dissolved element concentration (C) reaches a system-wide steady state value due to convection, there is essentially a time-invariant driving force ($\Delta C = C_0 - C$) for dissolution and deposition at a given temperature. Deposition of solute element occurs at lower temperatures in the circuit where $C_0 < C$. Therefore, a continuous transfer of materials from a hotter zone to a colder zone in the circuit would result in as depicted in Figure 1-2 in Chapter 1. Such mass-transfer process is of prime importance especially for advanced nuclear system where a large temperature gradient and high fluid velocity is essential to achieve economic viability. In dealing with experimental findings from mass transfer, it is convenient to use dimensionless numbers. The Sherwood number (Sh), which is closely related to the mass transfer coefficient and the diffusion coefficient in the liquid metal is of particular interest.

$$Sh = \frac{Kd}{D} \tag{2}$$

where K is the mass transfer coefficient (m/s), d is the characteristic specimen length (m) and D is the diffusion coefficient of the relevant species (m^2/s)

A limited number of data on the diffusion coefficients for relevant species, such as Fe and O in liquid Pb-alloys are available. For Cr, a single value has been found in the literature only for Pb-17Li system [32]. For comparison purposes, Figure 2-6 shows the diffusion coefficients of oxygen, iron and chromium available in the literature [17, 21, 32-37]. Corresponding equations from these sources summarized below. Though there exist scatter in data, the averaged diffusion coefficient of species in liquid Pb-alloy can be assumed as 10^{-9} m^2/sec at 600°C.

<u>Diffusivity of oxygen in liquid Pb</u>

$$D_{O\,in\,Pb} = 1.44\times10^{-7}\exp\left(-\frac{25940\,(J/mol)}{RT}\right) m^2/sec\ [21] \tag{3}$$

$$D_{O\,in\,Pb} = 6.62\times10^{-9}\exp\left(-\frac{16150\,(J/mol)}{RT}\right) m^2/sec\ [33] \tag{4}$$

$$D_{O\,in\,Pb} = 1.29\times10^{-9}\ m^2/sec \text{ at } 750^\circ C\ [34] \tag{5}$$

<u>Diffusivity of oxygen in liquid Bi</u>

$$D_{O\,in\,Bi} = 1.08\times10^{-6}\exp\left(\frac{-49325\,(J/mol)}{RT}\right) m^2/sec\ [17] \tag{6}$$

$$D_{O\,in\,Bi} = 1.98\times10^{-8}\exp\left(\frac{-26610(J/mol)}{RT}\right) m^2/sec\ [35] \tag{7}$$

<u>Diffusivity of Fe and Cr in liquid metals</u>

$$D_{Fe\,in\,Pb} = 4.9\times10^{-7}\exp\left(\frac{-44100(J/mol)}{RT}\right) m^2/sec\ [36] \tag{8}$$

$$D_{Fe\,in\,Pb\text{-}Bi} = 2.27\times10^{-9}\ m^2/sec \text{ at } 750^\circ C\ [37] \tag{9}$$

$$D_{Cr\,in\,Pb17Li} = 8\times10^{-11}\ m^2/sec \text{ at } 500^\circ C\ [32] \tag{10}$$

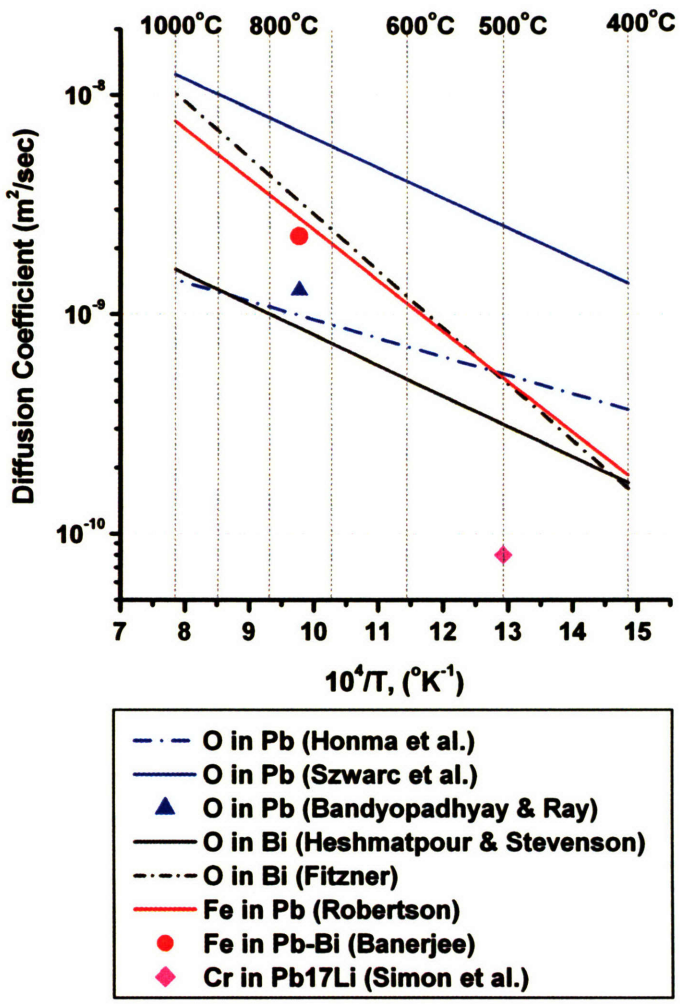

Figure 2-6 Diffusion coefficients of O, Fe and Cr in liquid Pb-alloys [17, 21, 32-37].

Balbaud-Célérier and Barbier [31] compiled empirical correlations on mass transfer coefficient developed by several researchers[38-41]. For flow in a pipe geometry, the following correlations are appropriate to use.

$$K = 0.0096 V^{0.913} d_{pipe}^{-0.087} \nu^{-0.567} D^{0.654} \text{ [38]} \tag{11}$$

$$K = 0.0165 V^{0.86} d_{pipe}^{-0.14} \nu^{-0.530} D^{0.670} \text{ [39]} \tag{12}$$

$$K = 0.0177 V^{0.875} d_{pipe}^{-0.125} \nu^{-0.579} D^{0.704} \text{ [40-41]} \tag{13}$$

where V is the flow velocity (m/s), d_{pipe} is the inside diameter of pipe, v is the kinematic viscosity (m^2/s) and D is the diffusion coefficient (m^2/s). The calculated corrosion rate using the

above correlations results in 2.4 times higher rates than the actual experimental data shows. This discrepancy was attributed to the assumptions made for the interface concentration, which was set as the saturation value, and for the bulk concentration, set to be zero [31].

The mode of flow Accelerated corrosion (FAC) in relation to the flow velocity was summarized in the same literature and is worth noting here. As shown in Figure 2-7, at low velocities, the dissolution of the species at the solid-liquid interface reaches equilibrium and the corrosion is determined by the rate of diffusion through the laminar sublayer to the bulk. In this velocity regime, so called mass transfer controlled corrosion occurs and its rate increases with increase in flow velocity. At higher velocities, the limiting process becomes the dissolution reaction occurring at the solid-liquid interface, thus the corrosion rate is independent of velocity, which process is termed as activation controlled. At much higher velocities, the loss of metals as well as the surface oxide films by erosion-corrosion is possible, so the system operation in this regime should be avoided.

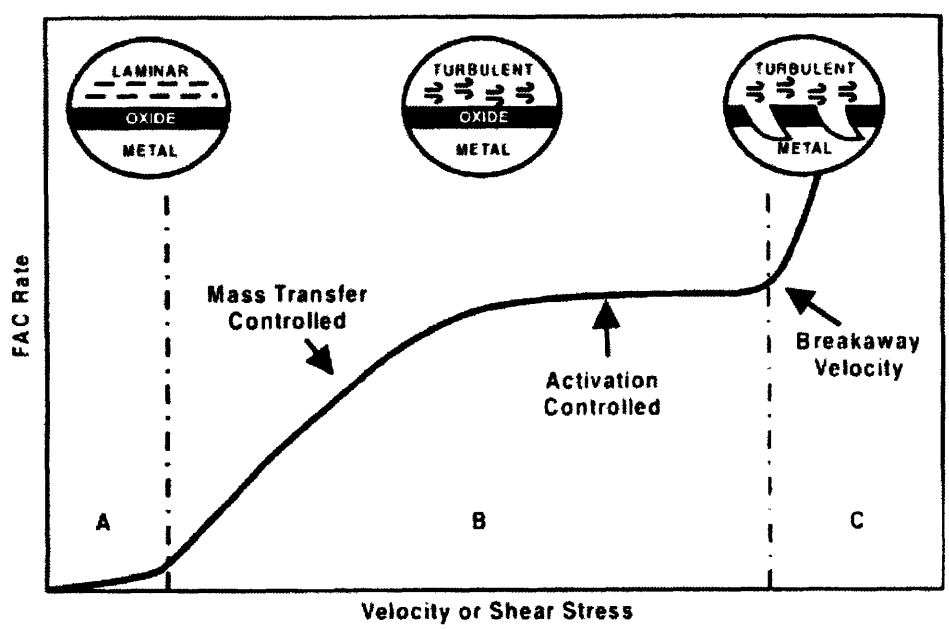

Figure 2-7 Variation of the mechanism of flow accelerated corrosion (FAC) as a function of the fluid velocity [31]

2.2.2 Oxidation Characteristics of Iron Based Alloy

As discussed earlier, the alloying effect of Cr and Si will be the major focus of present investigation, associated with the corrosion mechanisms as well as the mitigation scheme. From that perspectives, the oxide characteristics of Fe, Cr and Si will be reviewed in this section.

Formation of Iron Oxides

Oxidation of iron in air above 570°C results in a formation of multi-layered oxides, normally composed of wüstite($Fe_{1-x}O$), magnetite (Fe_3O_4), and hematite (α-Fe_2O_3). The iron-oxygen phase diagram is given in Figure 2-8 [42], which depicts the thermodynamically stable regions for Fe_3O_4 , $Fe_{1-x}O$, and Fe_2O_3. At temperatures lower than 570°C, only magnetite is stable. Hematite is formed by further oxidation of magnetite. Wüstite is only stable above 570°C and at reduced oxygen activities [43]. The multi-layer structure of iron oxides have the stacking order of: (a) an inner wüstite layer, (b) a thinner middle layer of magnetite, and (c) an even thinner outer layer of hematite [44]. Due to the rapid growth of wüstite on Fe and its highly non-stoichiometric nature (x up to 0.16), protection of low-alloy steels above 570°C can not be expected under oxidizing environment.

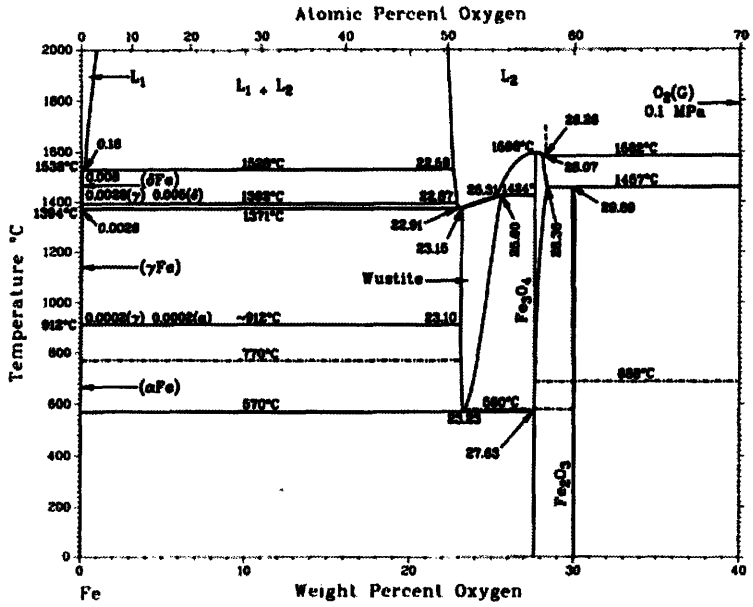

Figure 2-8 The iron-oxygen phase diagram [42].

As for crystal structure, wüstite has the rocksalt (NaCl) structure, of which the ideal form consists of an FCC anion (oxygen ion) close-packing lattice where all octahedral sites are filled with the smaller cations. Due to its high deviation from stoichiometry, the defect clustering in wüstite has a clear influence on cation diffusion [45]. At the composition of $Fe_{0.94}O$ the iron self-diffusion coefficient may be expressed as [46]

$$D_{Fe\ in\ Fe_{0.94}O} = 8.6\times10^{-7}\exp\left(\frac{-122800\,(J/mol)}{RT}\right)\ m^2/sec \qquad (1)$$

At room temperature, magnetite has the inverse spinel structure [47]. In the spinel structure, the oxygen atoms form a sublattice based on FCC closed-packing, and the metal ions occupy both the tetrahedral and octahedral sites. The unit cell consists of 32 oxygen atoms and accordingly the structure contains 32 octahedral and 64 tetrahedral sites. In a normal spinel, the trivalent metal cations occupy one-half of the octahedral sites while the divalent cations occupy one eighth of the tetrahedral sites [45]. But in the inverse spinel structure of magnetite, one eighth of the tetrahedral sites are occupied by Fe^{3+} while the octahedral sites are occupied by the Fe^{2+} and the remaining half of the Fe^{3+} ions. At higher temperatures, the randomization in the distribution of Fe^{2+} and Fe^{3+} over the occupied tetrahedral and octahedral sites are reported to occur [47]. The self-diffusion coefficient of iron when measured in a single crystal Fe_3O_4 showed a strong dependence on the oxygen activity [48-50]. If the oxygen partial pressure is lower than that of the stoichiometric composition of magnetite, the oxide becomes metal excess ($Fe_{3+y}O4$) and the interstitial-type mechanism is dominant for the diffusion of iron. On the contrary, at higher oxygen activities, it becomes metal deficient and the diffusion of iron occurs by vacancy mechanism [47, 49]. The iron tracer diffusion coefficient covering the whole magnetite range, when measured with single crystal Fe_3O_4, can be expressed as [48],

$$D_{Fe} = D_v^0 P_{O_2}^{2/3}\exp(-E_v/RT) + D_i^0 P_{O_2}^{-2/3}\exp(-E_i/RT) \qquad (2)$$

$$\text{with } D_v^0 = 3.98\times10^{-15}\,[m^2/sec];\ D_i^0 = 7.94\times10^{2}\,[m^2/sec];$$

$$E_v = -139600\,[J/mol];\ \text{and } E_i = -613200\,[J/mol]$$

By eliminating the compositional variations and using the correlation coefficient for the vacancy mechanism (f = 0.78), the vacancy diffusion coefficient was further simplified to the following equation [49].

$$D_v = 1.43\times10^{-5}\exp\left(\frac{-137000\,(\text{J/mol})}{RT}\right)[\text{m}^2/\text{sec}] \quad (3)$$

As for the nominal values of Fe self-diffusion in polycrystalline Fe_3O_4, experimental data measured with $Fe_{2.993}O_4$ by Himmel et al.[50] results in the following relationship as

$$D_{Fe\,in\,Fe_3O_4} = 5.2\times10^{-4}\exp\left(\frac{-230000\,(\text{J/mol})}{RT}\right)\text{m}^2/\text{sec} \quad (4)$$

The formation of metastable oxide of γ-Fe_2O_3 (maghemite) has been observed during the transformation process of magnetite to hematite. γ-Fe_2O_3 has the same crystalline structure (and strongly magnetic nature) as magnetite, though the composition is close to that of hematite. Nasrazadani and Raman [51] reported that the defects introduced into magnetite when heated under an oxidizing environment promote a defective spinel phase close to γ-Fe_2O_3, and the direct conversion of defect-free Fe_3O_4 to hematite (α-Fe_2O_3) does not appear to take place.

Hematite has a corundum structure, which is the HCP stacking of oxygen ions with 2/3 of the octahedral sites filled with trivalent metal ions, and the deviation from stoichiometry is known to be very small. Because of its slow growth, relatively small number of literature data are available on the growth kinetics of α-Fe_2O_3. Tracer diffusion data for Fe and O in a single crystal Fe_2O_3 show that they have comparable diffusion coefficients [52-53] and can be expressed as

$$D_{Fe\,in\,Fe_2O_3} = 1.9\times10^{5}\exp\left(\frac{-591618\,(\text{J/mol})}{RT}\right)\text{m}^2/\text{sec [52]} \quad (5)$$

$$D_{O\,in\,Fe_2O_3} = 10^{7}\exp\left(\frac{-610000\,(\text{J/mol})}{RT}\right)\text{m}^2/\text{sec [53]} \quad (6)$$

Effect of Alloying Cr

Cr_2O_3 has the corundum structure, and is the only solid oxide formed during high temperature oxidation. Because of its tendency to form protective oxide scale, Cr has been the major constituent of stainless steels and other heat-resistant alloys. The diffusion coefficients of Cr and O in Cr_2O_3 are given as

$$D_{Cr\,in\,Cr_2O_3} = 1.37\times10^{-5}\exp\left(\frac{-255642\,(J/mol)}{RT}\right)\ m^2/sec\ [54] \tag{7}$$

$$D_{O\,in\,Cr_2O_3} = 1.59\times10^{-3}\exp\left(\frac{-421747\,(J/mol)}{RT}\right)\ m^2/sec\ [55] \tag{8}$$

The addition of Cr alters the oxidation kinetics of iron alloys, offering the increased oxidation resistance even at high temperature. Figure 2-9 [56] shows the oxide scale structure and the change in the parabolic rate constant as a function of Cr content in Fe-Cr alloys.

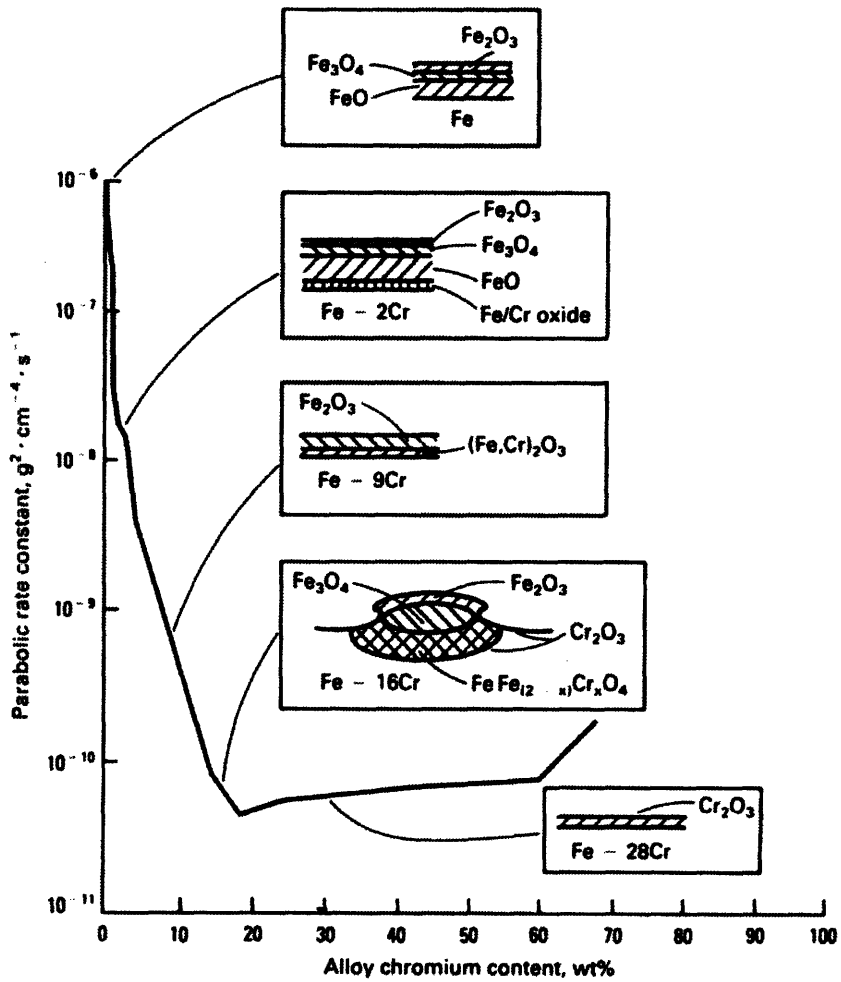

Figure 2-9 Schematic showing the effect of chromium in Fe-Cr alloys on oxidation rate and oxide scale structure based on isothermal oxidation studies at 1000°C in 0.13 atm O_2 [56]. The parabolic rate constant appearing in y-axis, k'', is defined as $(m/A)^2 = k''t$, where m is the mass increase of the specimen, A is the area over which reaction occurs, and t is the reaction time.

Effect of Alloying Si

Crystalline forms of SiO_2 occurs in three basic polymorphs: cristobalite, tridymaite and quartz [45]. Since each of these phases also has a high and low form related by a displacive transformation, more than 15 different crystalline forms of SiO_2 have been reported. As in the case of Cr, the alloying of Si to iron base material has the beneficial effect of increasing oxidation resistance. In the oxidation of dilute Fe-Si alloys (up to 5.3 wt% of Si), the relevant oxide phases formed at 500°C are Fe_3O_4, SiO_2, and Fe_2SiO_4 (fayalite) which has the structure of olivine, and belongs to orthosilicates group. The proposed mechanisms to explain increased oxidation resistance in such alloys has been summarized as: (a) the blockage of fast diffusion paths for Fe in Fe_3O_4 by Fe_2SiO_4 precipitates, (b) the formation of SiO_2/Fe_2SiO_4 at the alloy/oxide interface, acting as a diffusion barrier preventing further transport of Fe[57]. The related diffusion coefficients , including O in BCC iron, Fe and Si in Fe-Si, are given as

$$D_{O\,in\,BCC\,Fe} = 3.7\times10^{-6}\exp\left(\frac{-97283\,(J/mol)}{RT}\right)\ m^2/sec\ [58] \tag{9}$$

$$D_{Si\,in\,Fe\text{-}Si} = 7.35\times10^{-5}(1+12.4\times N_{Si})\exp\left(\frac{-219610\,(J/mol)}{RT}\right)\ m^2/sec\ [59] \tag{10}$$

$$D_{Fe\,in\,Fe\text{-}Si} = 3\times10^{-4}\exp(20\times N_{Si})\exp\left(\frac{-240800\,(J/mol)}{RT}\right)\ m^2/sec\ [60] \tag{11}$$

where N_{Si} is the mole fraction of alloyed silicon.

The diffusion coefficient of Fe^{3+} thorough the SiO_2 was reported by Atkinson [57, 61] as

$$D_{Fe^{3+}\,in\,SiO_2} = 6\times10^{-7}\exp\left(\frac{-288960\,(J/mol)}{RT}\right) m^2/sec\ [61] \tag{12}$$

Figure 2-10 summarizes the diffusion coefficients identified as Arrhenius plot and compares the relative effectiveness of each oxide as a diffusion barrier.

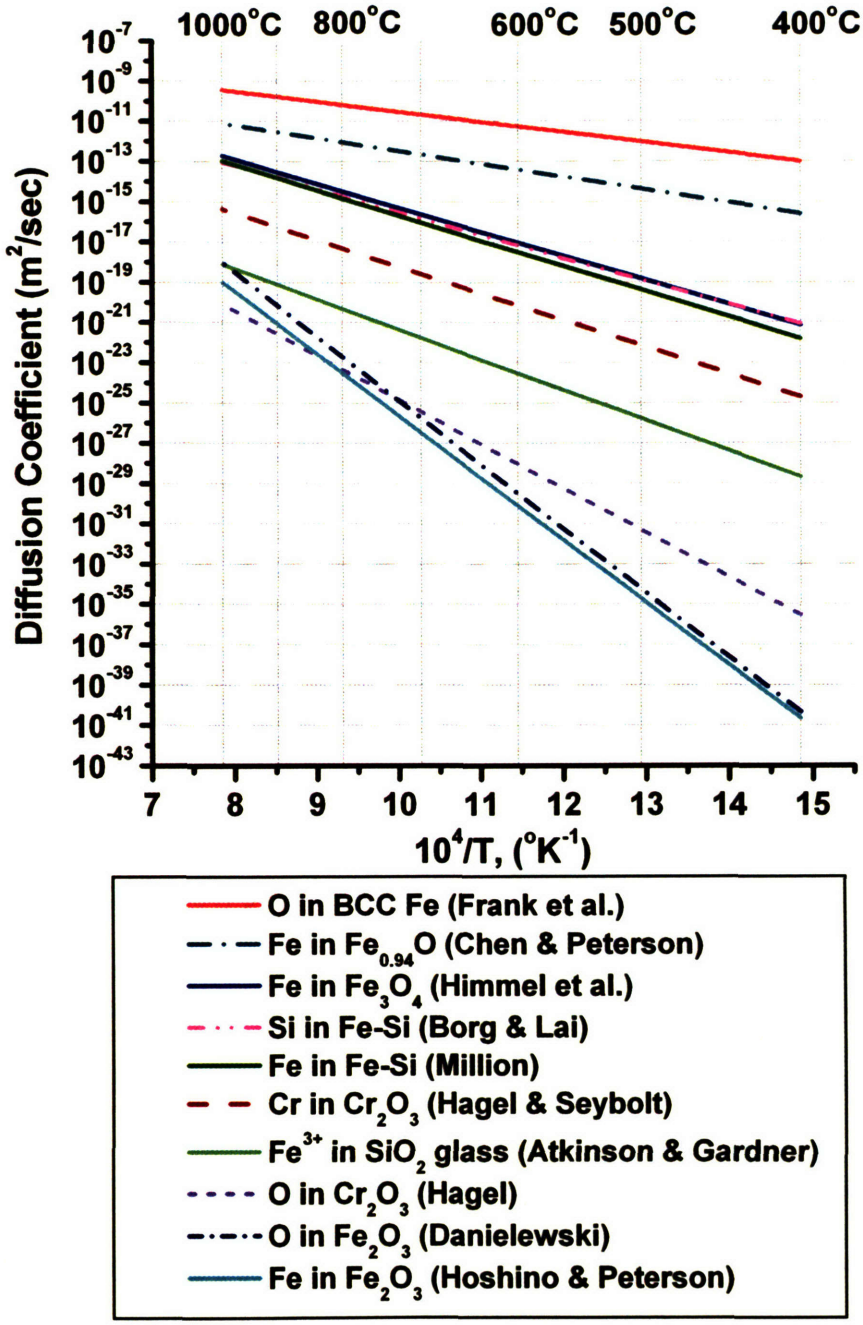

Figure 2-10 Diffusion coefficients of selected iron based materials and oxides, compiled from various sources [46, 50, 52-55, 57-61].

2.3 References

[1] G. S. Yachmenyov et al., "Problems of Structural Materials' Corrosion in Lead-Bismuth Coolant", in *Proceedings: Heavy Liquid Metal Coolants in Nuclear Technology*, Vol. 1 (HLMC-98), Obninsk, Russia, 1998, pp. 133-140.

[2] G. Müller, G. Schumacher, and F. Zimmermann, "Investigation on Oxygen Controlled Liquid Lead Corrosion of Surface Treated Steels", *Journal of Nuclear Materials*, **278** (2000) pp. 85-95.

[3] N. Li, "Active Control of Oxygen in Molten Lead-Bismuth Eutectic Systems to Prevent Steel Corrosion and Coolant Contamination", *Journal of Nuclear Materials*, **300** (2002) pp.73-81.

[4] J. R. Weeks, "Liquidus Curves of Nineteen Dilute Binary Alloys of Bismuth", *Transactions of the ASM*, **58** (1965) pp. 302-322.

[5] J. R. Weeks and A. J. Romano, "Liquidus Curves and Corrosion of Fe, Ti, Zr, and Cu in Liquid Bi-Pb Alloys", *Corrosion*, **25** (1969), pp. 131-136.

[6] H. Branover, S. Lesin, and M. Tsirlin, "Some Problems of the Corrosion and Protection of Materials in Liquid Metal MHD Generators", *Journal of Materials Science Letters*, **13** (1994) pp.508-511.

[7] D. A. Stevenson and J. Wulff, "Liquid-Solid Phase Distribution Studies in the Systems Iron-Lead, Cobalt-Lead, Chromium-Tin, and Nickel-Silver", *Transactions of the Metallurgical Society of AIME*, **230** (1964) pp.820-827.

[8] T. Alden, D. A. Stevenson, and J. Wulff, "Solubility of Nickel and Chromium in Molten Lead", *Transactions of the Metallurgical Society of AIME*, **212** (1958) pp.15-17.

[9] J. R. Weeks, "Solubility of Fe and Fe 0.8wt% C in Liquid Bi", *Transactions of the ASM*, **58** (1965) pp.426-428.

[10] C. H. P. Lupis, Chemical Thermodynamics of Materials, North-Holland, New York, 1983.

[11] N. A. Gocken, Statistical thermodynamics of Alloys, Plenum Press, New York, 1986.

[12] J. R. Weeks, "Lead, Bismuth, Tin and Their Alloys as Nuclear Coolants", *Nuclear Engineering and Design* , **15** (1971) pp.363-372.

[13] D. R. Gaskell, Introduction to the Thermodynamics of Materials, 3rd ed., Taylor & Francis, Washington, D.C., 1995.

[14] Y. A. Chang, K. Fitzner and M. X. Zhang, "The Solubility of Gases in Liquid Metals and Alloys", *Progress in Materials Science*, **32** (1988) pp.97-259.

[15] O. Kubaschewski and C. B. Alcock, Metallurgical thermochemistry, 5th ed., Pergamon Press, Oxford, 1979.

[16] C. B Alcock and T. N. Belford, "Thermodynamics and Solubility of Oxygen in Liquid Metals from E.M.F. Measurements Involving Solid Electrolytes, Part I.-Lead", *Transactions of Faraday Society*, **60** (1964) pp.822-835.

[17] K. Fitzner, "Diffusivity, Activity, and Solubility of Oxygen in Liquid Bismuth", *Thermochimica Acta*, **35** (1980) pp.277-286.

[18] S. Otsuka, T. Sano, and Z. Kozuka, "Activities of Oxygen in Liquid Bi, Sn, and Ge from Electrochemical Measurements", *Metallurgical Transactions B*, **12B** (1981) pp.427-433.

[19] S. Otsuka and Z. Kozuka, "Further Study on the Activities of Oxygen in Liquid Pb and Sb by a Modified Coulometric Titration Method", *Metallurgical Transactions B*, **12B** (1981) pp.616-620.

[20] A. Taskinen, "Thermodynamics and Solubility of Oxygen in Liquid Lead", *Scandinavian Journal of Metallurgy*, **8** (1979) pp.185-190.

[21] R. Szwarc, K. E. Oberg, and R. A. Rapp, "The Diffusivity and Solubility of Oxygen in Liquid Lead from Electrochemical Measurements", *High Temperature Science*, **4** (1972) pp.347-356.

[22] S. Otsuka and Z. Kozuka, "Activity of Oxygen in Liqud Lead and Antimony from Electrochemical Measurements", *Metallurgical Transactions B*, **10B** (1979) pp.565-574.

[23] S. Anik and M. G. Frohberg, "Thermodynamics and Solubility of Oxygen in Liquid Bismuth-Lead and Bismuth-Antimony Alloys" *Berichte der Bunsen-Gesellschaft für Physikalische Chemie*, **91** (1987) pp.790-794.

[24] A. Taskinen, "Activity Coefficient of Oxygen in Pb-Bi and Pb-Sb Melts", *Zeitschrift für Metallkunde*, **73** (1982) pp.163-168.

[25] J. P. Hajra, M. Wang, and M. G. Frohberg, "Applicability of an Interaction Parameter Based Model to the Thermodynamic Behaviour of Oxygen in Liquid Alloys", *Zeitschrift für Metallkunde*, **81** (1990) pp.255-260.

[26] I. V. Gorynin et al., "Structural materials for power plants with heavy liquid metals as coolants", in *Proceedings: Heavy Liquid Metal Coolant in Nuclear Technology*, Vol. 1 (HLMC-98), Obninsk, Russia, pp.120-132.

[27] G. Muller et al., "Results of Steel Corrosion Tests in Flowing Liquid Pb/Bi at 420-600°C after 2000h", *Journal of Nuclear Materials*, **301** (2002) pp.40-46.

[28] H. Glasbrenner et al., "Corrosion Investigations of Steels in Flowing Lead at 400°C and 550°C", *Journal of Nuclear Materials*, **296** (2001) pp.237-242.

[29] J. R. Weeks and C. J. Klamut, "Liquid Metal Corrosion Mechanisms", *Proceedings of the Conference on Corrosion of Reactor Materials*, IAEA, (1962), pp. 105-132.

[30] P.F. Tortorelli and S.J. Pawel, "Corrosion by Liquid Metals", *Corrosion: Fundamentals, Testing, and Protection*, Vol 13A, *ASM Handbook*, ASM International, 2003, pp. 129–134.

[31] F. Balbaud-Celerier and F. Barbier, "Investigation of Models to Predict the Corrosion of Steels in Flowing Liquid Lead Alloys", *Journal of Nuclear Materials*, **289** (2001) pp.227-242.

[32] N. Simon, T. Flament, and A. Terlain, "Determination of the Diffusion Coefficients of Iron and Chromium in Pb17Li", *International Journal of Heat and Mass Transfer*, **38** (1995) pp.3085-3090.

[33] S. Honma, N. Sano, and Y. Matsushita, "Electrochemical Measurement of the Diffusivity of Oxygen in Liquid Lead", *Metallurgical Transactions*, **2** (1971) pp.1494-1496.

[34] G. K. Bandyopadhyay and H. S. Ray, "Kinetics of Oxygen Dissolution in Molten Lead", *Metallurgical Transactions*, **2** (1971) pp.3055-3061.

[35] B. Heshmatpour and D. A. Stevenson, "An Electrochemical Study of the Solubility and Diffusivity of Oxygen in the Respective Liquid Metals Indium, Gallium, Antimony and Bismuth", *Journal of Electroanalytical Chemistry*, **130** (1981) pp.47-55.

[36] W. M Robertson, "Diffusion of Cobalt and Iron in Liquid Lead Measured by Grain Boundary Grooving", *Transactions of the Metallurgical Society of AIME*, **242** (1968) pp.2139-2142.

[37] Cited in [31] as S. Banerjee, *in: Proceedings of the Fifth International Congress on Metallic Corrosion*, Tokyo, Japan, May 21-27, NACE, Houston, Texas, 1974.

[38] P. Harriott and R. M. Hamilton, "Solid-liquid Mass Transfer in Turbulent Pipe Flow", *Chemical Engineering Science*, **20** (1965) pp.1073-1078.

[39] F. P. Berger and K. -F. F. -L. Hau, "Mass-Transfer in Turbulent Pipe-Flow Measured by Electrochemical Method", *International Journal of Heat and Mass Transfer*, **20** (1977) pp.1185-1194.

[40] D. C. Silverman, "Rotating Cylinder Electrode for Velocity Sensitivity Testing", *Corrosion*, **40** (1984) pp.220-226.

[41] D. C. Silverman, "Rotating Cylinder Electrode-Geometry Relationships for Prediction of velocity-Sensitive Corrosion", *Corrosion*, **44** (1988) pp. 42-49.

[42] Alloy Phase Diagrams, Vol. 3, Metals Handbook Desk Edition, Second Edition, ASM International, 1998, in ASM Handbooks Online, http://www.asmmaterials.info ASM International, 2004.

[43] P. Kofstad, Nonstoichiometry, diffusion, and electrical conductivity in binary metal oxides, Wiley-Interscience, New York, 1972.

[44] A. Atkinson, "Transport Processes during the Growth of Oxide Films at Elevated Temperature", *Reviews of Modern Physics*, **57** (2) pp.1985 437-470.

[45] Y. M. Chiang, D. P. Birnie, and W. D. Kingery, Physical Ceramics: Principles for Ceramic Science and Engineering, John Wiley & Sons, Inc., New York, 1997.

[46] W. K. Chen and N. I. Peterson, "Effect of the Deviation from Stoichiometry on Cation Self-Diffusion and Isotope Effect in Wüstite, $Fe_{1-x}O$", *The Journal of Physics and Chemistry of Solids*, **36** (1975) pp.1097-1103.

[47] P. Kofstad, High Temperature Corrosion, Elsevier Applied Science, New York, 1988.

[48] R. Dieckmann and H. Schmalzried, "Defects and Cation Diffusion in Magnetite (I)", *Berichte der Bunsen-Gesellschaft*, **81** (1977) pp.344-347.

[49] R. Dieckmann and H. Schmalzried, "Defects and Cation Diffusion in Magnetite (II)", *Berichte der Bunsen-Gesellschaft*, **81** (1977) pp.414-419.

[50] Cited in [43] as L. Himmel, R. F. Mehl, and C. E. Birchenall, *Transactions of the Metallurgical Society of AIME*, **197** (1953) p. 822.

[51] S. Nasrazadani and A. Raman, "The Application of Infrared Spectroscopy to the Study of Rust Systems – II. Study of Cation Deficiency in Magnetite Produced During its Transformation to Maghemite and Hematite", *Corrosion Science*, **34** (1993) pp.1355-1365.

[52] N. L. Peterson, "Diffusion Mechanisms and Point Defects in Transition Metal Oxides", *Crystal Lattice Defects and Amorphous Materials*, **12** (1985) pp.59-78.

[53] M. Danielewski, "Kinetics of Gaseous Corrosion Processes", Corrosion: Fundamentals, Testing, and Protection, Vol. 13A, *ASM Handbook*, ASM International, 2003, pp. 97–105.

[54] W. C. Hagel and A. U. Seybolt, "Cation Diffusion in Cr_2O_3", *Journal of the Electrochemical Society*, **108** (1961) pp. 1146-1152.

[55] W. C. Hagel, "Oxygen-Ion Diffusion in Hematite", *Transactions of the Metallurgical Society of AIME*, **236** (1966) pp.179-184.

[56] I. G. Wright, in: Metals Handbook, 9th ed., Vol. 13, Corrosion , ASM International, Metals Park, OH, 1987, p.97

[57] A. Atkinson, "A Theoretical Analysis of the Oxidation of Fe-Si Alloys Corrosion", *Science*, **22** (1982) pp.87-102.

[58] W. Frank, H.-J. Engell, and A. Seeger, "Solubility and Interstitial Migration of Oxygen in BCC Iron", *Transactions of the Metallurgical Society of AIME*, **242** (1968) pp.749-750.

[59] R. J. Borg and D. Y. F. Lai, "Diffusion in a-Fe-Si Alloys", *Journal of Applied Physics* **41** (1970) pp.5193-5200.

[60] B. Million, "Diffusion of Fe-59 in α-Fe-Si Alloys", *Czechoslovak journal of physics*, **B27** (1977) pp.928-934.

[61] A. Atkinson and J. W. Gardner, "The Diffusion of Fe^{3+} in Amorphous SiO_2 and the Protective Properties of SiO_2 Layers", *Corrosion Science*, **21** (1981) pp.49-58.

CHAPTER 3

EXPERIMENTAL PROCEDURES

To investigate the alloying effects of chromium and silicon with iron associated with the corrosion mechanisms in liquid Pb-alloy, a test facility was developed to conduct high temperature, static immersion tests on model alloys under controlled atmosphere. By design, an isothermal static test focuses on the interaction layer formation and its characterization. The experimental system was best optimized to operate at very low oxygen partial pressure at high temperature in an effort to encourage the dissolution process as a way to evaluate compatibility of materials in limited test duration. In this chapter, the results of the corrosion test and details of characterization will be provided.

3.1 Material

Iron alloys containing Cr and/or Si were chosen for investigation in an effort to elucidate corrosion and protection mechanisms in iron based alloy as discussed in the previous chapter. Upon considerations of the metallurgical stability under irradiation environment, iron alloys with Cr content up to 18 wt% and Si up to 2.5 wt% were selected as the primary materials for investigation.

The lack of nickel eliminates the possibility of selective corrosion to occur and a lack of other austenite formers assures a BCC structure. Minimization of carbon in alloys ensures their high temperature usage by circumventing temperature limitations imposed due to embrittlement issues common in carbide strengthened steels. Based on this reasoning, along with the intentions to eliminate complications in analysis, custom melting of Fe-Cr and Fe-Cr-Si alloys was used to produce experimental Fe-Si, Fe-Cr and Fe-Cr-Si alloys. Fe-Si alloys, which are able to be obtained from commercial sources were selected to contain other impurities, if any, at their lowest level possible. The nominal composition of material chemistry is given in Table 3-1.

Eight Fe-Cr and Fe-Cr-Si alloys (alloy ID from C1 to CS8 listed in Table 3-1) were custom made by General Electric Global Research located at Niskayuna, NY. The alloy melting was performed under high purity argon and repeated several times to assure compositional homogeneity. After melting, fast cooling of the melt onto a water-cooled copper crucible was conducted. The as-received alloys had dimensions of 7.62 cm(3") diameter by 1.91 cm(0.75") thickness. They were then homogenized at 1200°C for 10 hours under dry Ar/H_2 atmosphere at the high temperature furnace facilities at MIT . In order to even out the surface inhomogeneity of existing seams, further processing steps were taken as follows. First, the alloys were cold rolled, down to 0.56 cm(0.22") thickness in LANL (Los Alamos National Laboratory) with the setting of rolling mill being 0.127 cm(0.05") per pass. A series of subsequent annealing and cold rolling steps continued at MIT. Alloys were annealed for 1 hour at 750°C under dry Ar /H_2 mixture in between each rolling procedure that produced total 50% of thickness reduction with the mill setting of 0.0318 cm(0.0125") reduction per pass. The final form of alloys was obtained as 0.127cm (0.05") thick sheet and their compositions were verified by EPMA (Electron Probe Micro-Analysis), showing limited compositional deviations from the nominal composition of ±0.5% for Cr and ±0.05% for Si.

Four Fe-Cr-Si alloys (alloy ID from CS9 to CS12 listed in Table 3-1) were made by casting and solid Hot Isostatic Pressing (HIP) methods from Metalmen Sales Inc., Long Island City, NY. Alloys were obtained in the form of plate with 30.5cm×30.5cm×2.54cm (12"×12"×1") dimensions. The remaining three Fe-Si alloys were purchased in a commercially available sheet form from the same vender. No further processing was done on these materials except for de-scaling. The detailed chemistry report from this vender is listed in Table 3-2 for 3 Fe-Si and 4 Fe-Cr-Si alloys.

Prior to corrosion testing, each alloy was evaluated to characterize the microstructure. After sectioning, wet grinding and polishing, a final surface finish for optical microscopy was produced by polishing with 0.5 μm Al_2O_3 powder. The Fe-Si and Fe-Cr alloys were chemically etched with 2% natal solution. Fe-Cr-Si alloys were etched with a mixed solution of 15-mL HCl, 10-mL HNO_3, 10-mL acetic acid and 2 drops of glycerol. Optical micrographs showed an as-cast

microstructure with large and isotropic grains. No rolling structure was found in alloys, except for alloy S2 (Fe-2.55wt% Si) containing slightly elongated grains toward the rolling direction. Test samples were cut to the dimension of 2.54cm × 1.27cm × 0.1cm ~ 0.2cm (1" × 0.5"× 0.04~0.08"). After a series of grinding steps with SiC paper, the final finish was achieved with 3μm size diamond paste in order to assure defect free surface condition. An alumina crucible of 99.8% purity (Vesuvius McDanel, model ACN-3766) was used as a container for each sample to be immersed in 350g of Pb-Bi eutectic. a granule form of high purity Pb and Bi (Surepure Chemetals, each 99.99% pure) were mixed to the eutectic composition. The impurity analysis data on the Pb and Bi are provided in Table 3-3.

Table 3-1 Nominal compositions of selected alloys for Pb-Bi eutectic corrosion tests.

Material	ID	Nominal Composition (in wt%)
Fe-Si alloys	S1	Fe-1.25% Si
	S2	Fe-2.55% Si
	S3	Fe-3.82% Si
Fe-Cr alloys	C1	Fe-1% Cr
	C2	Fe-2.25% Cr
	C3	Fe-9% Cr
	C4	Fe-12% Cr
	C5	Fe-18% Cr
Fe-Cr-Si alloys	CS6	Fe-2.25% Cr-0.5% Si
	CS7	Fe-2.25% Cr-1.25% Si
	CS8	Fe-12% Cr-0.5% Si
	CS9	Fe-12% Cr-1.25% Si
	CS10	Fe-18% Cr-0.5% Si
	CS11	Fe-18% Cr-1.25% Si
	CS12	Fe-18% Cr-2.55% Si

Table 3-2 Chemistry data of Fe-Si and Fe-Cr-Si alloys.

Alloy ID	Chemical Composition (wt%)										
	Si	C	P	S	Mn	Cr	Ni	Mo	Cu	Co	Fe
S1	1.24	0.010	0.006	0.001	0.04	0.09	0.08	0.01	0.03	0.01	Bal
S2	2.55	0.017	0.003	0.001	0.12	0.08	0.15	0.01	0.03	0.01	Bal
S3	3.82	0.011	0.022	0.025	0.24	-	-	-	-	-	Bal

Alloy ID	Nominal Composition (wt%)	Actual Chemical Composition (wt%)		
		Cr	Si	Fe
CS9	Fe-12%Cr-1.25%Si	12.02	1.28	Bal
CS10	Fe-18%Cr-0.5%Si	18.04	0.49	Bal
CS11	Fe-18%Cr-1.25%Si	17.99	1.27	Bal
CS12	Fe-18%Cr-2.55%Si	17.98	2.50	Bal

Table 3-3 Chemistry data of high purity Pb and Bi.

Liquid metal	Purity (%)	Maximum Impurities (ppm)									
		Pb / Bi	Ag	Cu	Sn	As	Fe	Ni	Sb	Cd	Zn
Pb	99.99	2.7 (Bi)	< 1	< 1	< 5	< 1	< 1	-	< 5	4	< 1
Bi	99.99	2.8 (Pb)	3.3	0.9	-	-	< 0.6	< 0.9	< 3	< 0.2	< 0.2

3.2 System Description

As discussed in the previous chapter, the control of the oxygen potential is critical to the development of a fundamental understanding on the corrosion phenomena of structural metals contacting Pb or Pb-Bi alloys. Since the required oxygen concentration is very low, instrumentation for direct control and measurement is not available. Instead, by controlling the content of gaseous H_2 and H_2O assuming the equilibrium reaction with O_2 as described in section 2.1.3, the partial pressure of oxygen can be maintained in the range of stability for oxides

of interest. With the aid of the Ellingham diagram (Figure 2-3) developed in the previous chapter, the partial pressure ratios of H_2 and H_2O corresponding to the oxygen partial pressure required can be selected.

For the purpose of this research, the oxygen concentration of Pb-Bi eutectic had to be maintained at a level lower than Fe/Fe_3O_4 equilibrium (reducing condition for Fe) but higher than Si/SiO_2 and Cr/Cr_2O_3 (oxidizing condition for Si and Cr) equilibrium. This will make possible the investigation on the effectiveness of oxide film formed by Si and Cr, while suppressing fast growing Fe-oxides that consume materials significantly as discussed in detail in the previous chapter.

To achieve the oxygen partial pressure level at this low value, a special gas treatment system was constructed to remove any oxygen impurities present in commercial gas products. The system was designed to use two gas streams, an inert argon carrier gas stream and a hydrogen gas stream. Argon is directed first to a high temperature oxygen gettering furnace. A titanium charge inside of the furnace is oxidized by the impurity oxygen and moisture in the Ar stream leaving the outlet gas virtually oxygen and moisture free. A measurement unit for monitoring oxygen and moisture concentrations were installed downstream of the oxygen gettering furnace to ensure its performance. Oxygen in the hydrogen stream is combined with hydrogen to form water vapor by passing the stream over a palladium catalyst, followed by a dryer to remove moisture. The oxygen-removed gases are mixed together using mass control valve to achieve and maintain the hydrogen concentration at 4%. The oxygen and moisture concentration of the gas stream is monitored after mixing and then directed to the test system by passing through feedthroughs on the cover of a vacuum-tight stainless steel vessel. This vessel (shown in the inset of Figure 3-1), which passed a helium leak test to confirm leak rate less than 10^{-7}cc/sec, serves as a boundary from the environment. As an added protection, a seamless stainless crucible is placed inside of the vessel as a lining to protect the outer welded stainless steel vessel from any possible LBE spill with a possible cracking of alumina crucible inside. The vessel is placed in a crucible type, single zone furnace with a programmable controller getting control input from a thermocouple placed near the lower side of stainless steel vessel. Another thermocouple probe protected by high purity alumina tube is immersed in the LBE (contained in an alumina crucible) for temperature measurement during the test. The temperature readings along with the oxygen and

moisture concentrations were recorded with a data acquisition system connected to a PC. The schematic diagram in Figure 3-1 illustrates the overall experimental configuration with an emphasis on the cover gas controlling and monitoring system to achieve desired level of oxygen partial pressure.

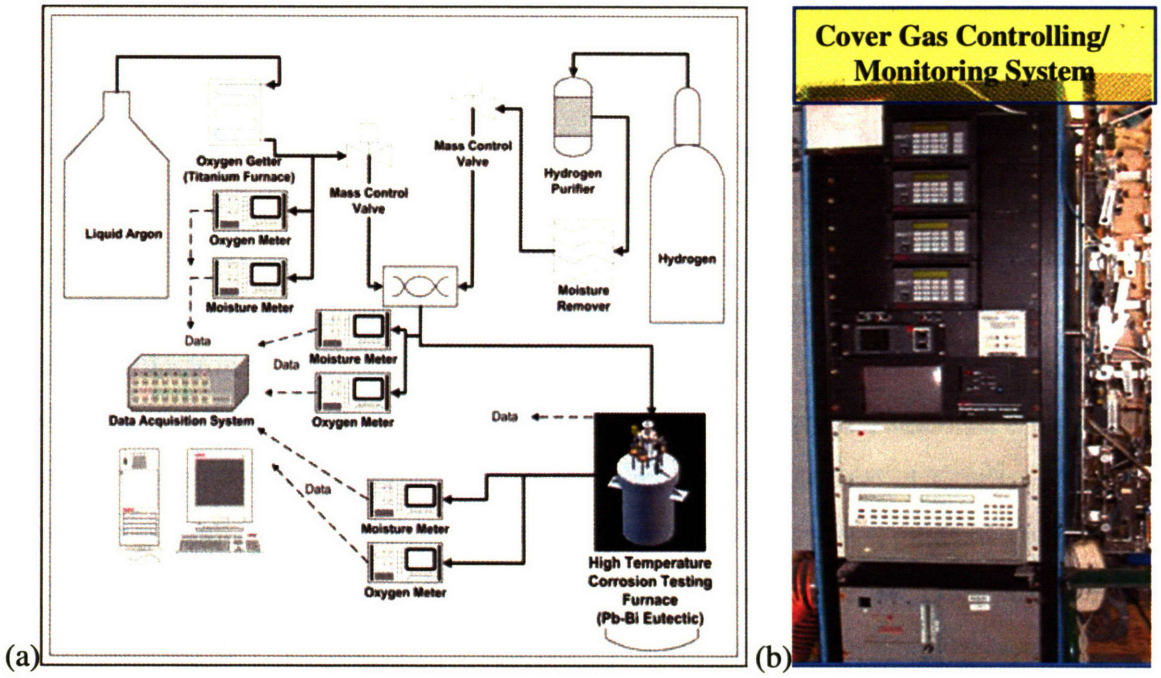

Figure 3-1 (a) Schematic diagram showing of arrangement of furnace, reaction chamber (inset), and gas conditioning paths used for LBE corrosion tests (b) an in-house built rack with integrated cover gas controlling/monitoring ability, also equipped with data acquisition system.

3.3 Testing and Analysis Procedures

Overall, fifteen different Fe-Si, Fe-Cr and Fe-Cr-Si alloys were tested at 600°C with varying exposure time under oxidizing conditions only with respect to Cr and Si. During the test the P_{H_2} / P_{H_2O} ratio was maintained at ~1000 as in Figure 2-3. As a token to confirm the cover gas

oxygen partial pressure, pure iron and Fe-18wt%Cr-2.55wt%Si alloy were placed near static testing specimens but without contacting LBE. Table 3-4 lists the test durations for each alloy.

After test, samples were cold-mounted using epoxy resin (Beuhler, Epoxide Resin No. 20-8130-128), and hardner (Buehler, Epoxide Hardner No. 20-8132-032) with a mass ratio of 5:1(epoxy : hardner). They were ground and polished with SiC paper and water, down to 1200 grit, and then with 6μm and 1μm diamond pastes. Final surface preparation was done with 0.05μm Al_2O_3 paste. Specimens processed with this surface finish were examined after carbon coating using SEM (Secondary Electron Microscopy) equipped with an EDX(Energy Dispersive X-ray Analysis) system in order to characterize the morphology and qualitative elemental distribution of interaction layers. High resolution micrographs and elemental distribution maps were obtained as a result. The same samples were also examined for a quantitative analysis using EPMA (Electron Probe Micro-analysis) equipped with a WDS (Wavelength Dispersive Spectrometry) system. With calibrated detectors using the elemental standard samples of interest, quantified compositional information was obtained for each element in weight percent as well as in atomic percent. In spite of limited spatial resolution of 1 μm, this analysis method is regarded as being highly effective in obtaining averaged compositional data, from which the effect of alloy chemistry can be related to the constituents variation in the interaction layer.

In addition, XRD (X-Ray Diffraction) analysis to obtain information on phase formation, and XPS (X-ray Photoelectron Spectroscopy) to reveal the chemical binding structure of surface film were also conducted for selected samples. In both analyses, no additional sample preparation was done other than selective cutting of the sample avoiding portions containing thick residue of LBE. Especially for XPS, of which spectral data was collected from the surface film of only several atomic layers deep, but of tens of square micrometer wide, great care was taken to illuminate only the revealed oxide film with X-ray source while avoiding any thick LBE residue formed on sample surface.

As for the compositional changes in LBE bath due to elemental dissolution, ICP-MS (Inductively coupled plasma-Mass spectroscopy) was used to examine changes in Fe, Cr and Si concentrations which may have occurred during a test.

Table 3-4. Summary of static LBE test matrix conducted at 600°C under controlled atmosphere of $P_{H_2} / P_{H_2O} \sim 1000$.

Composition of Alloy (wt%)	Specimen ID	Test Duration			
		100-hour	250-hour	300-hour	500-hour
Fe-1.25% Si	S1	√	-	√	-
Fe-2.55% Si	S2	√	-	√	-
Fe-3.82% Si	S3	√	-	√	-
Fe-1% Cr	C1	√	√	-	√
Fe-2.25% Cr	C2	√	√	-	√
Fe-9% Cr	C3	√	√	√	√
Fe-12% Cr	C4	√	√	√	√
Fe-18% Cr	C5	-	√	√	√
Fe-2.25% Cr-0.5% Si	CS6	√	√	-	√
Fe-2.25% Cr-1.25% Si	CS7	-	√	√	√
Fe-12% Cr-0.5% Si	CS8	√	√	-	√
Fe-12% Cr-1.25% Si	CS9	√	√	√	√
Fe-18% Cr-0.5% Si	CS10	√	√	-	√
Fe-18% Cr-1.25% Si	CS11	√	√	√	√
Fe-18% Cr-2.55% Si	CS12	√	√	√	√

CHAPTER 4

RESULTS

4.1 Samples Tested in the Cover Gas Condition

To assess the oxygen concentration in the cover gas, samples of Fe-18%Cr-2.55%Si and pure iron (99%) were placed inside of the furnace without contacting LBE. Figure 4-1 shows the appearance of those two samples collected after 250 and 500-hour tests, respectively. After 250-hour test at 600°C, Fe-18%Cr-2.55%Si sample was covered with semi-transparent blue oxide, while the Fe sample showed almost the same appearance as before the test with shiny metallic reflection, indicating that no measurable iron oxide layer had been formed on the surface even after 500-hour exposure at 600°C.

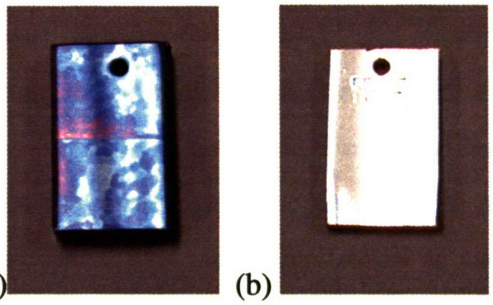

Figure 4-1 Visual observation of samples tested in cover gas condition at 600°C: (a) Fe-18%Cr-2.55%Si from 250-hour test and (b) Fe(99%) from 500-hour test.

XRD patterns were obtained from the Fe-18%Cr-2.55%Si surface using an X-ray diffractometer (Rigaku 185mm rotating anode X-ray generator, copper anode) and is shown in Figure 4-2. Small peaks indicating the presence of silicon oxide (SiO_2) and chromium oxide (Cr_2O_3) phases can be seen from the spectra. The major peaks, however, are identified as body-centered cubic (BCC) phase peaks of the bulk material and listed with Miller indices, which indicates that a very thin oxide (Cr, Si) film has been formed on the sample surface but not iron oxide.

To further characterize the chemical binding state of the thin surface film, XPS spectra using Kratos AXIS Ultra Imaging X-ray Photoelectron Spectrometer (by monochouromated Al Kα small-spot source, E=1486.6 eV) were measured in both survey and high resolution modes. All of the spectral data were acquired using the same photon source and charge-corrected to adventitious hydrocarbon at 285.0 eV as the surface oxide might be insulating to some degree.

In the survey spectra obtained at intervals of 1.0 eV of binding energy shown in Figure 4-3, no iron peak was detected, indicating no presence of it in the surface oxide film. Meanwhile, strong peaks at the Cr, O and C binding energies were detected, along with other minor peaks at Si, and LBE (possibly from vapor accumulated on the surface) energies. High carbon intensity on the surface may have resulted from the long-term testing in atmospheric environment where hydrocarbons can access and their concentration can build up.

The high resolution XPS spectra (intervals of 0.1 eV binding energy) for Cr and Si are shown in Figures 4-4 (a) and (b), and compared to the reference peak positions in the literature [1]. The chemical states of Cr agrees well with the Cr in Cr_2O_3, and Si with Si in SiO_2, indicating the formation of Cr_2O_3 and SiO_2 oxides under cover gas condition at 600°C. When combined with the survey data showing no iron presence in the oxide film, these findings can be concluded that the oxygen partial pressure in the cover gas, supposed to be maintained well below the equilibrium values of iron/iron-oxides, was indeed controlled as such, allowing only Cr and Si oxides to be formed during the exposure.

However, the presence of iron oxides observed on the surfaces originated from residual oxides of Pb and Bi and/or oxygen dissolved in the Pb and Bi. The initial oxidation of iron resulted from the reaction of this oxygen and/or with Pb and Bi surface oxides as observed in early stages of exposure. However, due to the very low oxygen partial pressure maintained in the cover gas, which was evidenced by the lack of scale formation some samples and the high oxygen diffusivity in LBE, the complete removal of initial oxygen was believed to occur in the first 30 hours of exposure, leaving the LBE in equilibrium with the cover gas composition. Further explanation and discussion will be given in the relevant sections.

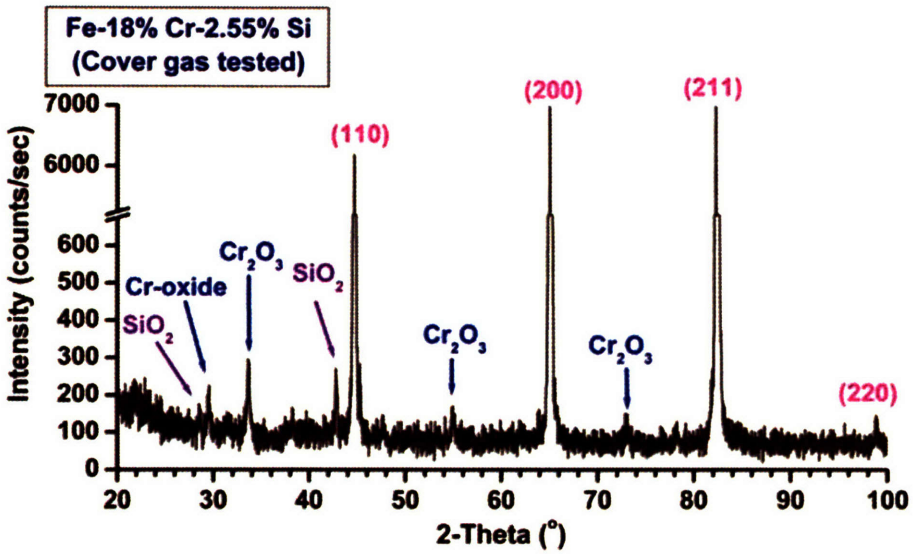

Figure 4-2 XRD patterns for oxide film formed on the Fe-18%Cr-2.55%Si sample placed in cover gas atmosphere during the 250-hour test conducted at 600°C. BCC-phase peaks are indicated by Miller indices. Minor oxide peaks are magnified by rescaling ordinate below 600 counts/sec.

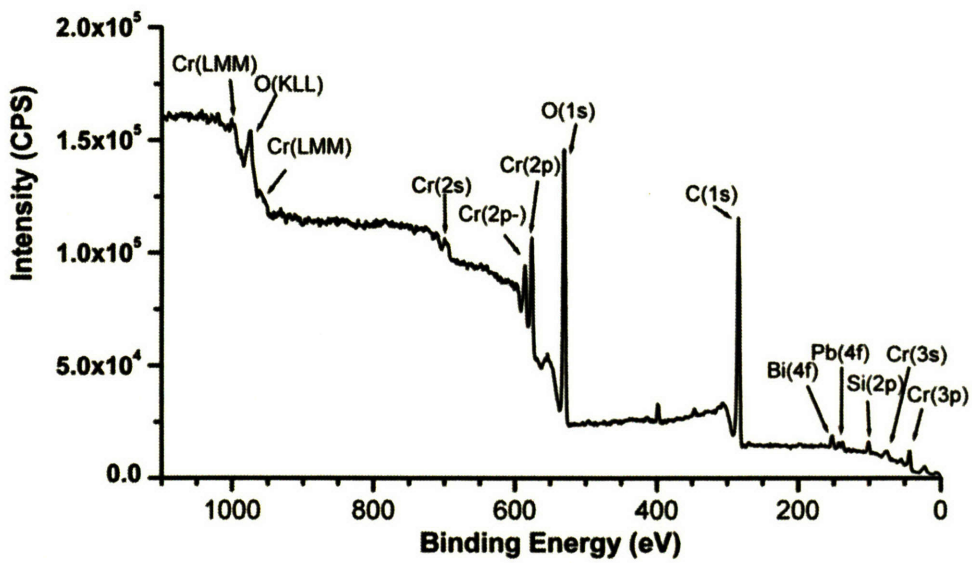

Figure 4-3 XPS survey spectra for Fe-18%Cr-2.55%Si sample tested in cover gas condition for 250 hours at 600°C. Spin-orbit splitting of Cr is represented by Cr(2p-) for Cr($2p_{1/2}$), and Cr(2p) for Cr($2p_{3/2}$).

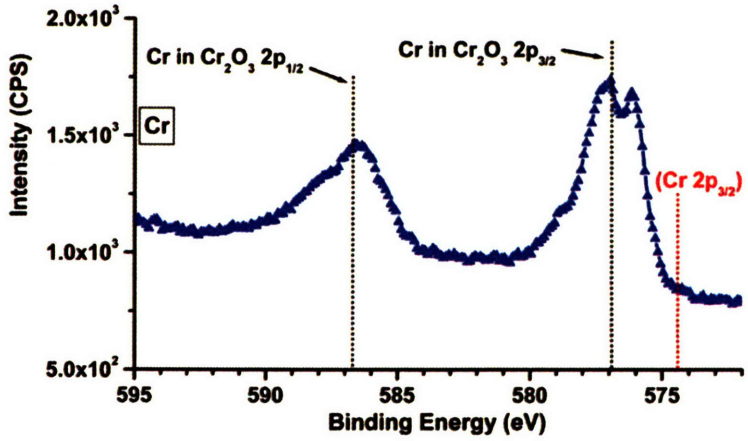

(a)

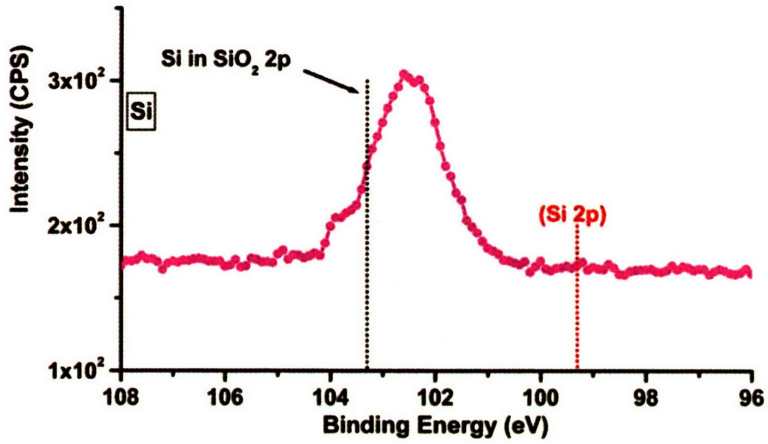

(b)

Figure 4-4 XPS high-resolution spectra of (a) Cr and (b) Si obtained from Fe-18%Cr-2.55%Si sample tested in cover gas condition for 250 hours at 600°C, presented with a charge correction to adventitious hydrocarbon at 285.0eV.

4.2 Dissolution of Elements

Solidified LBE samples collected from each alumina container of 8 alloys (Fe-1%Cr, Fe-2.25%Cr, Fe-2.25%Cr-0.5%Si, Fe-12%Cr-0.5%Si, Fe-12%Cr-1.25%Si, Fe-18%Cr-0.5%Si, Fe-18%Cr-1.25%Si, and Fe-18%Cr-2.55%Si) were analyzed using ICP-MS to investigate dissolved

Fe, Cr and Si concentrations. Si concentration was below the detection limit for all samples. Dissolved Fe and Cr concentrations are shown in Figure 4-5 observed after 100-hour exposure to 600°C LBE. There is no direct correlation between the dissolved Fe and Cr concentrations, nor any dependence on the alloy composition. However, slightly higher Cr dissolution in alloys containing low Cr was observed in general. Considering the solubility limits of Fe (10 ppm) and Cr (23 ppm) in equilibrium with LBE at 600°C, it was assumed that the solubilities of Fe and Cr in the LBE bath reached the thermodynamic equilibrium for the longer term exposure times.

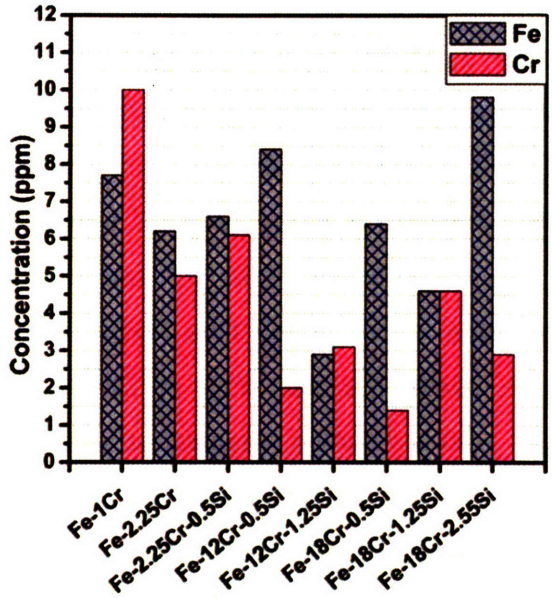

Figure 4-5 ICP-MS analysis data on solidified LBE bath after 100-hour 600°C test.

4.3 Corrosion Behavior of Fe-Cr Alloys

Depending on the Cr concentrations in the Fe-Cr alloy, the experimental results at 600°C show distinctive features generic to each concentration of Cr. In this section, the experimental results for each Fe-Cr alloy are provided individually in great detail, specifically focused on the nature of oxide film formation and its stability with increase in exposure duration.

4.3.1 Fe-1%Cr

After testing at 600°C for 100-, 250-, and 500-hour, Fe-1wt%Cr samples were analyzed using scanning electron microscopy (SEM, with a FEI/Philips XL30 FEG ESEM) equipped with an

EDS detector, to examine the morphological characteristics and elemental distribution within the interaction layer. The SEM image on the polished cross-sectional surfaces highlights contrast in atomic number at the interfaces of LBE/oxide as well as surface oxide and the base metal. This is because the signal from the back-scattered electron detector is superimposed on that of secondary electron detector, which results in higher Z materials appearing brighter in the image. For example, solidified LBE residue (of Pb and Bi with atomic numbers of 82 and 83, respectively) appears the brightest, while oxides formed on the surface or as internal precipitates appear the darkest owing to the low Z number of oxygen.

An SEM image of the Fe-1wt%Cr sample after 100-hour test is shown in Figure 4-6 (a). The formation of a porous-appearance oxide film at the interface between LBE and base metal is clearly indicated. To better analyze compositional variations of Fe, Cr and O within the oxide layer, EPMA was employed using a JEOL JXA-733 Superprobe, which is equipped with four wavelength detectors best optimized for high resolution WDS. The location of EPMA measurement is shown in Figure 4-6(a) as a yellow arrow mark, and its resultant profile is presented in Figures 4-6(c) and (d) in wt% and at% basis, respectively. The atomic % concentrations of Fe, Cr, and O are also tabulated in Figure 4-6(b). From the data, it is clear that the interaction layer formed on Fe-1wt%Cr sample is mainly iron oxides having varying degrees of stoichiometry (Fe : O= ~1:1 to 2:3). Incorporation of Cr in the seemingly porous upper layer was negligible, while slight enrichment of Cr up to 2.34 wt% (corresponding to 1.57 at% detected at the 12 μm position in Figure 4-6 (b)) was observed in the lower oxide layer.

As mentioned earlier, the presence of iron oxides originated from the surface oxides formed on a small granules of Pb and Bi at the room temperature. The iron oxide layer appeared as de-stabilized and located in the LBE above original sample surface. Therefore, the kinetic aspects of materials observed during the longer term exposure were not affected considerably by the initial presence of oxygen and the oxygen concentration can be assumed to be kept below the iron oxide formation range after the initial transient period of about 30 hours.

SEM images and X-ray maps of the Fe-1wt%Cr sample after 250-hour test are shown in Figure 4-7. In contrast to the previous 100-hour data, Cr enrichment up to 3.71 wt% was observed in the lower oxide layer when measured by EPMA. This is again confirmed by the strong Cr signal in this layer as shown in X-ray maps provided in Figure 4-7 (b). The thickness

of top iron oxide layer kept constant compared to 100-hr test, indicating that the formation period of oxide for both time span was almost identical. Considering the rapid growth rate of iron oxide above 570°C, this again supports the origin of oxygen from the finite amount of surface oxide from LBE granules. Therefore, the longer term test results were not affected by the presence of iron oxide as it can not sustain the growth after consuming available oxygen in LBE. The spotted strong Pb (LBE) signal inside of the oxides as well as a noticeable Cr distribution in LBE indicates its instability as a solid iron oxides. Figure 4-8 shows a severe penetration of LBE through both iron and Cr-rich oxide layers, which occurred after exposure at 600°C for 500 hours. Based on this, it is clear that the oxides formed on Fe-1wt%Cr alloy are not protective enough to prevent LBE penetration, in spite of observed Cr enrichment of up to 4.22 wt% (2.74 at%) occurred in the lower oxide layer.

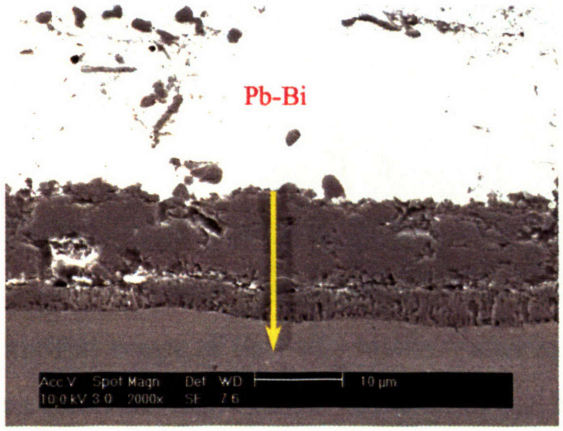

(a)

(b)

Concentration (atomic%)				
Sample	µm	Fe	Cr	O
Fe-1%Cr	0	39.45	0.15	56.89
	1	44.17	0.07	53.78
	2	45.98	0.08	52.36
	3	48.57	0.05	50.85
	4	47.34	0.09	51.26
	5	48.02	0.06	51.55
	6	46.72	0.05	53.21
	7	47.11	0.07	52.60
	8	44.14	0.09	55.13
	9	43.13	0.10	56.17
	10	42.10	0.15	56.91
	11	44.51	0.32	54.62
	12	42.13	1.57	56.27
	13	41.93	1.42	56.55
	14	43.62	1.23	55.00
	15	72.35	1.13	26.32
	16	97.80	0.99	1.00
	17	98.11	0.92	0.73

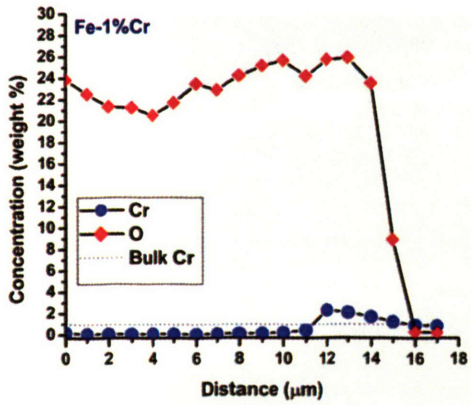

(c)

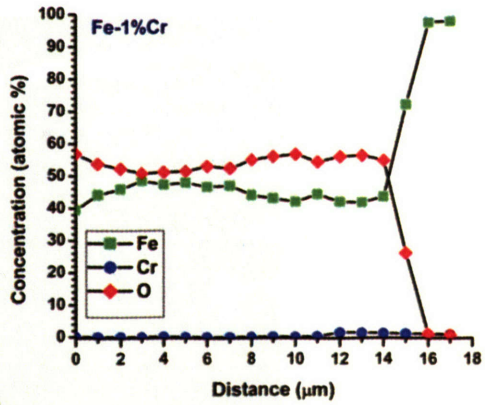

(d)

Figure 4-6 (a) SEM image of Fe-1%Cr material after exposure at 600°C for 100 hours, along with a yellow arrow indicating a scanned line for EPMA, (b) tabulated values of at% profile, (c) concentration profiles of Cr and O in wt%, and (d) concentration profiles of Fe, Cr and O in at%.

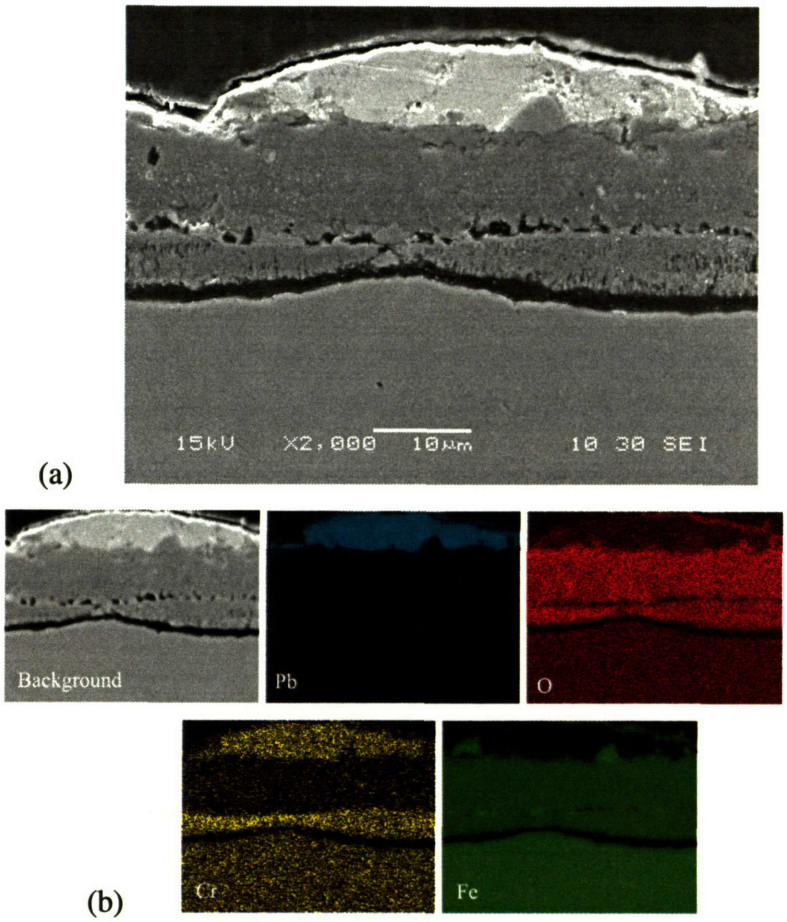

Figure 4-7 (a) SEM image of Fe-1%Cr material after exposure at 600°C for 250 hours, (b) X-ray maps showing elemental distributions of Pb, O, Cr and Fe within the interaction layers.

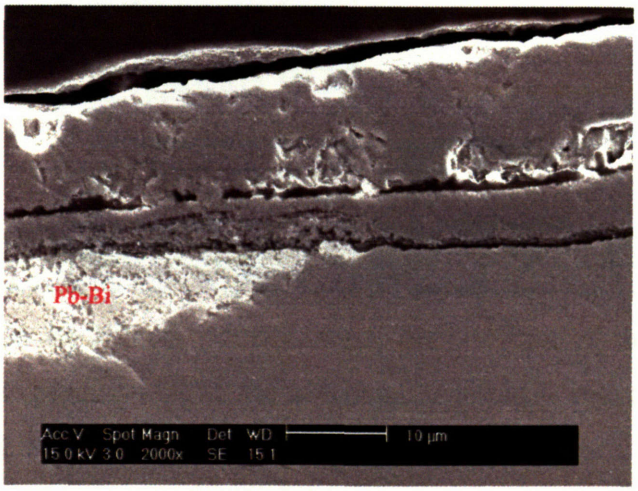

Figure 4-8 SEM image of Fe-1%Cr material showing the LBE penetrated region beneath the oxide layers after exposure at 600°C for 500 hours.

4.3.2 Fe-2.25%Cr

Results of compositional analysis on the oxide for Fe-2.25%Cr material after exposure at 600°C for 500 hours are tabulated in Figure 4-9. The SEM images obtained from 100-, 250-, and 500-hour tests in 600°C are shown in Figure 4-10 Again, the almost constant oxide thickness (upper iron oxide) indicates the limited supply of oxygen during the test duration.

The presence of LBE trapped within the oxide layers yet clearly indicates their instability under the test condition. As with the case of Fe-1%Cr material, EPMA data revealed that the lower portion of the oxide layer has been enriched with Cr up to 8.98 wt% (6.08 at%) during the 500-hour exposure. Again, a deep penetration zone of LBE was detected after a 500-hour test underneath the Cr-rich oxide as shown in Figure 4-10 (c).

(a)

Concentration (atomic%)				
Sample	μm	Fe	Cr	O
Fe-2.25%Cr	0	44.22	0.02	55.69
	1	48.94	0.01	51.00
	2	43.63	0.00	56.33
	3	48.69	0.02	51.22
	4	45.58	0.01	54.30
	5	41.47	0.02	56.96
	6	43.50	0.03	55.25
	7	45.32	0.02	53.79
	8	44.59	0.02	54.44
	9	43.53	0.01	56.28
	10	45.54	0.02	53.77
	11	46.86	0.02	52.98
	12	46.98	0.01	52.86
	13	46.66	0.01	52.51
	14	47.17	0.01	52.69
	15	48.44	0.02	51.37

(b)

Concentration (atomic%)				
Sample	μm	Fe	Cr	O
Fe-2.25%Cr	0	28.91	5.00	58.77
	1	30.96	5.17	62.51
	2	36.05	4.63	59.30
	3	35.38	6.08	58.51
	4	72.05	3.72	22.83

Figure 4-9 EPMA results on compositional analysis (in at%) within the oxide formed on Fe-2.25%Cr material after exposure at 600°C for 500 hours. Atomic % concentrations of Fe, Cr, and O in (a) upper iron oxide and (b) lower Cr-rich oxide.

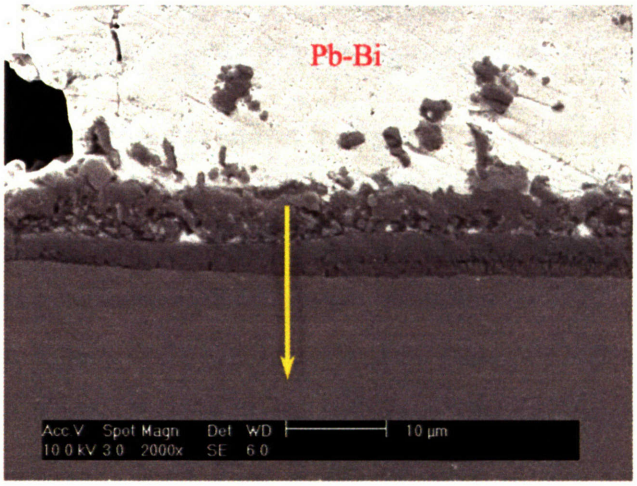

(a)

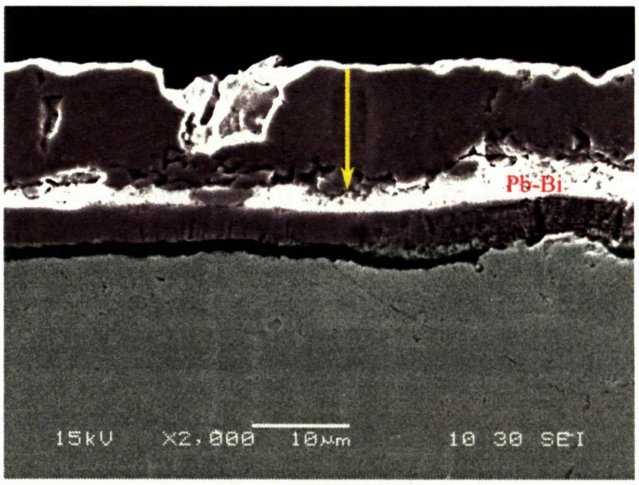

(b)

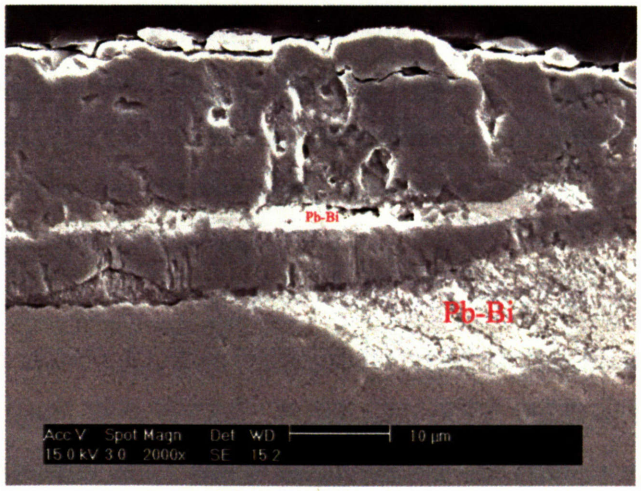

(c)

Figure 4-10 SEM images of Fe-2.25%Cr material after exposure at 600°C for (a) 100 hours (b) 250 hours and (c) 500 hours.

4.3.3 Fe-9%Cr

SEM images of Fe-9%Cr material are shown in Figure 4-11 obtained from 600°C exposure ranging in duration from 100- to 500 hours. Again, LBE penetration occurred after 500 hours. However, some distinctive features are worth mentioning for oxide layers detected during intermediate exposure times associated with Cr content in alloy.

From EPMA data listed in Figure 4-12, oxides formed at 100-hour test again shows a duplex structure consisting of iron oxide (observed from 0 to 6μm distance range) and Cr-rich oxide. The Cr-rich oxide layer (ranging from 6 to 9 μm distance in the graph) has an average composition being close to that of a Fe_3O_4 + $FeCr_2O_4$ mixture and shows enrichment of Cr up to 16.2 wt% (10.95 at%). The morphological difference between the interaction layer formed on a Fe-9%Cr material, distinguishing itself from the lower-Cr alloy case, is the formation of an internal oxidation zone beneath the Cr-rich oxide layer. As seen in Figure 4-12 (a) and (b), this zone, corresponding to a scanning distance of 10 to 15 μm, maintains a constant concentration level of 20 at % oxygen (~7 wt%) , along with 9 at% Cr (~10 wt%) and remaining 70 at% Fe. With the compositional evidence, it can be assumed that the internal oxidation precipitates have a stoichiometry close to that of $FeCr_2O_4$. This multi-layer structure of oxides formed on Fe-Cr alloys are reported by many researchers [4-5].

In addition to the presence of an internal oxidation zone, the following features were observed in a longer duration test (300-hour) as shown in Figure 4-13 (a) and (b), including: (a) a loss of outermost iron oxide layer (which is consistent with the previous low-Cr alloy results), (b) a maximum Cr enrichment of up to 21.03 wt% (14.87 at%) in Cr-rich (spinel) layer, and (c) an increased depth in the internal oxidation zone.

Figure 4-14 (b) shows another important feature to be noted for this material. After 250-hour exposure, elemental X-ray maps show a strong distribution of Cr and O at the grain boundaries located near the internal oxidation zone, and is an indication that grain boundary oxidation has occurred. Based on the significantly reduced Fe signal at grain boundaries, it can be assumed that Cr-rich spinel of Cr_2O_3 precipitates may have been formed preferentially along the grain boundaries.

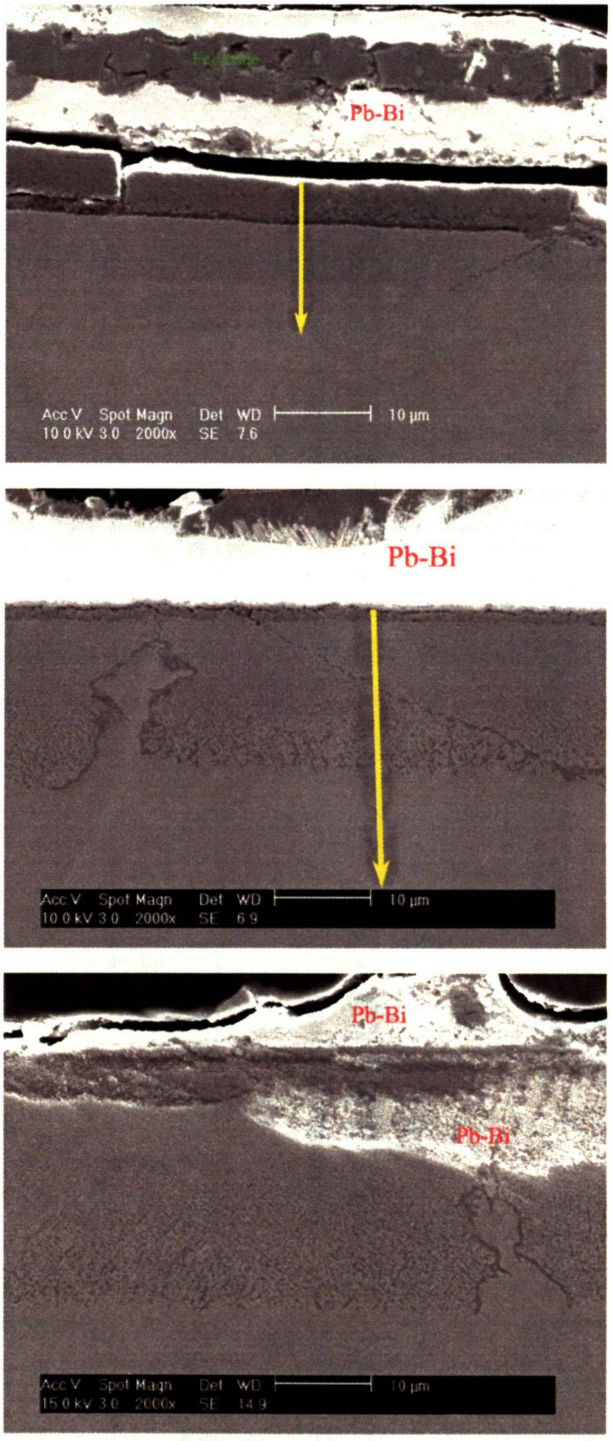

Figure 4-11 SEM images of Fe-9%Cr material, after exposure at 600°C for (a) 100 hours, (b) 300 hours, and (c) 500 hours.

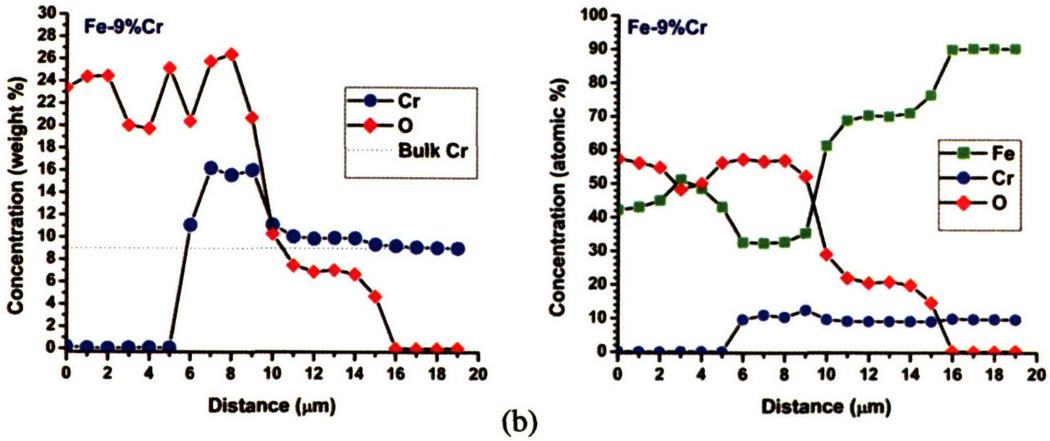

Figure 4-12 Compositional analysis data of Cr, O and/or Fe obtained by EPMA for Fe-9%Cr material after exposure at 600°C for 100 hours, presented in (a) wt% and (b) at%.

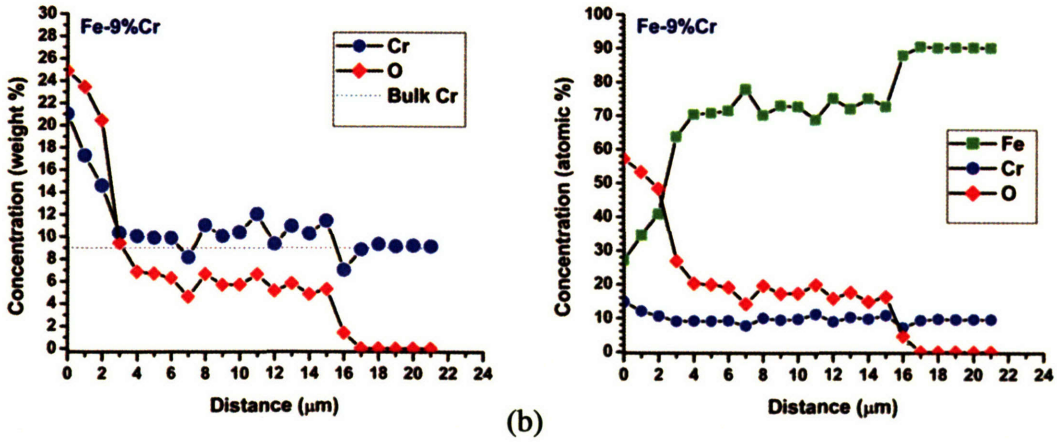

Figure 4-13 Compositional analysis data of Cr, O and/or Fe obtained by EPMA for Fe-9%Cr material after exposure at 600°C for 300 hours, presented in (a) wt% and (b) at%.

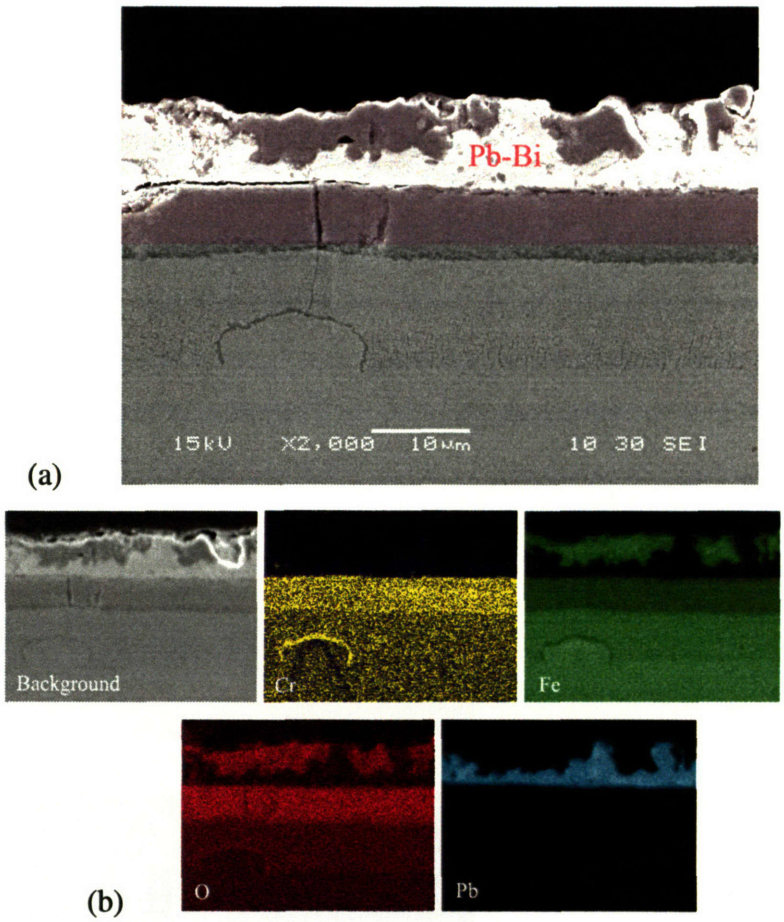

Figure 4-14 (a) SEM image of Fe-9%Cr material after exposure at 600°C for 250 hours, (b) X-ray maps showing elemental distributions of Cr, Fe, O, and Pb within the interaction layers.

4.3.4 Fe-12%Cr

As illustrated in Figure 4-15, the interaction layers developed in Fe-12%Cr material during 100-hour exposure at 600°C LBE also have three distinctive layers, which are iron oxide, Cr-rich oxide being close to the spinel oxide stoichiometry, and the internal oxidation zone. Maximum Cr enrichment in Fe-Cr spinel layer was observed as 18.76 wt% (12.64 at%), occurring at 9 μm depth from the top surface of the porous iron oxide layer.

As shown in Figure 4-16, Fe-12%Cr sample tested for 250 hours again exhibited Cr and O segregation in the grain boundary, showing stronger signals of Cr and O along the grain

boundaries being contrasted to the background when analyzed with EDX. In addition, it is clearly observed that once vertically grown, the network of internal oxide precipitates (shown as tiny, dark granular figures in the internal oxidation zone as can be seen in Figures 4-15 (a) and 4-16 (a)), begins to become connected laterally (as seen in Figure 4-17 (a)), and eventually forms a complete lateral connection, which divides the interface between the internal oxidation zone and the base alloy with a clear, dark line (Figure 4-17(b)). With EPMA result tabulated in Figure 4-16 (d), the oxide particles participating in the growing network are Cr-rich spinel, based on the collected data of Fe, Cr and O concentrations showing proximity to Fe+$FeCr_2O_4$ stoichiometry (background Fe + 15.70 at% Cr and 30.82 at% O) at 11 μm distance, corresponding to spot close to the grain boundary.

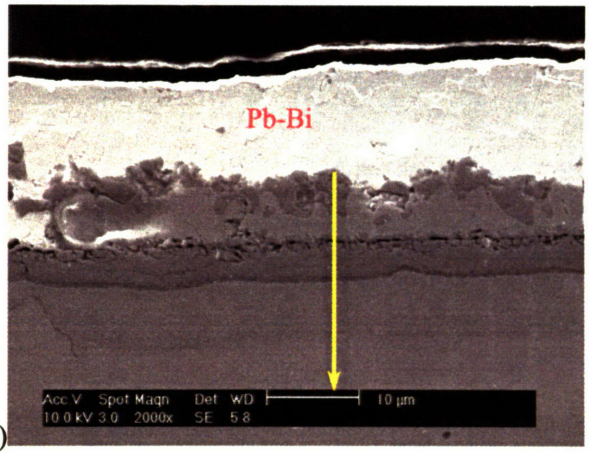

(a)

Concentration (atomic%)				
Sample	µm	Fe	Cr	O
Fe-12% Cr	0	43.62	0.29	55.54
	1	43.15	0.31	55.95
	2	43.14	0.37	55.56
	3	51.50	0.49	46.88
	4	51.80	0.54	47.07
	5	45.93	9.42	44.16
	6	35.74	8.38	55.79
	7	32.17	11.44	56.39
	8	31.61	11.83	56.56
	9	31.07	12.64	56.30
	10	44.48	12.24	43.27
	11	57.88	11.73	30.33
	12	60.71	11.80	27.42
	13	61.83	11.80	26.26
	14	63.35	11.87	24.67
	15	66.31	12.00	21.60
	16	85.05	12.60	2.18
	17	86.65	12.93	0.23
	18	86.82	13.00	0.01
	19	86.77	12.83	0.21
	20	86.71	12.96	0.12
	21	86.65	12.86	0.31

(b)

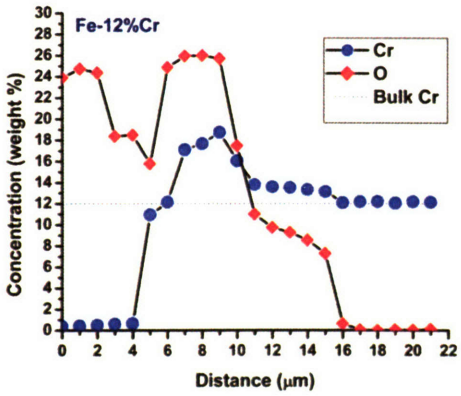

(c)

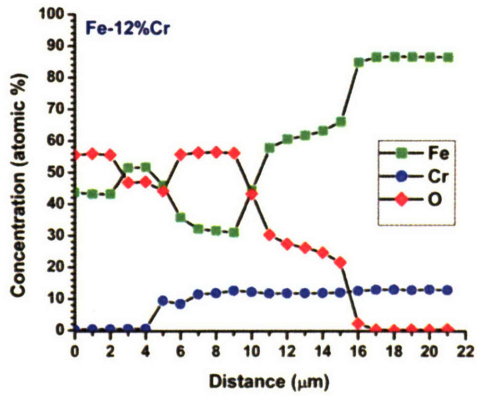

(d)

Figure 4-15 (a) SEM image of Fe-12%Cr material after exposure at 600°C for 100 hours with a yellow arrow indicating a line scan for EPMA, (b) tabulated values of at% profile, (c) concentration profiles of Cr and O in wt%, and (d) concentration profiles of Fe, Cr and O in at%.

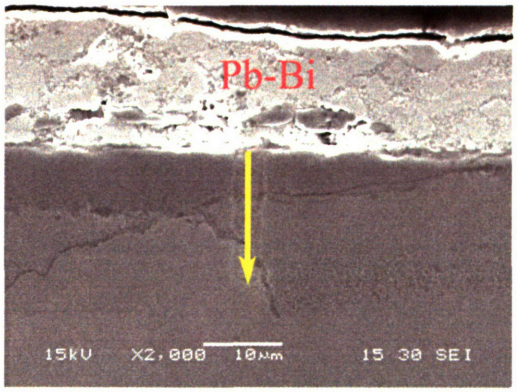

(a)

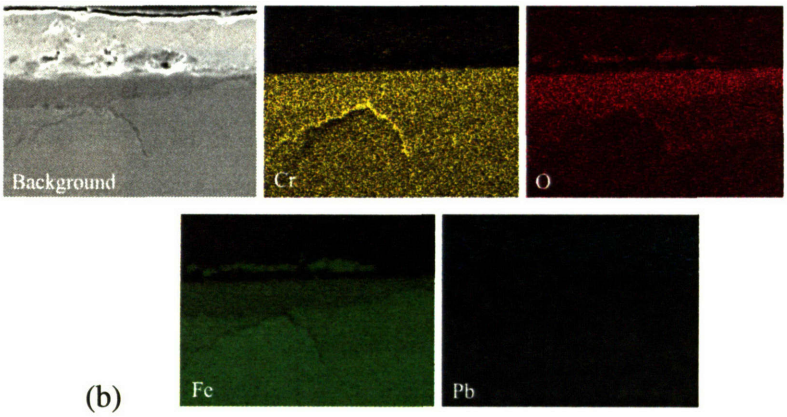

(b)

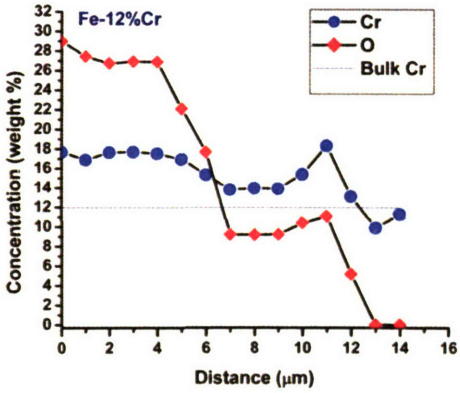

(c)

(d)

Sample	μm	Concentration (atomic%) Fe	Cr	O
Fe-12% Cr	0	28.19	11.32	60.28
	1	30.77	11.02	58.20
	2	30.84	11.69	57.48
	3	30.66	11.66	57.59
	4	30.68	11.57	57.64
	5	37.32	11.95	50.64
	6	44.82	11.63	43.52
	7	60.88	12.35	26.73
	8	60.65	12.52	26.79
	9	60.96	12.36	26.64
	10	57.15	13.39	29.40
	11	53.24	15.70	30.82
	12	71.10	12.59	16.17
	13	89.08	10.83	0.00
	14	87.65	12.29	0.00

Figure 4-16 (a) SEM image of Fe-12%Cr material after exposure at 600°C for 250 hours, along with a yellow arrow indicating a line scan for EPMA, (b) X-ray maps showing elemental distributions of Cr, Fe, O, and Pb within the interaction layers (c) concentration profiles of Cr and O in wt%, and (d) tabulated values of concentration profiles of Fe, Cr and O in at%.

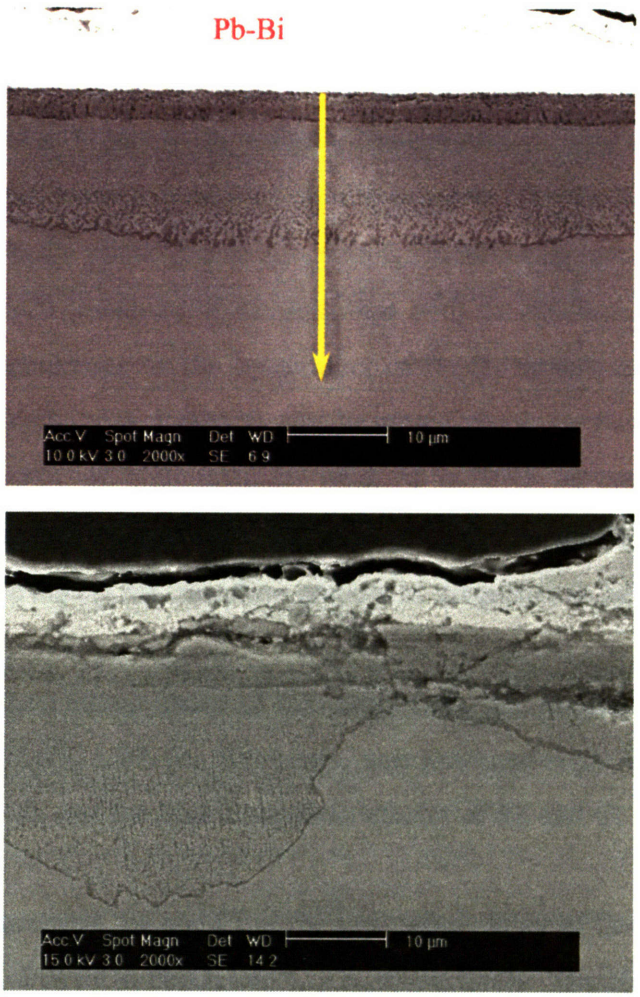

(a)

(b)

Figure 4-17 SEM images of Fe-12%Cr material obtained after exposure at 600°C for (a) 300 hours and (b) 500 hours.

To further investigate the present oxide phases in , XRD spectral data were obtained for the 500-hour tested sample at 600°C. In the upper graph shown in Figure 4-18, various oxide peaks (marked as ***O***) can be seen, along with the Pb-Bi related phases (marked as *). The lower graph provides XRD spectra of the base material, which has not been tested in LBE but stored in desiccators after 3µm surface finish. It is clear that the base material contains only BCC phases whose peaks are indicated by Miller indices. To identify relevant phase peaks, obtained data were analyzed with Jade 7.0 software (from MDI, Inc.) using the ICDD (International Center for Diffraction Data) PDF databases.

After a detailed peak search and match process, the major phase present in the tested sample was identified as iron-chrome oxide ($FeCr_2O_4$) of spinel structure as a dominant phase. The detailed results are presented in Figure 4-19. γ- Fe_2O_3 (maghemite) as well as FeO (wüstite) and α-Fe_2O_3 (hematite) phase peaks are also present. As discussed in Chapter 2, this result supports the transition process for Fe_3O_4 phase that is assumed to occur at temperatures above 570°C. Also, the presence of γ- Fe_2O_3 (maghemite) is consistent with the findings of Nasrazadani and Raman[2], explaining its occurrence as the by-product of Fe_3O_4 transformation into hematite. The high intensity of $FeCr_2O_4$ peak intensity can be noted resulting from the increased Cr content in alloy. The presence of high intensity peak of α-Fe_2O_3 as comparable to that of $FeCr_2O_4$ is worth mentioning associated with the effect of increase in Cr, which is known to stabilize Fe^{3+} based structure during the transition process of magnetite to hematite (α-Fe_2O_3) [3].

To further understand the binding states of the oxide film, the surface oxide of Fe-12%Cr material, after exposure at 600°C LBE for 500 hours, was analyzed with XPS. As a result, the spectra, shown in Figure 4-20, and the high resolution spectra of Fe and Cr as seen in Figure 4-21 were obtained.

Combined with XRD measurement, Fe and Cr at the top surface layer of Fe-Cr oxide are known to be in the chemical states of close to Fe_2O_3 and Cr_2O_3, respectively. Therefore, the morphology of multi-layers of iron-chromium oxides can be structured as to have F_2O_3-Cr_2O_3 layer on the top, γ-Fe_2O_3 layer below, followed by Fe_3O_4 layer with $FeCr_2O_4$ as the dominant phase, and with FeO being innermost layer [4-5]

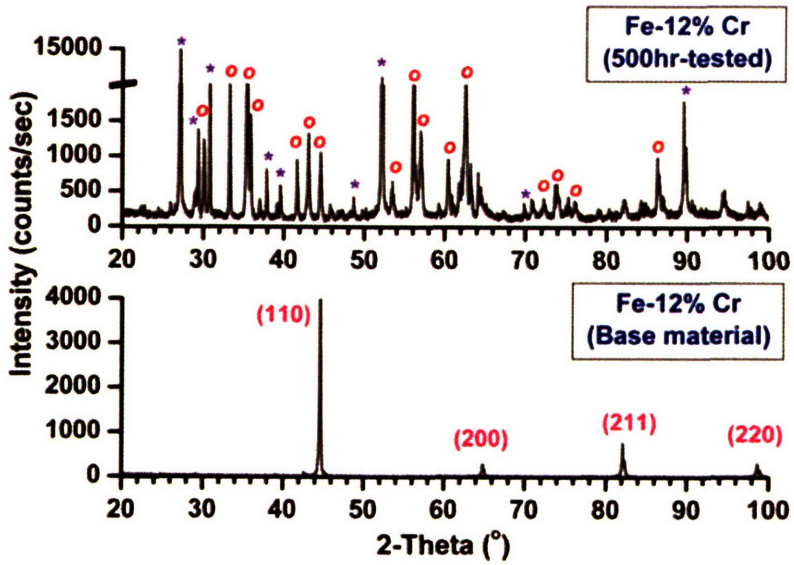

Figure 4-18 XRD spectra of Fe-12%Cr material showing the existing phase peak after 500-hour, 600°C LBE exposure (upper graph, O: oxide peaks, *: Pb-Bi peaks) in comparison to that of the base material (lower graph, BCC phase, Miller indices)

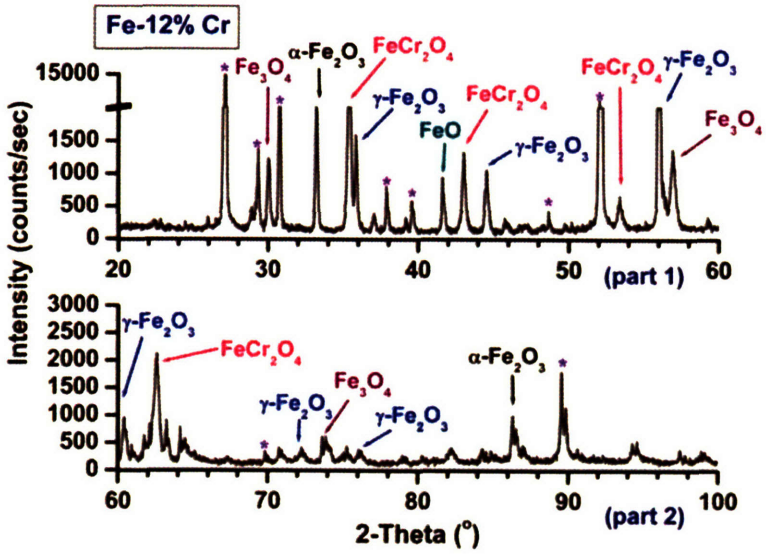

Figure 4-19 XRD spectra of Fe-12%Cr material after exposure at 600°C for 500 hours showing a detailed oxides peak identification.

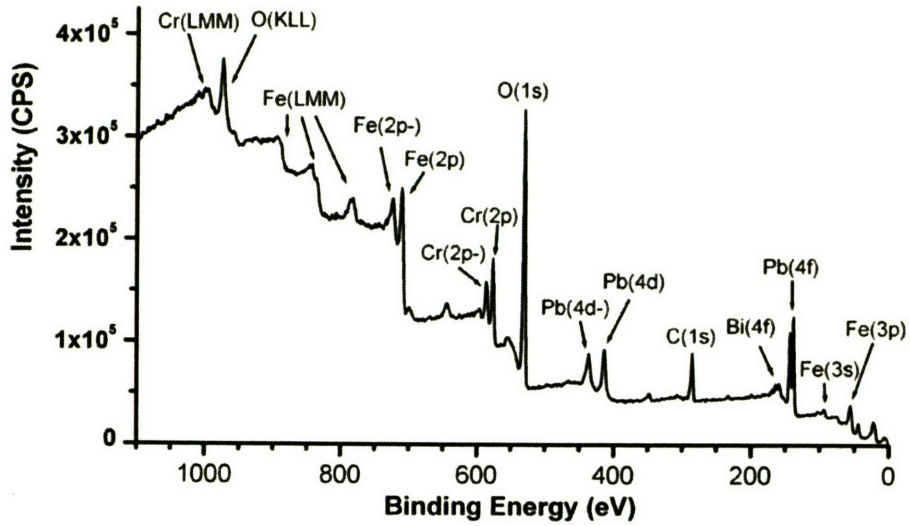

Figure 4-20 XPS survey spectra for Fe-12%Cr material after exposure at 600°C for 500 hours. Spin-orbit splitting of Cr is represented by Cr(2p-) for Cr($2p_{1/2}$), and Cr(2p) for Cr($2p_{3/2}$). Fe and Pb are presented with the same labeling convention as Cr.

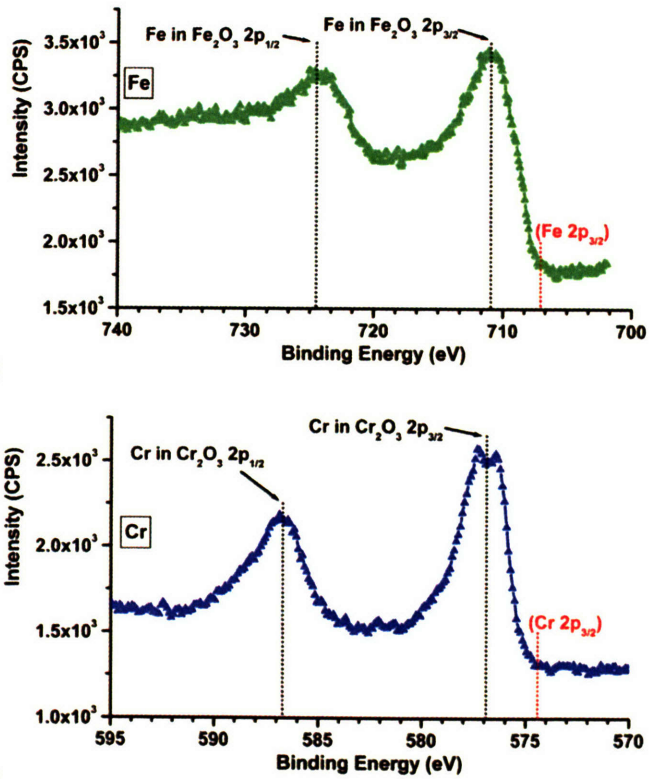

Figure 4-21 XPS high-resolution spectra of (a) Fe and (b) Cr obtained from Fe-12%Cr material tested in 600°C LBE for 500 hours, presented with a charge correction to adventitious hydrocarbon at 285.0eV.

4.3.5 Fe-18%Cr

After exposure of Fe-18%Cr material to LBE at 600°C for 300 hours, a completely different type of oxide layer was detected on the sample surface, having a very compact and adherent appearance. EPMA data approximated the composition of oxide as $(Fe,Cr)_2O_3$ and no internal oxidation zone was detected underneath this layer. The SEM image of Figure 4-22 shows the oxide layer morphology and Figure 4-23 lists the detailed result of EPMA compositional analysis within the layer.

As shown in Figure 4-23 (b) and (d), a fairly uniform composition of oxide has formed during 500 hours in 600°C LBE test, and the highest enrichment of Cr was observed at the interface between the oxide and the base metal. Again, the oxide composition matched closely that of $(Fe,Cr)_2O_3$, a continuous solid solution of Fe_2O_3 and Cr_2O_3, both having the corundum structure. As mentioned earlier, such changes in the oxide composition and phase can be attributed to the stabilizing effect of Cr^{3+} on Fe^{3+} ion in the oxide lattice [3], thereby promoting α-Fe_2O_3 (hematite) structure where a complete solid solution with Cr_2O_3 can occur, while accommodating the increased Cr content in the alloy. This finding is also consistent with the observed disappearance of the internal oxidation zone, proving that the solubility of Cr_2O_3 in the surface oxide has increased significantly.

Figure 4-24 shows the result of EDX analysis revealing the elemental distribution within the oxide layer. Slight variations of Cr concentration within the oxide can be observed qualitatively, along with enrichment of Cr and O at the oxide/base alloy interface.

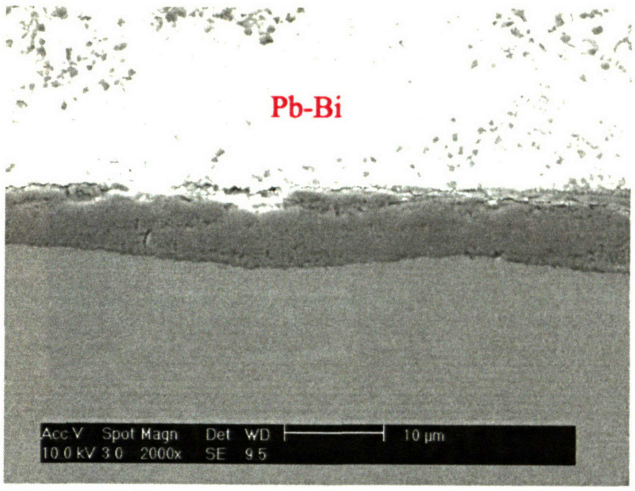

Figure 4-22 SEM image of Fe-18%Cr after exposure at 600°C for 300 hours.

(a)

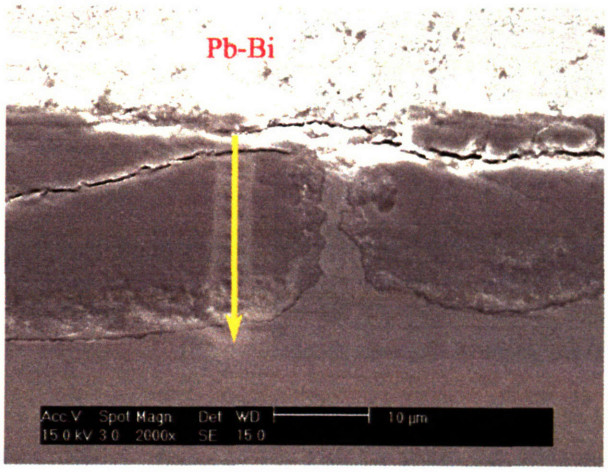

(b)

Concentration (atomic%)				
Sample	µm	Fe	Cr	O
Fe-18% Cr	0	27.77	16.42	55.26
	1	27.14	16.64	55.79
	2	23.80	14.70	61.46
	3	26.24	15.46	58.00
	4	24.55	15.44	59.99
	5	24.90	15.65	59.39
	6	24.50	15.88	59.60
	7	24.72	16.36	58.92
	8	24.37	16.61	59.01
	9	24.13	16.56	59.31
	10	23.96	17.26	58.79
	11	23.19	18.22	58.54
	12	22.96	18.41	58.58
	13	23.29	17.87	58.77
	14	23.55	18.41	57.84
	15	21.93	19.48	58.20
	16	21.81	20.60	57.01
	17	22.01	21.22	55.93
	18	20.85	21.07	57.56
	19	23.54	20.47	55.50
	20	54.02	18.53	27.38
	21	70.23	16.51	13.20

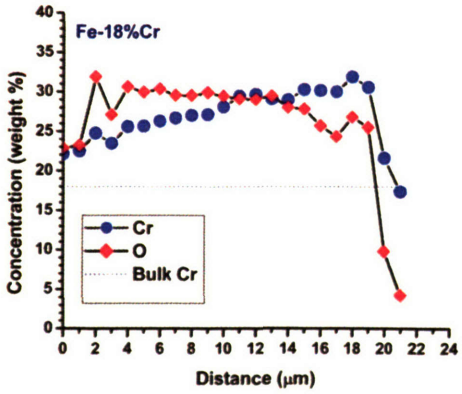

(c)

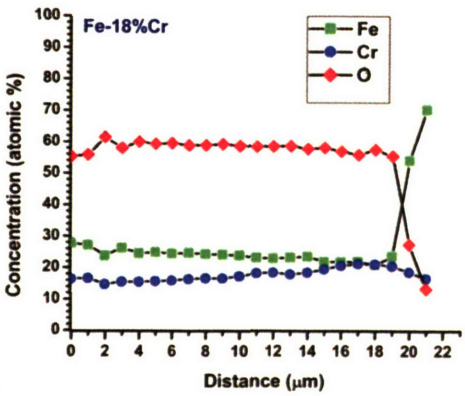

(d)

Figure 4-23. (a) SEM image of Fe-18%Cr after exposure at 600°C for 500 hours, with a yellow arrow indicating a scanned line EPMA, (b) tabulated values of at% profile, (c) concentration profiles of Cr and O in wt%, and (d) concentration profiles of Fe, Cr and O in at%.

(a)

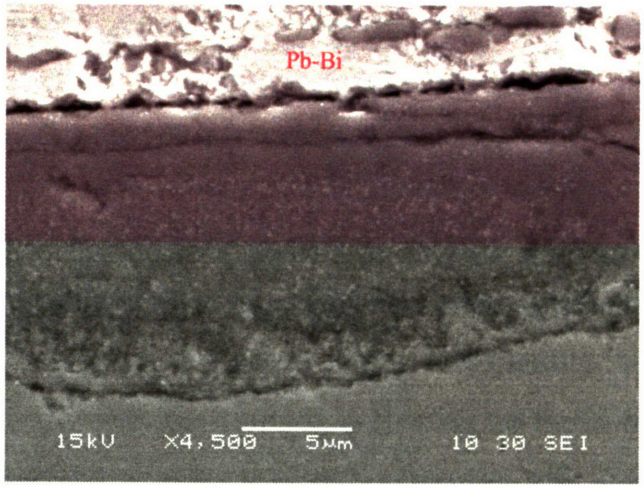

(b)

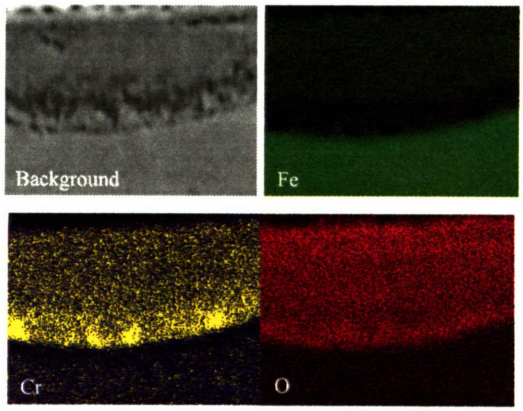

Figure 4-24 (a) SEM image of Fe-18%Cr material after exposure at 600°C for 250 hours, (b) X-ray maps showing elemental distributions of Cr, Fe, and O within the oxide layer.

4.3.6. Summary of Fe-Cr Test Results

- Due to the residual oxygen formed as surface oxides in Pb and Bi granules, the formation of iron based oxide were observed at the initial stages of exposure in Fe-Cr materials containing low Cr content, namely Fe-1wt% Cr and Fe-2.25wt% Cr. Duplex structure of outer iron oxide and inner Cr-rich oxide was observed. The estimated duration for such oxidation was only the first 30 or so hours, which can be verified by the porous, unstable nature of iron oxides and the constant thickness throughout the

increased tested duration. Therefore, the interaction kinetics of tested materials is not affected for longer term tests. A deep penetration of LBE was observed for both Fe-1%Cr and Fe-2.25%Cr after 500 hour exposure.

- Fe-Cr alloys with 9- and 12% Cr showed an internal oxidation region beneath an external Cr-rich spinel layer. The major phase in oxide is detected as $FeCr_2O_4$ from XRD analysis on Fe-12%Cr. Other phases such as FeO (wüstite), γ-Fe_2O_3 (maghemite), and α-Fe_2O_3 (hematite) were also detected, supporting the Fe_3O_4 transformation above 570°C. This multi-layered structure is in good agreement with findings reported in the literature [4-5]. Also, EPMA analysis in the internal oxidation zone gave compositional result in close match with Fe_3O_4+$FeCr_2O_4$. Oxide precipitates in the zone were believed to be a Cr-rich spinel. Oxidation product of Cr and O formed along the grain boundary.

- Fe-18%Cr showed change in oxide composition to $(Fe,Cr)_2O_3$, which is a solid solution between Fe_2O_3 and Cr_2O_3. Disappearance of the internal oxidation zone was observed with the morphology of oxide appearing compact and slowly growing. Enrichment of Cr and O at the interface between the oxide and the base metal is highlighted.

4.4 Corrosion Behavior of Fe-Si Alloys

Fe-Si alloys of Fe-1.25%Si, Fe-2.55%Si, and Fe-3.82%Si were tested in static LBE at 600°C for up to 300 hours. Most of the samples show similar trends in their oxide characteristics with respect to the test duration. In order to avoid repeated explanations on such features, the experimental results on Fe-Si alloys are presented congruently in this section.

4.4.1. Fe-2.55%Si and Fe-3.82%Si After 100-hour Test

SEM images and EPMA data on concentrations of Si, O and/or Fe are shown in Figure 4-25 for Fe-2.55%Si sample and in Figure 4-26 for Fe-3.82%Si sample after 100-hour exposure to 600°C static LBE. Experimental data on 100-hour test are not available because a complete loss

of interaction layer occurred during the sample preparation stage. A dual structure in the interaction layer, consisting of the outer iron oxide and the internal oxidation zone, were observed in both materials.

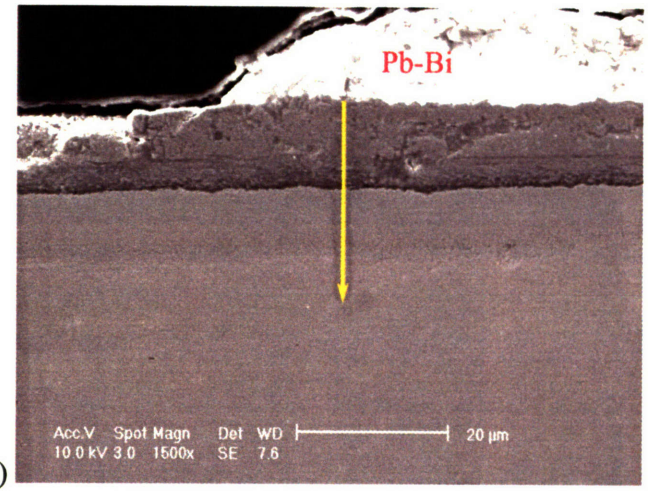

(a)

(b)

Sample	µm	Fe	Si	O
		Concentration (atomic%)		
Fe-2.55%Si	0	44.86	0.06	53.93
	1	47.88	0.06	51.45
	2	47.11	0.01	52.69
	3	48.52	0.10	51.36
	4	45.56	4.30	49.97
	5	40.04	5.54	54.30
	6	39.35	7.04	53.53
	7	41.18	8.46	50.27
	8	75.37	5.21	19.29
	9	81.28	4.66	13.91
	10	81.60	5.07	13.19
	11	84.49	5.13	10.22
	12	85.86	4.83	9.11
	13	85.22	5.10	9.58
	14	84.33	5.38	10.18
	15	88.21	4.78	6.92
	16	94.54	5.30	0.00
	17	94.42	5.40	0.00
	18	94.51	5.32	0.00
	19	94.55	5.27	0.00
	20	94.75	4.98	0.11
	21	94.65	5.19	0.00

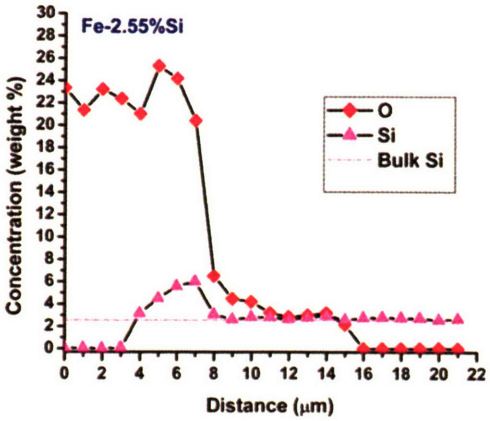

(c)

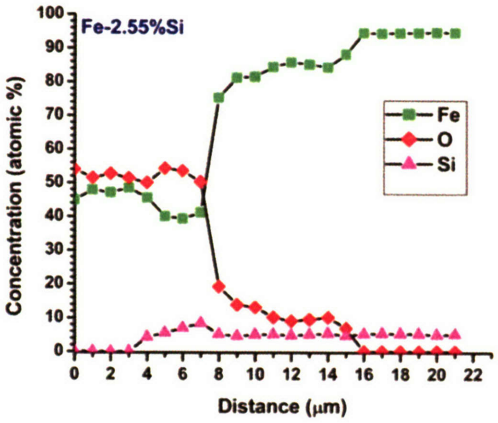

(d)

Figure 4-25 (a) SEM image of Fe-2.55%Si after exposure at 600°C for 100 hours, along with a yellow arrow indicating a line scan for EPMA, (b) tabulated values of at% profile, (c) concentration profiles of Si and O in wt%, and (d) concentration profiles of Fe, Si and O in at%.

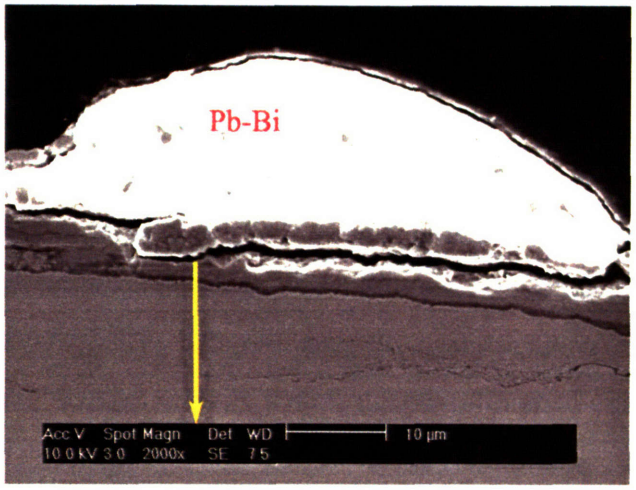

(a)

Sample	µm	Concentration (atomic%) Fe	Si	O
Fe-3.82%Si	0	40.74	0.14	57.39
	1	41.43	0.93	56.58
	2	38.97	1.54	58.08
	3	45.97	2.06	51.50
	4	38.00	9.20	52.67
	5	65.81	7.90	26.14
	6	69.97	7.92	21.95
	7	71.75	8.06	20.02
	8	72.80	7.97	19.05
	9	76.33	7.41	16.09
	10	77.88	7.19	14.76
	11	79.55	6.84	13.45
	12	78.87	7.17	13.75
	13	75.83	8.37	15.45
	14	69.31	10.78	19.75
	15	76.40	9.21	14.28
	16	89.11	8.07	2.64
	17	90.58	8.301	0
	18	91.48	8.326	0
	19	91.34	8.456	0

(b)

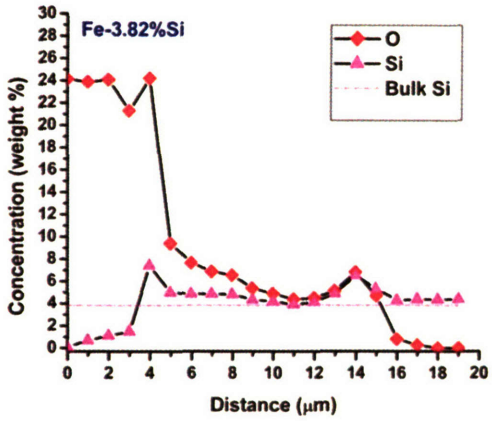

(c)

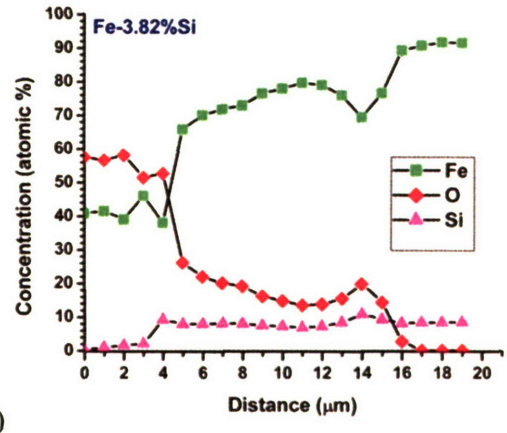

(d)

Figure 4-26 (a) SEM image of Fe-3.82%Si after exposure at 600°C for 100 hours, along with a yellow arrow indicating a scanned line for EPMA, (b) tabulated values of at% profile, (c) concentration profiles of Si and O in wt%, and (d) concentration profiles of Fe, Si and O in at%.

As shown in Figures 4-25 and 4-26, EPMA data of both samples detected enrichment in Si concentration at the front of internal oxidation zone (for Fe-2.55%Si: 7µm, for Fe-3.82%Si: 4µm). For the Fe-3.82%Si material, a similar concentration peak of Si was detected at the end of the zone located at 14µm. The oxygen concentration at the first Si peak location is too high for any Si based oxides formation. However, the composition in the subsequent internal oxidation zone can be interpreted as a mixture of Fe with Fe_2SiO_4 and/or SiO_2 oxide particles.

4.4.2. Fe-1.25%Si, Fe-2.55%Si and Fe-3.82%Si After 300-hour Test

Further progress in the internal oxidation zone formation was observed from the SEM images of Fe-Si alloys tested 300 hours in 600°C LBE. In Fe-1.25% sample, an averaged depth of 10.4 (±0.6) μm internal oxidation zone was detected. In addition, the presence of grain boundary oxidation is indicated by the dark line residing at the lower right corner of the SEM image of Figure 4-27 (a). The affected grain boundary is about 35.7 μm in depth from the surface to the base metal, which contrasts with the depth of internal oxidation zone as stated above.

(a)

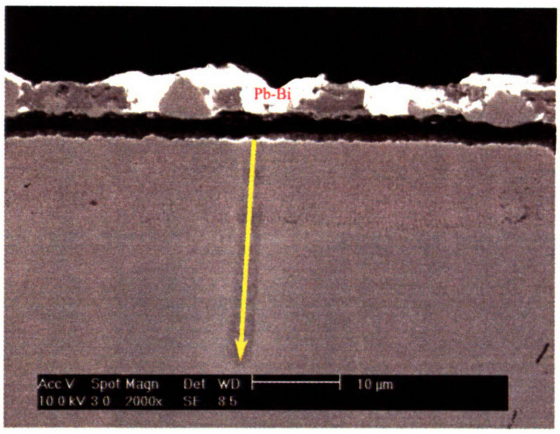

(b)

Sample	μm	Concentration (atomic%) Fe	Si	O
Fe-1.25%Si	0	66.29	2.82	30.25
	1	60.57	2.66	35.91
	2	78.05	3.15	18.58
	3	87.69	2.41	9.67
	4	87.46	2.36	9.98
	5	88.24	2.27	9.28
	6	88.23	2.29	9.19
	7	89.52	2.33	8.01
	8	90.68	2.29	6.88
	9	90.44	2.54	6.93
	10	91.89	2.02	5.89
	11	92.61	2.13	5.21
	12	92.27	2.07	5.65
	13	97.50	1.49	0.84

(c)

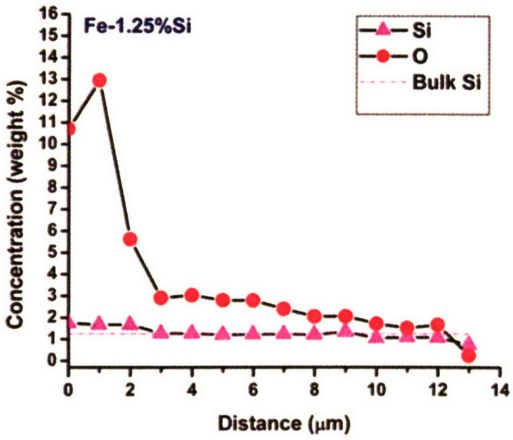

(d)

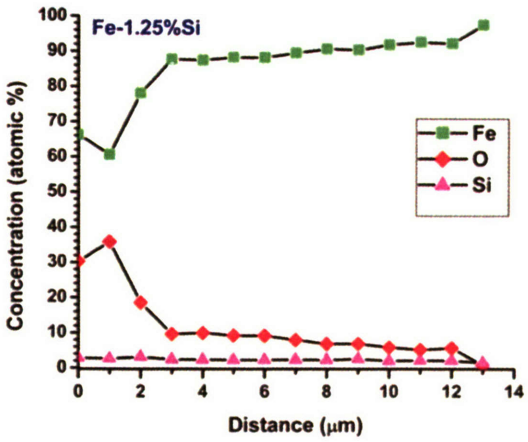

Figure 4-27 (a) SEM image of Fe-1.25%Si after exposure at 600°C for 300 hours with a yellow arrow indicating a line scan for EPMA, (b) tabulated values of at% profile, (c) concentration profiles of Si and O in wt%, and (d) concentration profiles of Fe, Si and O in at%.

An increase in Si content in Fe-Si alloys promotes, a more distinctive, band-like structure of internal oxidation zone near the surface as can be seen in Figure 4-28(a) and Figure 4-29(a). Although the Si contents in the bulk is close to (for Fe-2.55%Si material), or exceeds (for Fe-3.82%Si material) the minimum value of Si (5 at%) known to form a continuous external SiO_2 scale [6], no presence of such layer having an exclusive SiO_2 composition was detected from EPMA data on both samples. However, from the composition profile of Fe-2.55%Si displayed in Figure 4-28 (b)-(c), the presence of Fe_2SiO_4 precipitates along with SiO_2 particles may be assumed. For Fe-3.82%Si material as shown in Figure 4-29, a discontinuous scale of SiO_2 precipitates is rather suspected, based on the Si:O ratio close to 1:2 in the oxidation zone. This could be attributed to the very slow kinetics of SiO_2 formation reported in the literature [7]. Nevertheless, the formation of Fe_2SiO_4 or SiO_2 precipitates are known to increase oxidation resistance by blocking the paths for iron to diffuse to form external oxide.

(a)

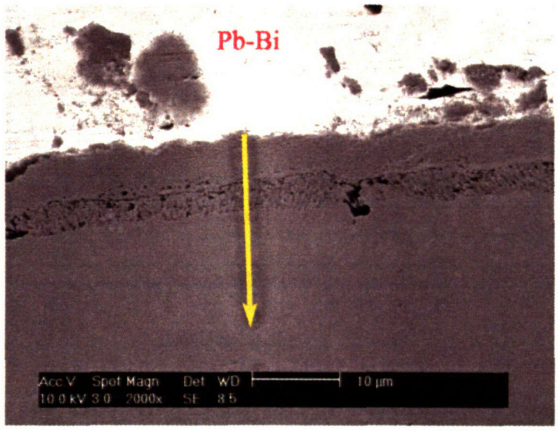

(b)

Sample	µm	Concentration (atomic%) Fe	Si	O
Fe-2.55%Si	0	79.77	4.37	15.74
	1	72.09	4.60	22.84
	2	71.84	4.45	23.00
	3	74.36	4.65	20.86
	4	82.50	4.16	13.27
	5	79.97	4.23	15.74
	6	80.46	4.31	15.17
	7	80.94	4.50	14.45
	8	83.43	5.32	11.05
	9	77.11	7.22	15.55
	10	76.97	7.48	15.44
	11	76.95	7.49	15.46
	12	90.81	3.74	5.38
	13	88.64	4.07	7.22
	14	96.74	3.17	0.00
	15	95.99	3.91	0.00
	16	95.32	4.56	0.00

(c)

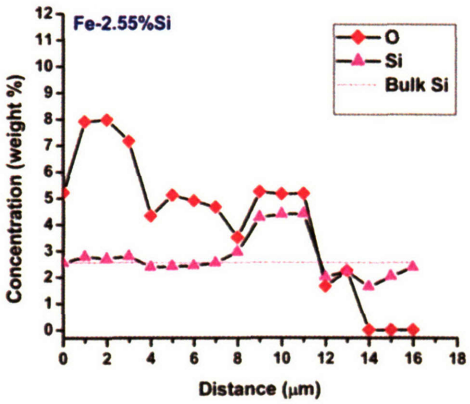

(d)

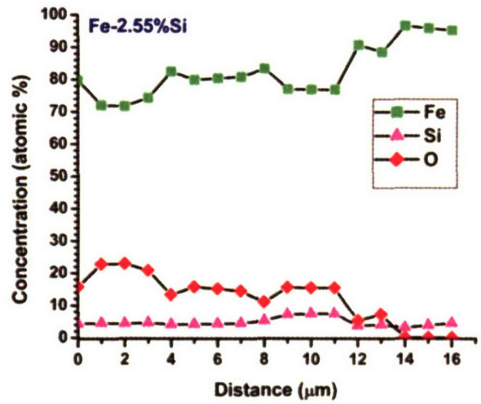

Figure 4-28 (a) SEM image of Fe-2.55%Si after exposure at 600°C for 300 hours, along with a yellow arrow indicating a line scan location for EPMA, (b) tabulated values of at% profile, (c) concentration profiles of Si and O in wt%, and (d) concentration profiles of Fe, Si and O in at%.

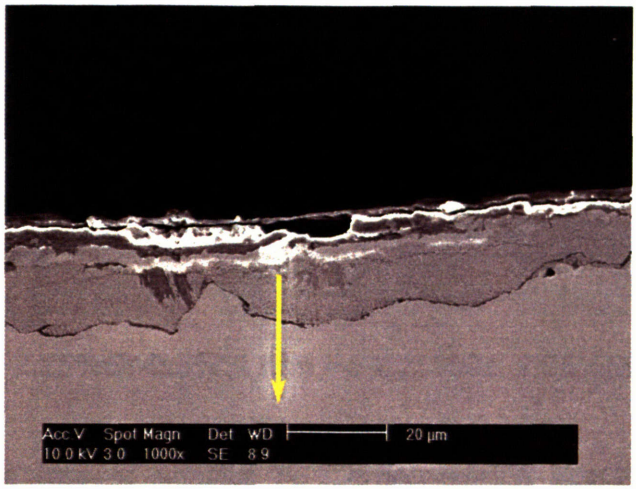

(a)

Sample	µm	Concentration (atomic%) Fe	Si	O
Fe-3.82%Si	0	38.70	11.71	47.04
	1	65.94	8.31	24.92
	2	70.13	8.68	20.94
	3	69.79	9.38	20.64
	4	67.65	9.88	22.27
	5	75.67	12.11	12.06
	6	93.99	5.85	0.08
	7	93.60	6.28	0.00
	8	93.34	6.56	0.00
	9	93.00	6.87	0.00
	10	92.78	7.09	0.00
	11	92.79	7.10	0.00
	12	92.70	7.15	0.00
	13	92.65	7.23	0.00
	14	92.33	7.54	0.00
	15	92.30	7.58	0.00
	16	92.86	7.08	0.00
	17	92.61	7.27	0.00
	18	92.31	7.54	0.00
	19	92.39	7.51	0.00
	20	92.30	7.58	0.00

(b)

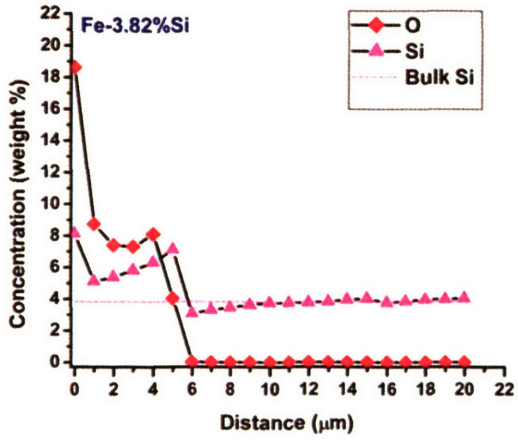

(c)

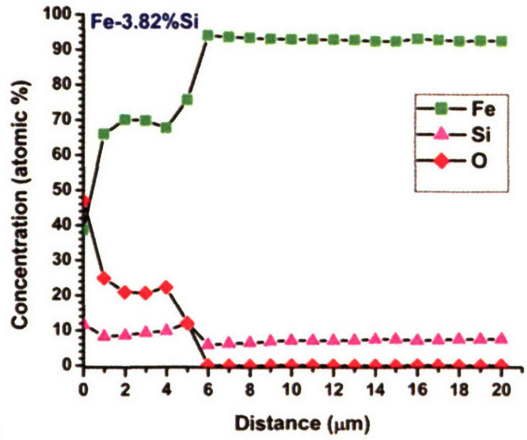

(d)

Figure 4-29 (a) SEM image of Fe-3.82%Si after exposure at 600°C for 300 hours, along with a yellow arrow indicating a line scan for EPMA, (b) tabulated values of at% profile, (c) concentration profiles of Si and O in wt%, and (d) concentration profiles of Fe, Si and O in at%.

4.4.3. Summary of Fe-Si Test Results

Fe-Si alloys containing Si ranging from 1.25- to 3.82 wt% were tested up to 300 hours in 600°C LBE. After disappearance of initially formed iron oxides, remaining internal oxidation zone was found under the surface. No continuous layer of SiO_2 oxide was detected. Rather, formation of oxide precipitates of Fe_2SiO_4 and SiO_2 in the internal oxidation zone was assumed.

4.5 Corrosion Behavior of Fe-Cr-Si alloys

When added with Si up to 2.55wt%, Fe-Cr alloys showed distinctive features in oxidation behavior depending on the Cr content in the base Fe-Cr alloys, including: (a) an extensive boundary diffusion, (b) a Si incorporated internal oxidation zone, or (c) effects of grain size and cold working.

4.5.1 Fe-2.25%Cr-0.5%Si and Fe-2.25%Cr- 1.25%Si

In the case of samples Fe-2.25%Cr-0.5%Si and Fe-2.25%Cr-1.25%Si, extensive grain boundary oxidation is a key characteristic observed after intermediate exposure time in 600°C LBE. During the initial exposure as shown in Figure 4-30, Fe-2.25%Cr-0.5%Si material exhibited similar oxidation as did its counterpart Fe-Cr alloy. However, after 250 hours, intensive segregation of elements around grain boundaries was detected in the X-ray map shown in Figure 4-31. This map shows the segregation of Cr, Si and O to the grain boundaries, which are roughly outlined by the map. The presence of oxygen at the same location with such elements of Cr and Si indicates that they remain in oxides form. A reduction of iron in the grain boundary is evident.

With increased Si content as in alloy as Fe-2.25%Cr-1.25%Si, more extensive grain boundary oxidation was observed. As shown in Figure 4-32, a loss of whole grain resulting from a grain boundary oxidation has occurred and the presence of Cr and Si oxides is evidenced with their strong signal inside the grain. Again, the reduction of iron is apparent on the surface of the lost grain. Further exposure of Fe-2.25%Cr-1.25%Si samples showed a more expanded grain boundary oxidation region, where the affected grain boundaries outlined as dark lines as can be seen in Figure 4-33. The distance of grain boundary oxidation front was measured as 47±5 μm from the surface, while the internal oxidation zone front inside the grain remained at 15.7±0.7 μm. This phenomenon indicates that under the testing condition, a short circuit diffusion process via grain boundaries is dominant, which is consistent with observed Cr-oxide segregation in the grain boundaries reported previously in Fe-9%Cr and Fe-12%Cr materials.

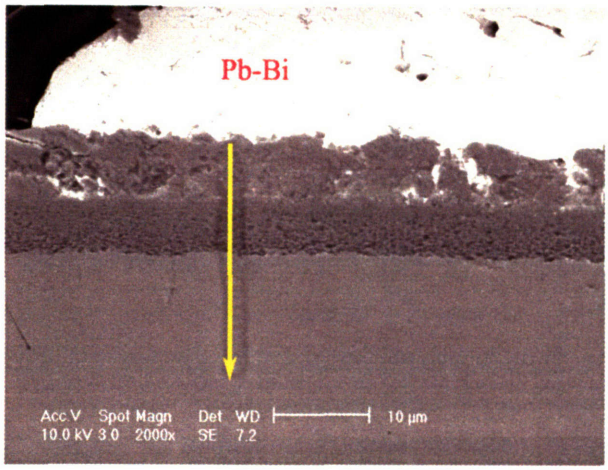

Figure 4-30 SEM image of Fe-2.25%Cr-0.5%Si material after exposure at 600°C for 100 hours.

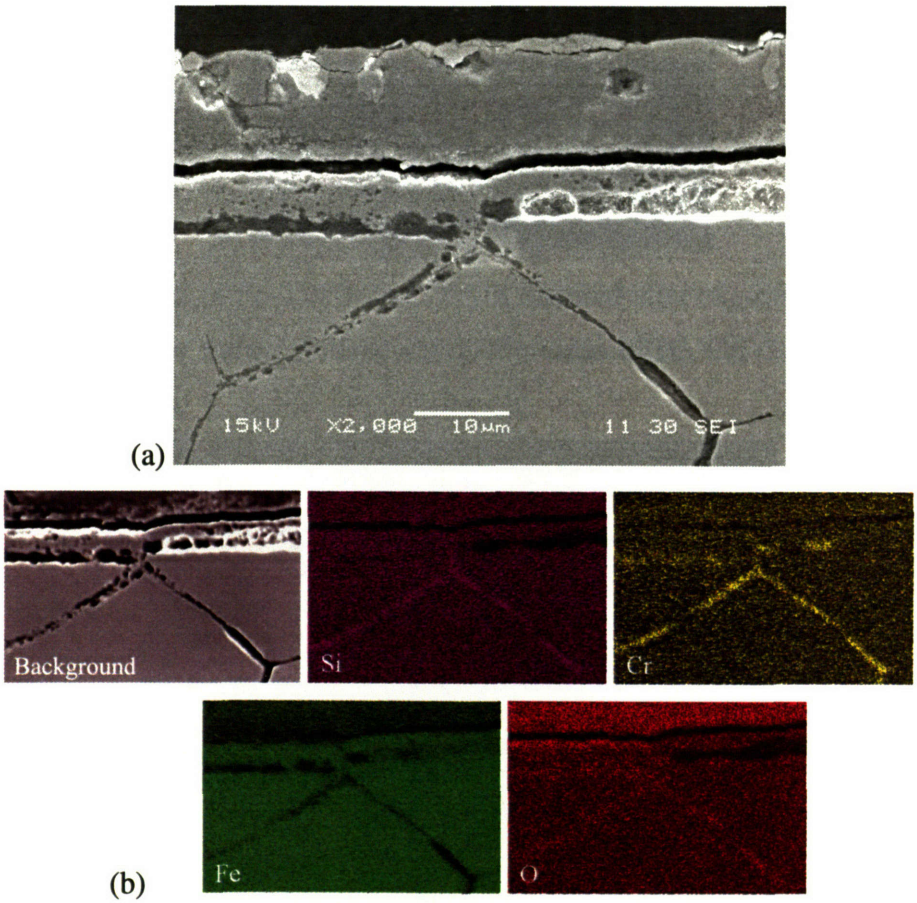

Figure 4-31 (a) SEM image of Fe-2.25%Cr-0.5%Si material after exposure at 600°C for 250 hours, (b) X-ray maps showing elemental distributions of Si, Cr, Fe, and O within the grain boundary

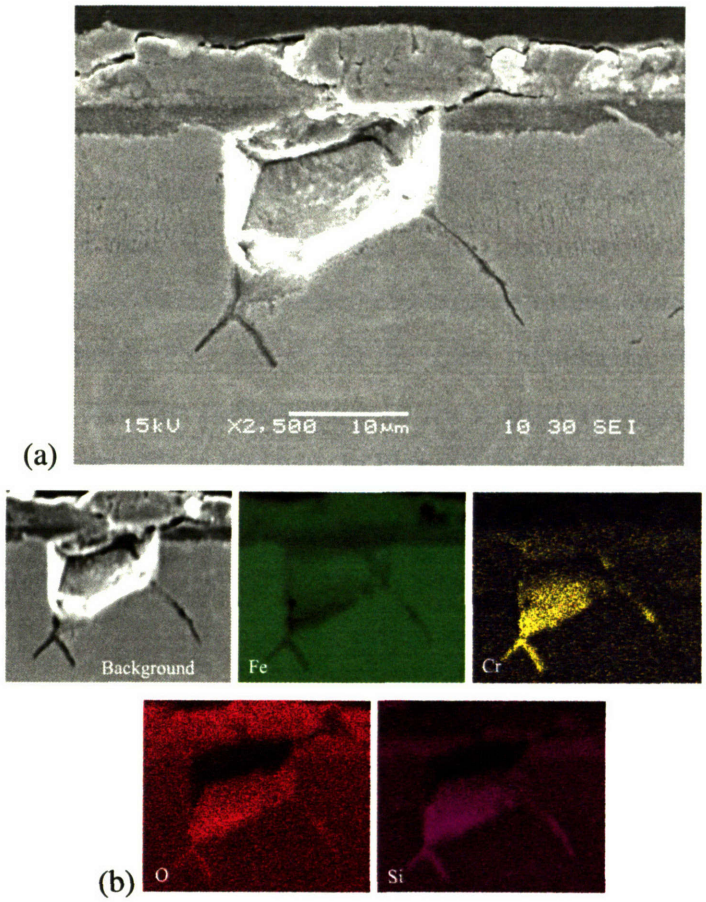

Figure 4-32 (a) SEM image of Fe-2.25%Cr-1.25%Si material after exposure at 600°C to LBE for 250 hours, (b) X-ray maps showing elemental distributions of Fe, Cr, O, and Si within the lost grain and grain boundaries.

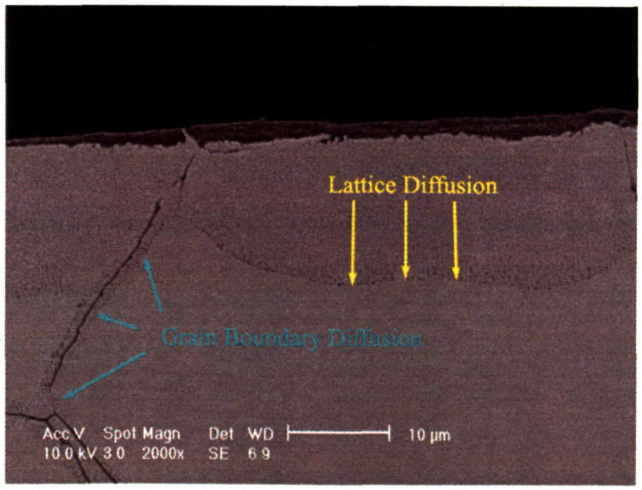

Figure 4-33 SEM image of Fe-2.25%Cr-1.25%Si material after exposure at 600°C for 300 hours, showing a clear distinction of lattice diffusion front and grain boundary diffusion region.

4.5.2. Fe-12%Cr-0.5%Si

EPMA data of sample Fe-12%Cr-0.5%Si obtained after 100-hour exposure detected compositions close to the mixed spinel type oxide as shown in Figure 4-34. In this early stage, no clear distinction in terms of oxide morphology and composition was observed as a result of the Si addition, when compared to Fe-12%Cr. After 250-hour exposure, X-ray maps in Figure 4-35 show increased concentrations of Cr and O in the grain boundaries, where iron depletion is observed as well. Due to the low concentration of Si, a clear segregation of Si in the grain boundaries was hardly discernable in the map. In Figure 4-36, only oxide morphology similar to that in the internal oxidation is shown. The origin and time of formation will be discussed in detail in the following chapter.

(a)

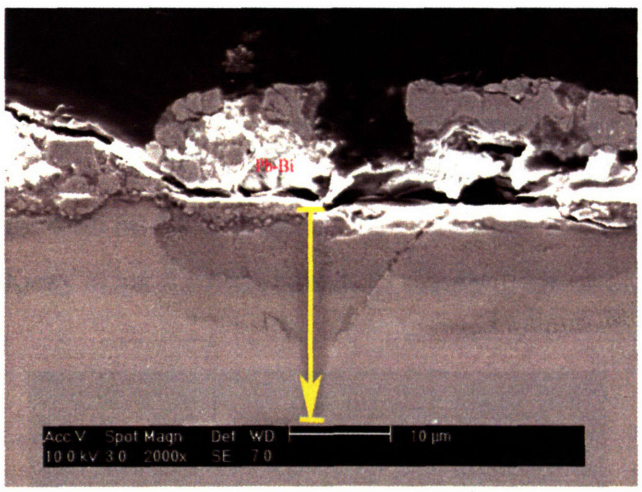

(b)

Sample	µm	Concentration (atomic%) Fe	Cr	Si	O
Fe-12%Cr-0.5%Si	0	34.93	8.22	0.94	55.87
	1	32.90	10.09	0.33	56.67
	2	31.36	11.52	0.59	56.52
	3	33.70	12.16	0.72	53.42
	4	31.86	12.67	0.85	54.62
	5	31.42	12.73	0.49	55.37
	6	31.40	12.10	0.38	56.12
	7	35.40	12.00	0.44	52.16
	8	49.14	11.86	0.48	38.48
	9	57.59	11.99	0.52	29.90
	10	59.82	12.04	0.57	27.57
	11	61.15	12.11	0.55	26.20
	12	60.72	12.44	0.63	26.21
	13	61.31	12.21	0.79	25.70
	14	78.35	12.13	1.72	7.80
	15	85.98	12.43	0.75	0.84
	16	89.61	9.28	0.74	0.37
	17	90.56	8.56	0.73	0.14
	18	85.61	13.35	0.87	0.18

Figure 4-34 (a) SEM image of Fe-12%Cr-0.5%Si after exposure at 600°C for 100 hours, along with a yellow arrow indicating scanned area for EPMA, (b) tabulated values of Fe, Cr, Si and O concentration in at%.

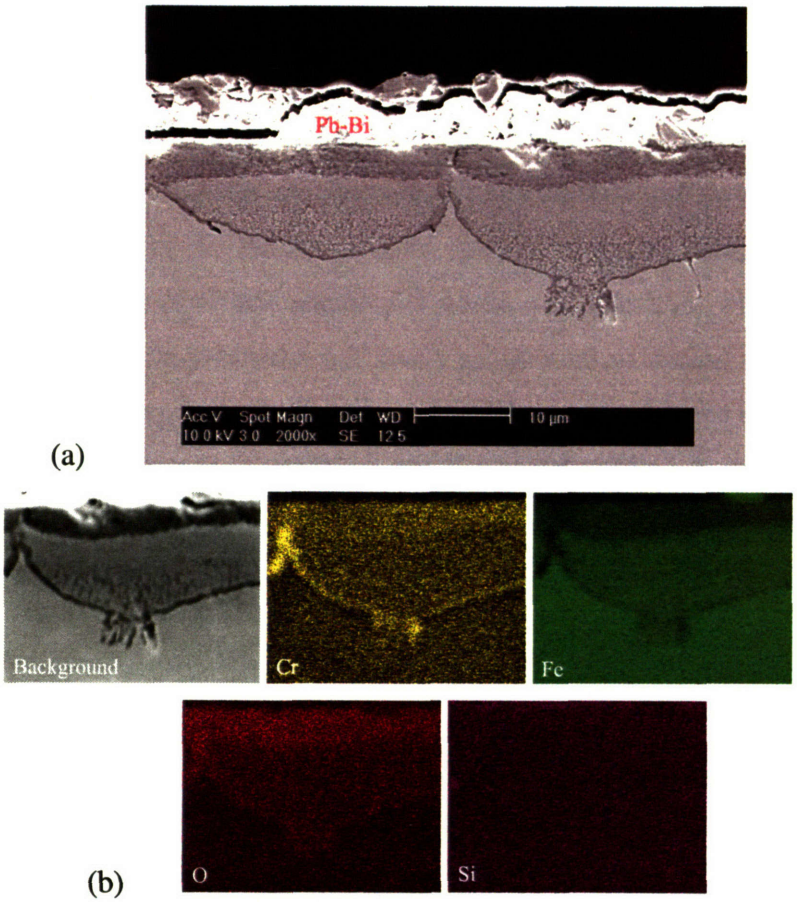

Figure 4-35 (a) SEM image of Fe-12%Cr-0.5%Si material after exposure at 600°C for 250 hours, (b) X-ray maps showing elemental distributions of Si, Cr, Fe, and O within the oxide layer.

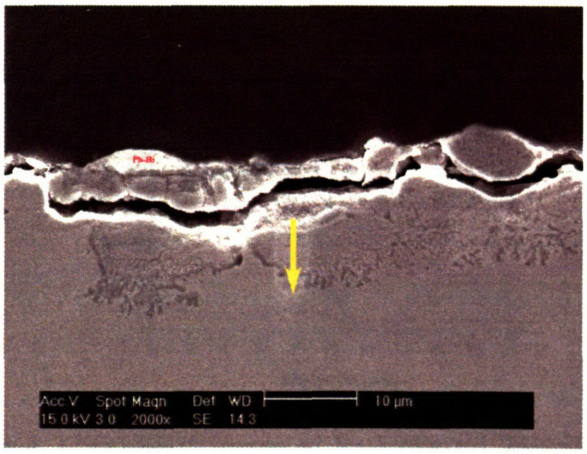

(a)

(b)

Concentration (atomic%)					
Sample	µm	Fe	Cr	Si	O
Fe-12%Cr-0.5%Si	0	30.90	11.27	0.93	56.49
	1	35.26	9.52	0.61	53.88
	2	73.74	6.05	0.37	19.77
	3	58.92	12.13	0.78	28.15
	4	58.99	12.35	0.74	27.89
	5	59.80	12.22	0.73	27.23
	6	59.25	12.12	0.76	27.86
	7	35.33	20.80	1.20	42.67
	8	81.89	8.71	0.65	8.74

Figure 4-36 (a) SEM image of Fe-12%Cr-0.5%Si after exposure at 600°C for 500 hours, along with a yellow arrow indicating scanned area for EPMA, (b) tabulated values of at% profile Fe, Cr, Si and O.

4.5.3. Fe-12%Cr-1.25%Si

With the increase in the Si content in alloy, an increased Si concentration in the oxide layers were observed even at the early stage of exposure. As can be seen in Figure 4-37, the formation of interaction layer with three distinctive morphologies occurs, consisting of a compact, dark oxide having oxygen content of 50 at% and Si of 3.3 at%, a middle layer with less oxygen and Si content, 30 at% and 2 at%, respectively, and lastly an internal oxidation zone with a web-like structure made of oxide precipitates. In an enlarged SEM image of Figure 4-38, taken after 250-hour exposure, the same structure is exhibited and the corresponding X-ray maps show a clear enrichment in the concentration of Cr, Si, and O in the top layer as well as at the boundary of internal oxidation zone with the base metal. Reduced iron concentration was detected in the top layer.

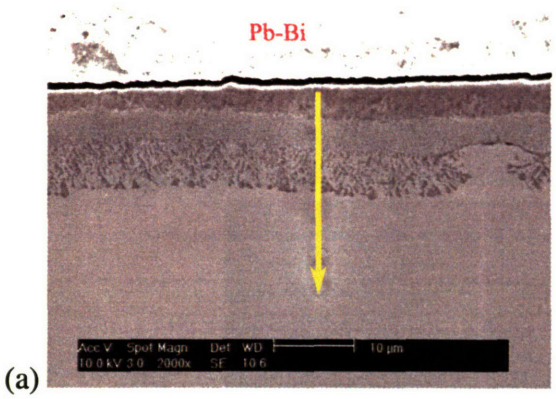

(a)

(b)

Sample	µm	Fe	Cr	Si	O
		Concentration (atomic%)			
Fe-12%Cr-1.25%Si	0	26.77	18.65	3.32	50.79
	1	25.67	18.85	3.36	51.63
	2	53.97	11.84	2.19	32.01
	3	53.49	12.27	2.19	32.00
	4	53.76	12.20	2.25	31.78
	5	53.10	12.30	2.17	32.42
	6	56.15	13.20	2.38	28.21
	7	50.56	15.83	2.88	30.73
	8	51.15	14.65	2.77	31.37
	9	53.49	13.68	2.45	30.36
	10	73.63	10.15	2.15	14.16
	11	86.32	12.06	1.58	0.00
	12	88.94	9.96	1.08	0.00
	13	85.73	12.46	1.79	0.00
	14	85.14	12.91	1.96	0.00
	15	84.97	12.88	2.09	0.00
	16	84.88	12.96	2.14	0.00
	17	84.79	12.96	2.17	0.00
	18	84.97	12.87	2.16	0.00
	19	84.98	12.80	2.21	0.00
	20	84.77	13.10	2.13	0.00

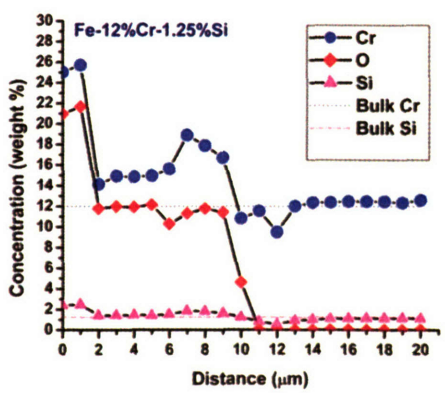

(c)

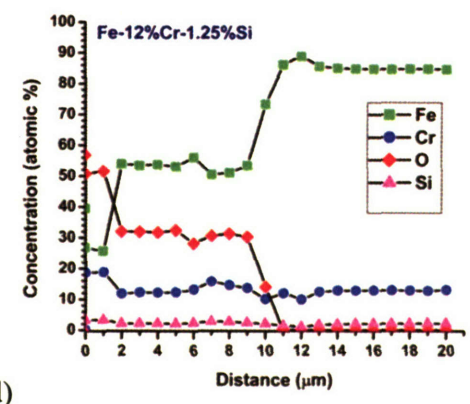

(d)

Figure 4-37 (a) SEM image of Fe-12%Cr-1.25%Si after exposure at 600°C for 100 hours, along with a yellow arrow indicating EPMA region, (b) tabulated values of at% profile, (c) concentration profiles of Cr, Si and O in wt%, and (d) concentration profiles of Fe, Cr, Si and O in at%.

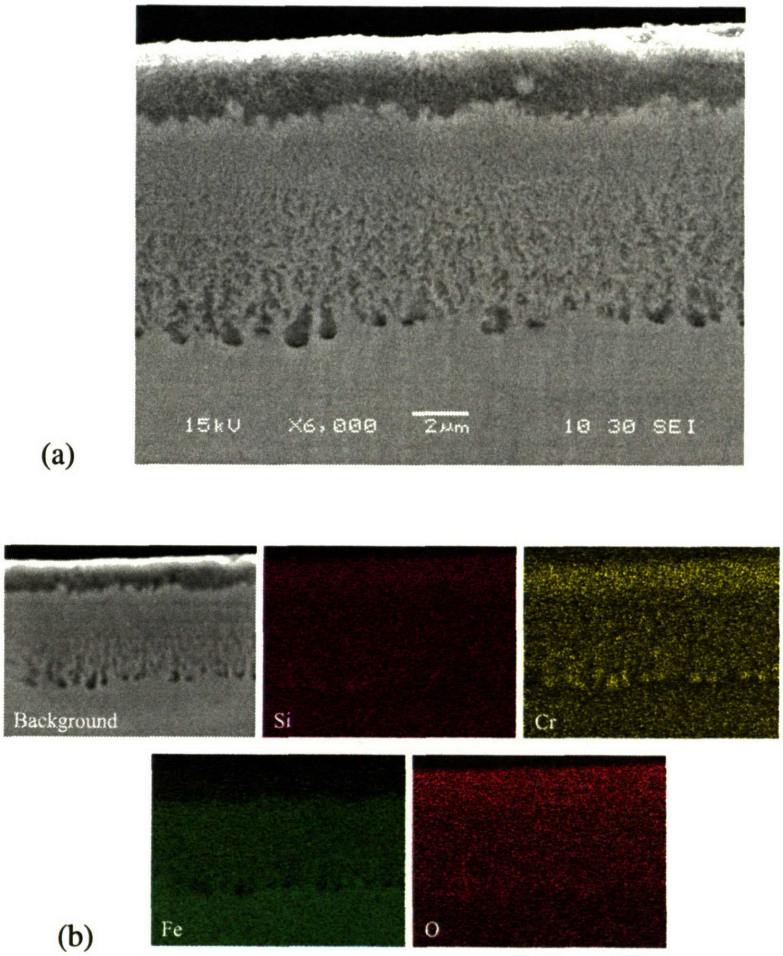

Figure 4-38 (a) SEM image of Fe-12%Cr-1.25%Si material after exposure at 600°C for 250 hours, (b) X-ray maps showing elemental distributions of Si, Cr, Fe, and O within the oxide layer, and enrichments of Cr and O at the interface between the oxide and the base metal.

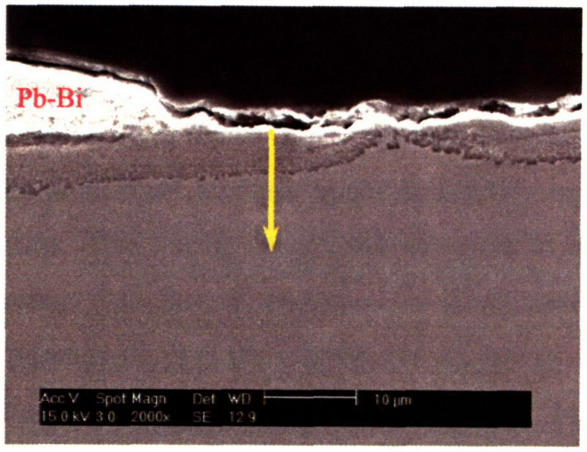

(a)

(b)

Sample	µm	Concentration (atomic%) Fe	Cr	Si	O
Fe-12%Cr-1.25%Si	0	54.32	12.41	2.14	31.08
	1	55.68	12.34	2.08	29.82
	2	46.99	15.04	2.26	35.67
	3	42.45	15.55	2.99	38.97
	4	47.73	14.73	2.32	35.18
	5	52.98	12.38	4.83	29.77
	6	89.55	9.21	1.22	0.00
	7	85.70	12.38	1.88	0.00
	8	84.58	13.23	2.16	0.00
	9	84.64	13.14	2.16	0.00
	10	84.55	13.24	2.17	0.00
	11	84.61	13.15	2.21	0.00

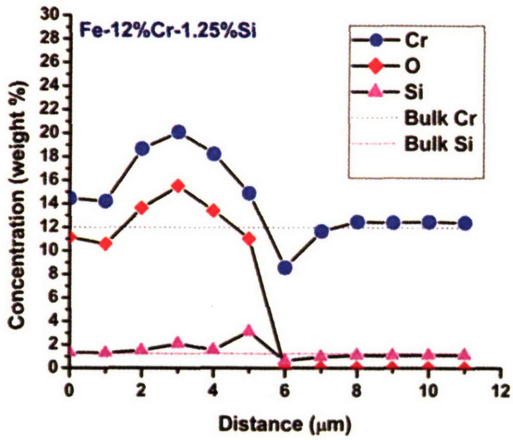

(c)

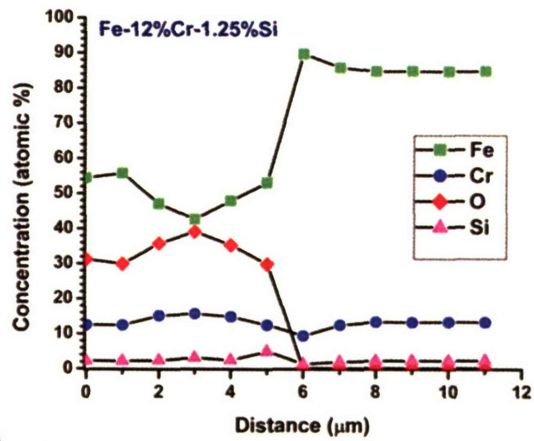

(d)

Figure 4-39 (a) SEM image of Fe-12%Cr-1.25%Si after exposure at 600°C for 500 hours, along with a yellow line indicating a line scan location for EPMA, (b) tabulated values of at% profile, (c) concentration profiles of Cr, Si and O in wt%, and (d) concentration profiles of Fe, Cr, Si and O in at%.

The EPMA results, obtained after 500-hour exposure and shown in Figure 4-39, reveals the presence of one type of interaction layer having too low an oxygen concentration to be in the form of an oxide.

4.5.4. Fe-18%Cr-0.5%Si

The initial of oxide formed on Fe-18%Cr-0.5%Si material has a composition similar to $(Fe,Cr)_2O_3$ except for the slight increase in Si content near the interface of oxide/base metal as can be seen in Figure 4-40. The composition is comparable to that obtained from Fe-18%Cr,

along with similar compact appearance in oxide morphology. The oxygen concentration in at% was fairly uniform within the oxide, but the Cr concentration increased slightly as did Si near the lower boundary of oxide. In the 500-hour exposure material shown in Figure 4-41, it can be seen that no significant increase in the interaction layer thickness was observed after longer term exposure. This result shares the common features with the previous Fe-12%Cr-1.25%Si, indicating that further oxidation of base metal has been hindered possibly due to the incorporation of Si at the interface of oxide/base metal. Compared to the samples of Fe-12%Cr and Fe-18%Cr, which showed a significant increase in the interaction layer after 500-hour exposure, it is clear that the addition of Si has affected the reaction kinetics of these alloys.

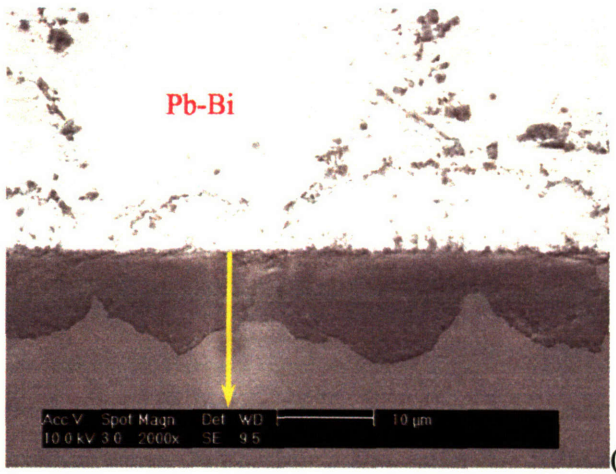

(a)

(b)

Sample	µm	Concentration (atomic%) Fe	Cr	Si	O
Fe-18%Cr-0.5%Si	0	27.02	15.16	1.15	56.31
	1	20.44	20.19	0.57	58.68
	2	19.97	20.44	0.68	58.78
	3	22.38	18.42	0.62	58.47
	4	19.54	20.39	0.56	59.45
	5	21.06	20.91	0.81	57.15
	6	20.31	21.08	0.77	57.81
	7	14.15	26.62	1.78	57.43
	8	14.01	26.79	1.96	57.18
	9	13.66	26.07	1.99	58.21
	10	51.11	17.03	1.61	30.13
	11	85.76	13.72	0.48	0.00
	12	83.09	16.39	0.51	0.00
	13	83.24	16.20	0.53	0.00
	14	83.33	16.10	0.52	0.00

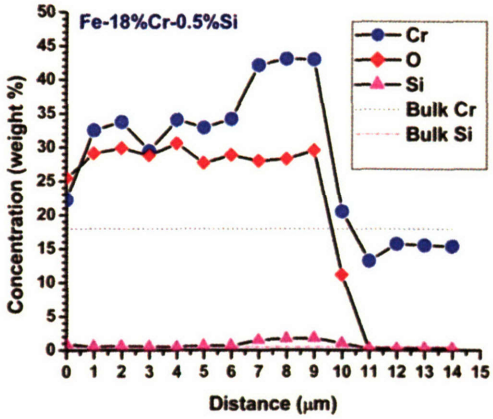

(c)

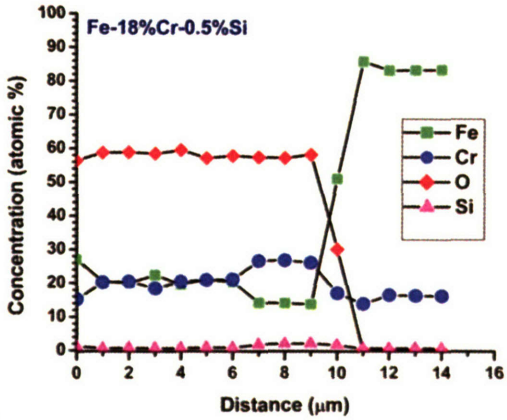

(d)

Figure 4-40 (a) SEM image of Fe-18%Cr-0.5%Si after exposure at 600°C for 100 hours, along with a yellow arrow indicating a scan for EPMA, (b) tabulated values of at% profile, (c) concentration profiles of Cr, Si and O in wt%, and (d) concentration profiles of Fe, Cr, Si and O in at%.

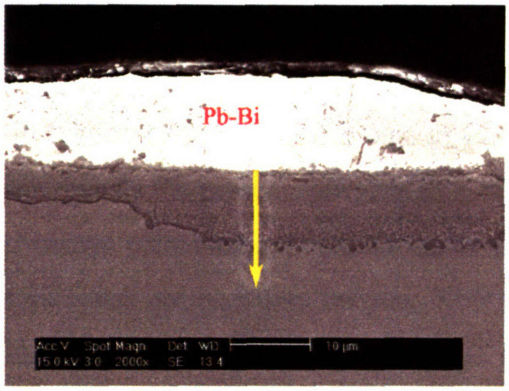

(a)

Sample	μm	Fe	Cr	Si	O
		Concentration (atomic%)			
Fe-18%Cr-0.5%Si	0	18.83	20.05	2.53	57.37
	1	18.85	19.80	2.41	57.68
	2	19.10	21.42	2.12	56.71
	3	24.13	20.80	1.62	53.16
	4	25.39	20.39	1.43	52.57
	5	39.49	17.97	0.73	41.77
	6	41.61	17.92	0.68	39.79
	7	42.77	17.71	0.67	38.83
	8	69.76	15.30	1.88	13.02
	9	83.24	16.44	0.30	0.00
	10	81.61	18.00	0.38	0.00
	11	83.87	15.87	0.26	0.00

(b)

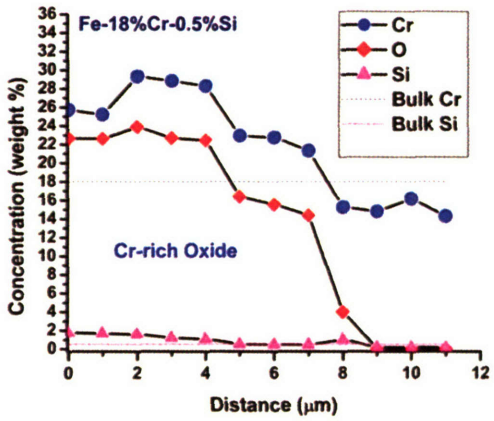

(c)

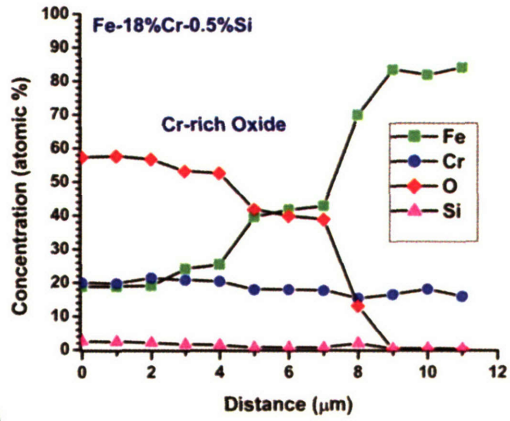

(d)

Figure 4-41 (a) SEM image of Fe-18%Cr-0.5%Si after exposure at 600°C for 500 hours, along with a yellow arrow indicating a line scan for EPMA, (b) tabulated values of at% profile, (c) concentration profiles of Cr, Si and O in wt%, and (d) concentration profiles of Fe, Cr, Si and O in at%.

4.5.5 Fe-18%Cr-1.25%Si and Fe-18%Cr-2.55%Si

Results obtained from Fe-18%Cr-1.25%Si and Fe-18%Cr-2.55%Si need to be interpreted carefully with respect to the grain size effect. Among Fe-Cr-Si samples made by custom melting, these two materials have extremely large grains ranging in size from 500μm to 2~3000 μm. Thus, the resultant data are expected to have very thin interaction layer, considering that grain boundary diffusion is dominant during exposure, as evidenced by the Fe-2.25%Cr-1.25%Si results. A comparison was made by testing a different sample, with small grains (~10μm) and

heavy cold work (about 75%), but having the same composition as Fe-18%Cr-2.55%Si to verify the expected differences in test result.

As shown in Figure 4-42, the SEM image of Fe-18%Cr-2.55%Si material tested at 600°C LBE for 500 hours reveals the presence of very thin oxide film on its surface. The compositional map of the layer shows increased concentrations of Cr, Si and O in the layer. Due to its thickness, EPMA analysis was not possible, instead, XPS was employed to obtain the chemical bonding states of this oxide. In XPS survey spectra as seen in Figure 4-43, no presence of iron was detected and the existence of Si and Cr as oxides are likely. The resultant identification of oxides are shown in Figure 4-44, from the high resolution data collected in the vicinity of Cr (2p) and Si (2p) binding energy. Cr is in the chemical state of Cr_2O_3, and Si of SiO_2. Additional information on the oxide phases were obtained by XRD analysis. As seen in Figure 4-45, the major phase peaks detected in Fe-18%Cr-1.25%Si material after 500-hour exposure are still BCC phase peaks resulting from the base material. Only small peaks of oxides were found and this again confirms the thinness of surface film. In the rescaled axis, the phases of Cr_2O_3, SiO_2 and other Si related phases can be seen as shown in Figure 4-46. A presence of intermediate phases such as $FeSi_2$ and Cr_3Si was also detected from a detailed peak identification.

Experimental results obtained from Fe-18%Cr-2.55%Si material showed the same features as Fe-18%Cr-1.25%Si. In Figure 4-47, SEM image taken after 250-hour exposure showed a very thin interaction layer, and the XPS spectra as shown in Figures 4-48 and 4-49 detected Cr_2O_3 and SiO_2 bonding states from Fe-18%Cr-2.55%Si sample tested for 500 hours. XRD analysis also explains the presence of Cr_2O_3, SiO_2 and other Si related phases in the tested sample as can be seen in Figure 4-50.

When a sample with a much smaller grain size was tested for 300 hours at 600°C LBE, a striking difference in the oxidation behavior was detected. As can be seen in Figure 4-51, an extensive grain boundary oxidation, covering the entire sample surface and outlining regions inside where Cr and Si oxides precipitates form a web-like network structure. This sample has a small grain size (~10μm) and was cold worked heavily (75%) after the initial homogenization process as explained previously in the section 3.1.1. It has the same composition of Fe-18%Cr-2.55%Si. Therefore, it can be concluded that the dominant process of interaction layer formation

at the test condition occurred via grain boundary diffusion. The reduction of such short circuit paths due to a large grain size, combined with its high Cr and Si concentration has produced only a thin surface layer. However, when the surface diffusion through grain boundary is facilitated by reduction of grain size, the formations of surface film, affected grains by oxidation, and an internal oxidation zone can be detected all at the same time, as indicated by Figure 4-51. Therefore, at temperatures around 600°C, it is important to take the grain boundary effect into considerations when designing corrosion resistant alloy systems to LBE based on their oxide protectiveness.

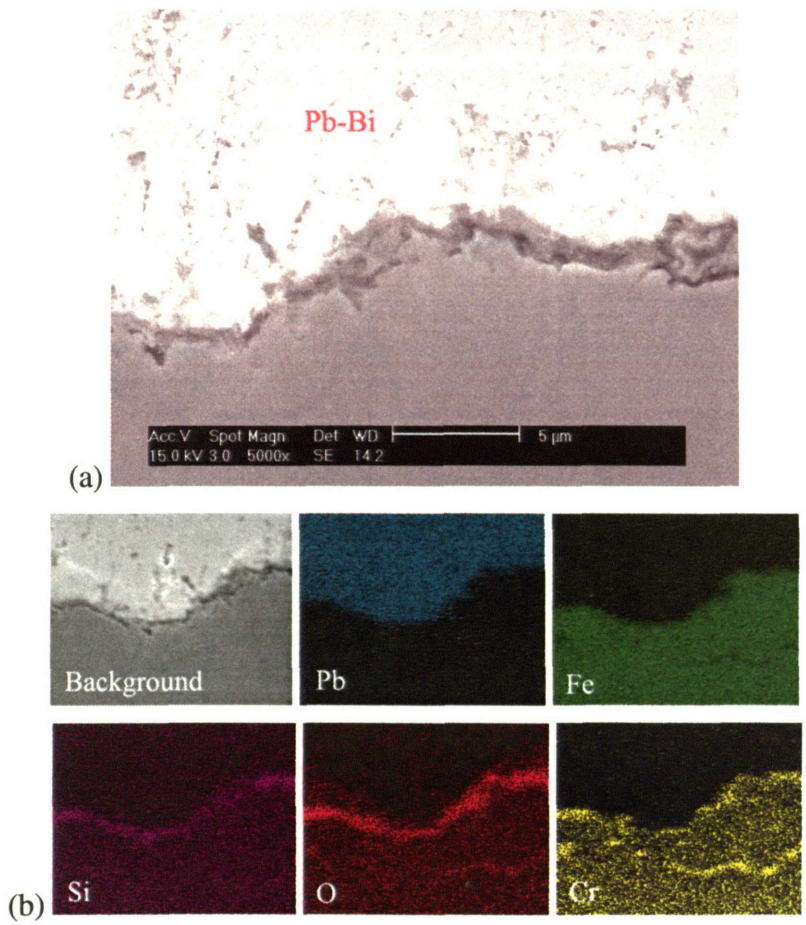

Figure 4-42 (a) SEM image of Fe-18%Cr-1.25%Si sample after exposure at 600°C for 500 hours,(b) X-ray maps showing elemental distributions of Si, Cr, Fe, and O within the interaction layer, where clear enrichment of Si, O and Cr is observed.

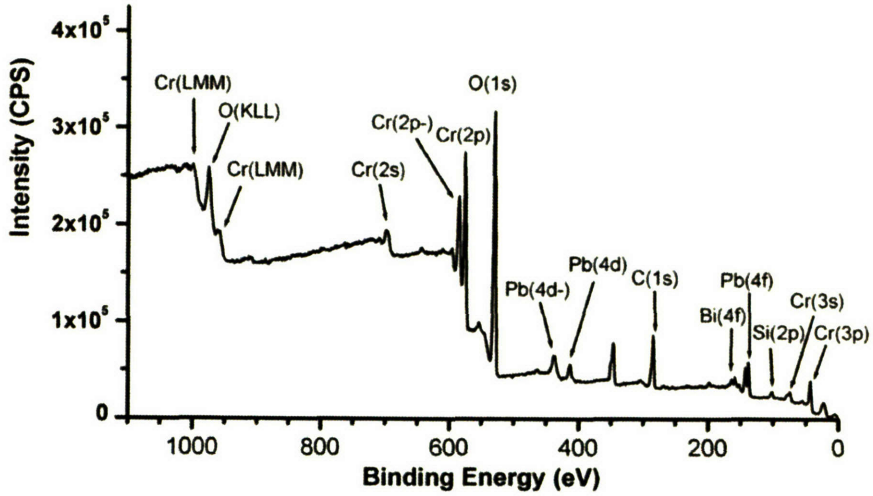

Figure 4-43 XPS survey spectra for Fe-18%Cr-1.25%Si sample after exposure at 600°C for 500 hours. Spin-orbit splitting of Cr is represented by Cr(2p-) for Cr($2p_{1/2}$), and Cr(2p) for Cr($2p_{3/2}$).

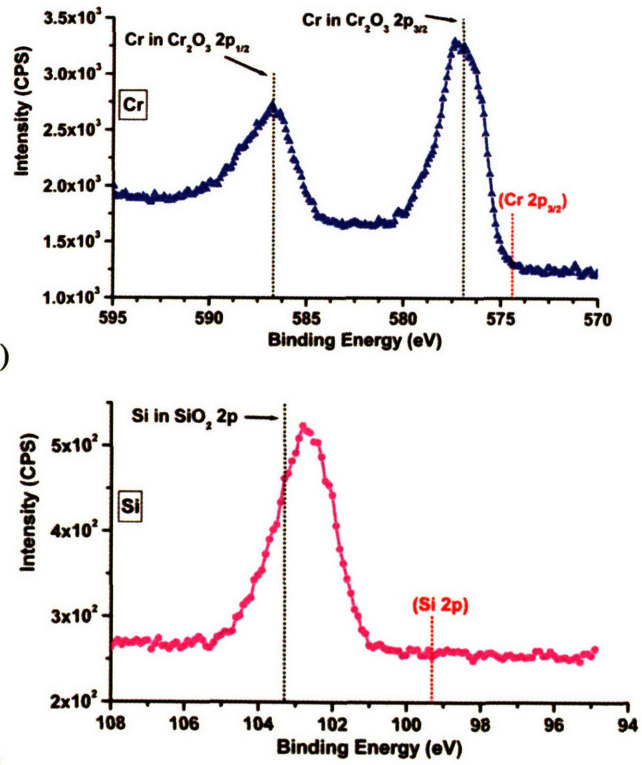

Figure 4-44 XPS high-resolution spectra of (a) Cr and (b) Si obtained from Fe-18%Cr-1.25%Si material tested in 600°C LBE for 500 hours, presented with a charge correction to adventitious hydrocarbon at 285.0eV.

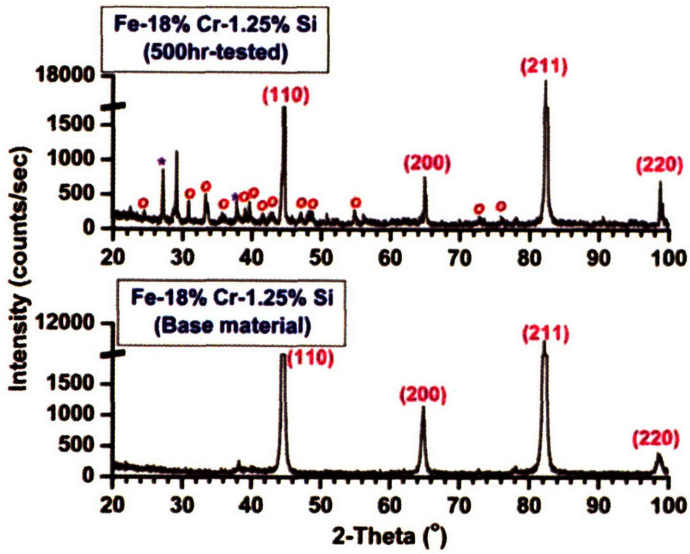

Figure 4-45 XRD spectra of Fe-18%Cr-1.25%Si material showing the existing phase peak after exposure at 600°C for 500 hours (upper graph, O: oxide peaks, *: Pb-Bi peaks) in comparison to that of the base material (lower graph, BCC phase, Miller indices).

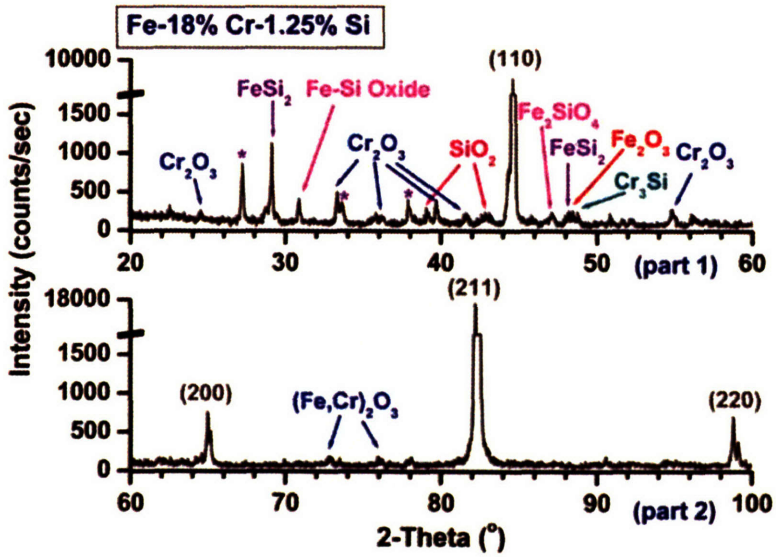

Figure 4-46 XRD spectra of Fe-18%Cr-1.25%Si material tested in LBE at 600°C for 500-hour showing a detailed oxides peak identification.

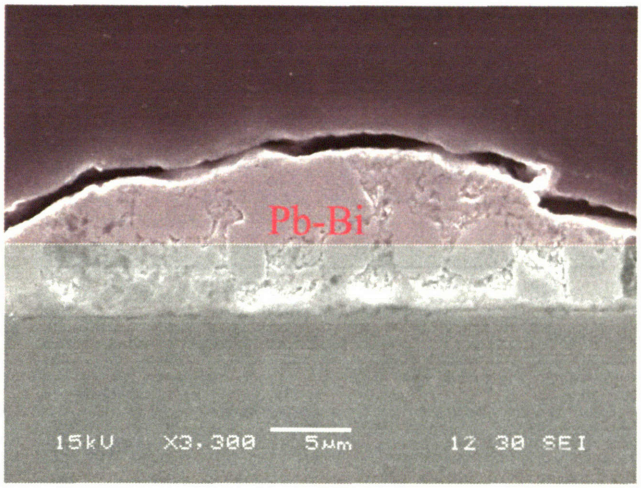

Figure 4-47 SEM image of Fe-18%Cr-2.55%Si material showing a very thin interaction layer formed during the 250-hour exposure to 600°C LBE.

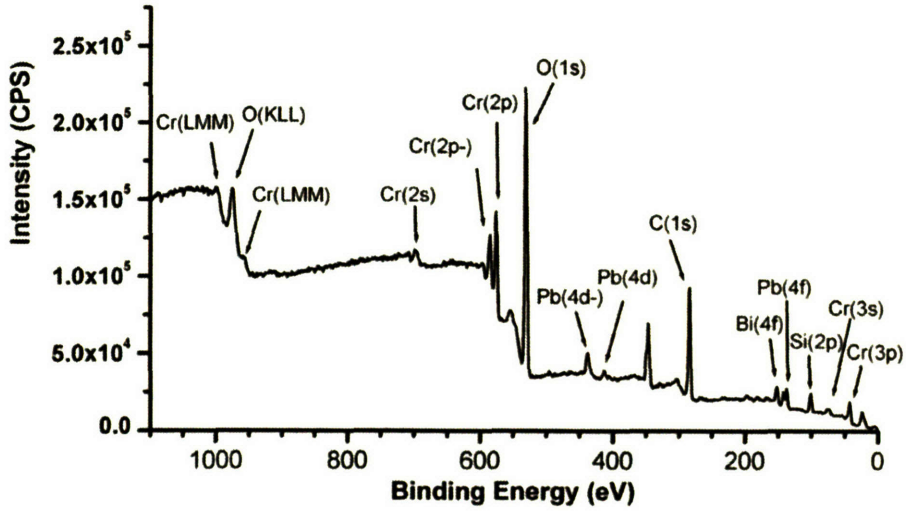

Figure 4-48 XPS survey spectra for Fe-18%Cr-2.55%Si material after exposure at 600°C for 250 hours. Spin-orbit splitting of Cr is represented by Cr(2p-) for Cr($2p_{1/2}$), and Cr(2p) for Cr($2p_{3/2}$).

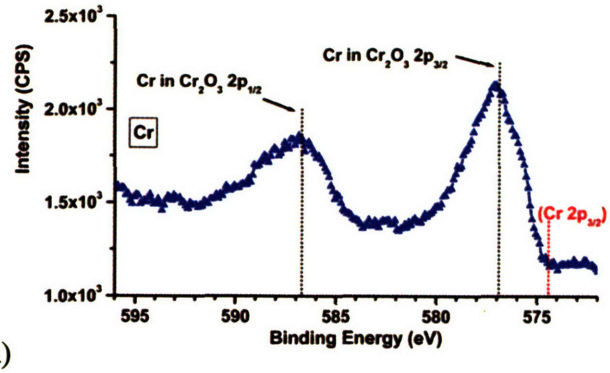

(a)

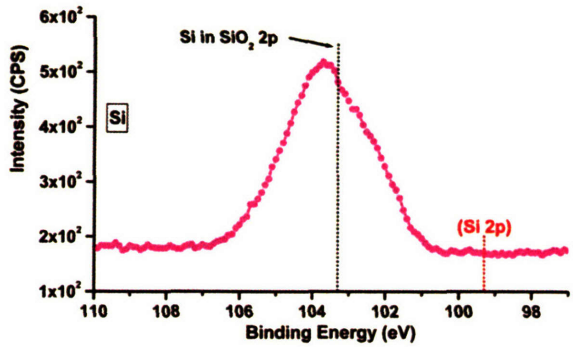

(b)

Figure 4-49 XPS high-resolution spectra of (a) Cr and (b) Si obtained from Fe-18%Cr-2.55%Si material after exposure at 600°C for 500 hours, presented with a charge correction to adventitious hydrocarbon at 285.0eV.

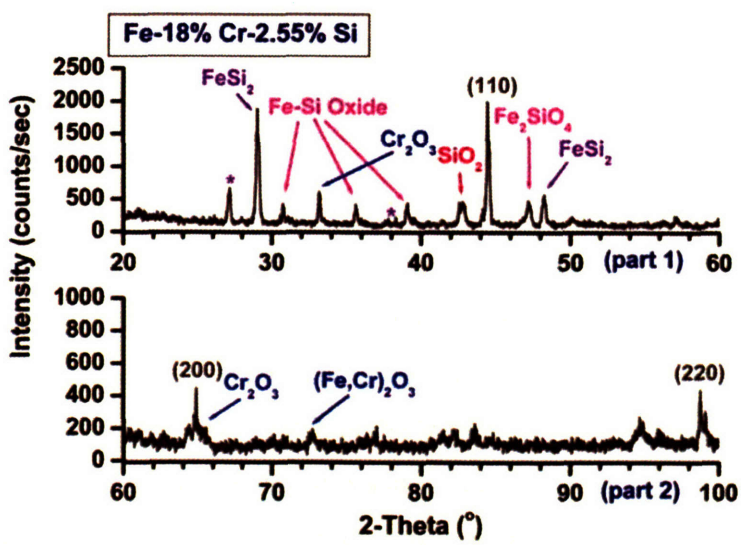

Figure 4-50 XRD spectra of Fe-18%Cr-2.55%Si material after exposure at 600°C for 500 hours showing a detailed oxides peak identification.

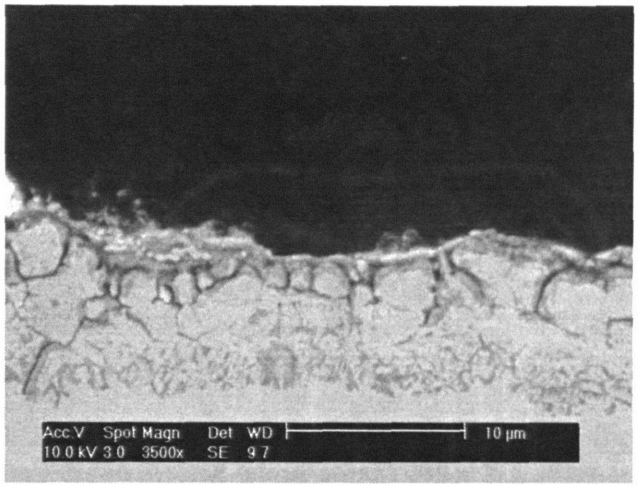

Figure 4-51 SEM image of heavily cold worked, small grain sized material with the same composition as Fe-18%Cr-2.55%Si. It shows extensive grain boundary oxidation, outlining regions inside where Cr and Si oxides precipitates form a web-like network structure. Image obtained after 300-hour exposure to 600°C LBE.

4.5.6. Summary of Fe-Cr-Si Test Results

- Fe-2.25wt%Cr alloyed with Si of 0.5- and 1.25wt% showed increased internal oxidation due to enhanced grain boundary diffusion. The segregation of Cr, Si and O to the grain boundary was clearly evidenced.

- The addition of Si into Fe-12wt%Cr and Fe-18wt%Cr resulted in a reduction of interaction layer thickness with increase in test duration. With 0.5wt%Si addition to Fe-12Cr, the contribution of Si to the change in the reaction kinetics may be considered minor. However, Si-rich oxide precipitates were detected for Fe-12%Cr-1.25%Si at the oxide/metal boundary. A decrease in the interaction layer thickness might be accounted for such formation of oxide, blocking further diffusion of oxidants through the boundary, while the loss of external oxide layer was going on. Similar reduction of interaction layer thickness was detected for Fe-18wt%Cr-0.5wt%Si.

- The formation of very thin interaction layer, based on Cr_2O_3 and SiO_2 oxides, was reported for those alloys of Fe-18wt%Cr-1.25wt%Si and Fe-18wt%Cr-2.55wt%Si. However, considerations on the grain size effect were required to explain the underlying cause correctly. The large grain size of material as well as the abundant Cr and Si concentration were accounted for the "very" thin oxide layer formation.

4.6 References

[1] J. Chastain and R. C. King, Jr.(eds.), Handbook of X-ray Photoelectron Spectroscopy, Physical Electronics, Inc., Eden Prairie, Minnesota, 1995.

[2] S. Nasrazadani and A. Raman, "The Application of Infrared Spectroscopy to the Study of Rust Systems–II. Study of Cation Deficiency in Magnetite Produced during its Transformation to Maghemite and Hematite", *Corrosion Science*, **34** (1993) pp. 1355-1365.

[3] C. A. Barrero et al., "Synthesis of Magnetite in Presence of Cu^{2+} or Cr^{3+}", *Hyperfine Interactions* , **134** (2001) pp. 141–152.

[4] P. Kofstad, High Temperature Corrosion, Elsevier Applied Science, New York, 1988.

[5] M. Schütze, Protective Oxide Scales and Their Breakdown, John Wiley & Sons, UK, 1997.

[6] A. Atkinson, "A Theoretical Analysis of the Oxidation of Fe-Si Alloys", *Corrosion Science*, **22** (1982) pp.87-102.

[7] F. Stott, "Influence of Alloy Additions to Oxidation", *Materials Science and Technology*, **5** (1989) pp.734-740.

CHAPTER 5

DISCUSSION

As was discussed earlier, the "thesis" that an Fe-Cr-Si alloy would be resistant to corrosion in Pb and Pb alloys over a wide range of oxygen potentials has been proven by the experimental results. This behavior has been achieved through the use of elements (Cr and Si) that separately (Si) and in cooperation (Si + Cr) establish a protective film at oxygen potentials above the formation potential for Si-oxides. At very low oxygen potentials, the dissolution process results in an enrichment if low solubility Si in the surface region. This reduces further dissolution at oxygen potentials below the Si-oxide formation potential.

In this chapter the focus will be on a rationalization of the observations in comparison with the current theories of scale formation in oxygen containing environments. However, in the case at hand, there is the additional process by which continuous dissolution into the liquid metal is occurring at the same time that a surface film/scale may be forming.

Recalling that the expected role of oxide films is the mitigation of Pb-alloy corrosion by the formation of a stable diffusion barrier on the structural metal surface, it is crucial to assess the effect of alloying Cr and/or Si from their kinetic nature and stability viewpoints. This chapter presents a detailed discussion of the experimental results reported in Chapter 4, which focuses on the compositional variance of the oxide and the change in kinetics due to alloying.

Rationalization of Presence of Fe-Oxides at Oxygen Potentials "below" the Oxide Formation Potential

As discussed earlier, the presence of iron oxides observed on the surfaces originated from residual oxides of Pb and Bi and/or oxygen dissolved in the Pb and Bi. It was impossible to purchase oxygen-fee starting material. The initial oxidation of iron resulted from the reaction of this oxygen and/or with Pb and Bi surface oxides as observed in early stages of exposure.

However, due to the very low oxygen partial pressure maintained in the cover gas, which was evidenced by the lack of scale formation on control samples as shown in Figure 4-1, and the high oxygen diffusivity in LBE, the complete removal of initial oxygen was believed to occur in the first 30 hours of exposure, leaving the LBE in equilibrium with the cover gas composition. The porous, iron oxides embedded in solidified LBE is evidence that indicates an interrupted oxygen supply to the system and the resultant de-stabilization of iron oxides. In addition, the relatively constant oxide thickness of iron-rich oxides showing little dependence on the test duration, as shown in Fe-1wt %Cr and Fe-2.25wt% Cr alloys, is another supporting evidence of early detachment of such films, when the fast growing nature of iron oxides (especially wüstite) above 570°C is considered. Therefore, the kinetic aspects of materials observed during the longer term exposure were not affected considerably by the initial presence of oxygen and the oxygen concentration can be assumed to be kept below the iron oxide formation range after the initial transient period of about 30 hours.

The actual experimental condition (temporal scenario) rather incidentally mimicked a postulated failure scenario where an originally intended higher oxygen control did not function and the system was left with very low oxygen concentration for which a stable iron based oxide formation was not possible. In such cases, the present results can be viewed as a demonstration of the effectiveness of chrome and silicon based oxide films formed on the relevant iron alloys in terms of providing corrosion protection under such adverse environment that might happen during operation of a large scale system. As mentioned earlier, in the following discussions on the kinetic processes of the model alloys, the oxygen concentration in the system is assumed to be maintained well below the iron oxide formation level, with the test results of samples placed in the cover gas condition (Figures 4-1~5) as supporting evidence.

5.1 Effect of Alloying on LBE Corrosion

5.1.1 External vs. Internal Oxidation (Fe-Cr alloys)

From the experimental results of Fe-Cr alloy presented in the previous chapter, the morphology of oxides observed after 500-hour exposure can be summarized as consisting of

three forms : (a) an external oxide scale having a duplex structure of outer iron oxide and inner Cr-rich oxide, observed in low Cr (1~2.25 wt%) compositions, (b) a mixed mode of scale formation showing internal oxidation beneath the external scales, which was observed in Fe-Cr alloys with intermediate Cr (9~12wt%) content, and (c) an exclusive scale formation of $(Fe,Cr)_2O_3$ solid solution in Fe-18wt% Cr alloy. Similar findings have been reported by various researchers[1-7].

As can be seen in Figures 4-8 (Fe-1wt%Cr) and 4-10 (Fe-2wt%Cr), Fe-Cr alloys containing low Cr did not form a protective oxide on the surface under the testing condition resulting in significant LBE penetration being observed after 500 hours when tested at 600°C LBE under low oxygen conditions. With increase in Cr content, a criterion of Cr concentration for corrosion protection was seen by comparing the Fe-9wt%Cr material that showed significant LBE penetration under test condition after 500 hours, to the Fe-12wt%Cr material where no such penetration occurred. For both alloys with intermediate Cr concentration, the major oxide phase is a mixed spinel type where Cr replaces some of the iron positions. The iron-chromium spinel oxide is known to have a much reduced parabolic rate if compared with iron oxides at high temperatures [1-2]. Two distinctive features to be noted in these alloys, are the presence of an extensive internal oxidation zone beneath the spinel type oxide and the segregation of Cr and O to the grain boundaries as can be seen Figures 4-14 and 4-16. Explanations on the internal oxidation zone formation can be found in various literature sources [1,3,4]. According to Seybolt [3], internal oxidation occurred beneath the spinel oxide layer, for Fe-Cr alloys with Cr content up to 12.8%. On the contrary, no internal oxidation zone formation was formed when Fe-Cr alloys formed a Cr_2O_3 based oxide with corresponding Cr content of more than 13.6% [3]. Following this result, Birks and Meier [1] explained the internal oxidation phenomenologically as a result of the hindered movement of the outer scale from advancing inward, and usually occurs under such conditions as a pre-oxidized sample is encapsulated vacuum or a separation of oxide-metal has occurred. For the current experimental results on Fe-9wt%Cr and Fe-12wt%Cr, both conditions are relevant since the initial oxygen in LBE was able to occur to form the outer oxide of iron, which was produced by the initially higher oxygen potential than that expected from an equilibrium condition with the cover gas. This excess oxygen was consumed by the formation of iron oxides, followed by the spallation of outer oxide scale. Because of the

significant depth of the internal oxidation zone that was detected as early as 100-hour exposure, another supporting evidence was gained on the low oxygen concentration, assumed to have been reached during the early stages of exposure, allowing only the precipitation of Fe-Cr spinel particles across the extensive distance. In search of a thermodynamic explanation, Smeltzer and Whittle [4] attributed the structure of the internal oxidation forming beneath the external oxide to oxide precipitation, resulting from a "virtual" diffusion path cutting into and across the oxygen solubility curve bordering the two-phase alloy oxide field in the ternary alloy-oxygen isotherm.
As for the grain boundary oxidation, detected in both alloys with higher Cr and O segregation in the region, the work of Labun et al.[5] can be cited as a relevant explanation, which reported the formation of Cr-rich spinel oxide ridges at grain boundaries as a result of preferential oxidation by rapid Cr and O diffusion along the alloy grain boundaries. The actual diffusion process forming the Cr-rich oxide is two-dimensional. Due to the enhanced transport of Cr to the interface of the base metal and the oxide scale along the grain boundaries, oxidation of Cr takes place initially along the intersection of the alloy grain boundaries with the surface. Then, it penetrates in a stepwise manner across the grains following lateral chromium diffusion from these locations. Such penetration of an internal oxidation front into the alloy takes place if there is insufficient Cr and the critical volume of Cr_2O_3 particles is not enough to allow immediate development of Cr_2O_3 layer [6].

As mentioned earlier, there is an abrupt change in oxide composition with the further increase in Cr concentration in Fe-Cr alloys. From EPMA results (Figure 4-23), the oxide layer, formed during exposure at 500°C after 250 hours of Fe-18wt%Cr, was identified as a solid solution of Fe_2O_3 and Cr_2O_3 oxides of $(Fe,Cr)_2O_3$, as a result of increased Cr activity in the alloy. No internal oxidation zone was observed, which is again consistent with the literature findings in this Cr composition [3,7].

As for the very early stages of oxidation in Fe-Cr alloys containing as high Cr as 18wt%, Kuroda et al. [7] reported the nucleation of an $(Fe,Cr)_3O_4$ spinel oxide. With further oxidation, this initial cubic spinel oxide transforms to α-$(Fe,Cr)_2O_3$ oxide having the rhombohedral structure. They attributed this initial nucleation of spinel oxide (observed during first several minutes of oxidation) to a crystallographic criteria, which dominates only at the early stages of

oxidation, favoring a cubic arrangement between oxygen and metal atoms in order to have a good lattice match with the base metal of the same cubic structure. Later, a thermodynamically stable oxide based on Cr_2O_3 is formed associated with the higher chemical reactivity of Cr. They also reported the inward growth of oxide nuclei on 18wt% Cr alloy and presumed this to be as a result of the rapid inward diffusion of oxygen exceeding the outward diffusion of iron and chromium. Therefore, as discussed earlier for Fe-9wt%Cr and Fe-12wt%Cr, the actual diffusion process forming the oxide takes place in a two-dimensional way, including a lateral diffusion of oxidant followed by the short circuit diffusion through the grain boundary. From this observation, the increase in Cr concentration and the decrease in distance of lateral diffusion (=grain size of the material) can be beneficial to form a stable, Cr based oxide which will provide an adequate protection from the LBE penetration in a shorter time span.

The kinetic nature of the interaction layer formation of tested Fe-Cr alloys are summarized in Figure 5-1, focusing on the oxide growth as a diffusion controlled mechanism. The overall trend shows a decrease in the parabolic reaction rate constant, k' (as in $x^2=2k't$, where x=thickness and t=time), with increase in Cr content in Fe-Cr alloys. As stated previously, because the formation of an iron based oxide layer is the result of initial transient behavior and does not affect the kinetic nature of the interaction layer in the later stages of a test, the low Cr (1~2.25wt%) alloys are omitted from this assessment assuming that the detached iron oxide layer growth was not sustained by diffusional processes. In the same vain, the detached iron oxides found in higher Cr alloys were excluded from the layer thickness measurement. However, the depth of internal oxidation region was included because it takes place as a diffusion controlled process in the alloys.

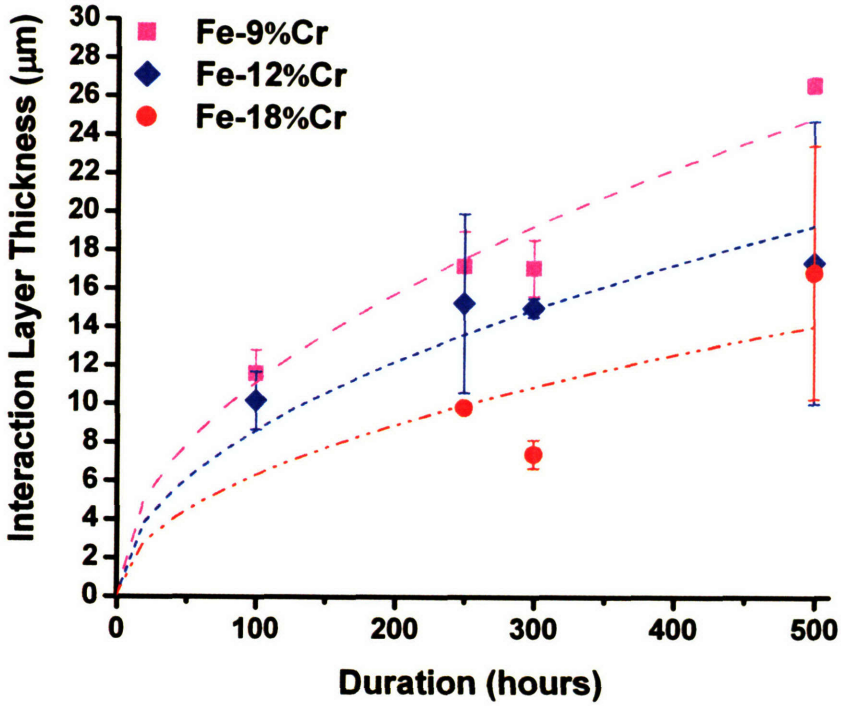

Figure 5-1. The growth of oxide layer formed on Fe-Cr alloys after 600°C LBE static test.

To further understand the diffusion process during stable oxide growth, Wagner's oxidation theory [8] is applied to oxide growth on an Fe-18wt%Cr alloy. Based on the experimental results in section 4.3.5, the oxide layer is composed primarily of iron and chromium oxides. Figure 4-23 (d) supports that the atomic compositions of the constituent elements of Fe, Cr and O are fairly constant throughout the oxide layer, if the slight increment of Cr at the metal/oxide boundary is neglected. Since no internal oxidation occurred in the metal substrate, the oxygen concentration in the metal can be set to zero. It is worth pointing out that although Cr oxide can be either a p-type or an n-type semiconductor depending on doping and oxygen partial pressure [9], the most commonly held view is that Cr_2O_3 is a p-type conductor at low temperatures (<1250°C) and relatively high oxygen activity can be applied here as Cr_2O_3 is in solid solution with Fe_2O_3. From these observations, it is assumed that the major migrating species for further growth of the oxide are chromium cations, oxygen anions, and electrons. These observations are used to support the following assumptions necessary for the application of Wagner's theory to be valid.

(1) The oxide scale is thick compared with the electrical double layer where space charge effects occur.

(2) The oxide layer is compact, and adherent with little deviation from stoichiometry.

(3) The solubility of oxygen in the metal is negligible and no other process such as oxide evaporation occurs at the interface.

(4) The diffusion of ions or electrons across the oxide scale is the rate controlling process.

(5) The thermodynamic equilibria are established on both metal/oxide and oxide/oxidant interfaces.

(6) The thermodynamic equilibrium is established locally through the growing oxide,

In Wagner's oxidation theory, the environment is assumed as gaseous oxygen and the oxide scale forms by the migration of cations and/or anions. In the current application, the environment is LBE which contains dissolved oxygen atoms. In a stationary state, Cr irons would migrate toward the oxide-LBE interface through the oxide layer and ultimately dissolve into LBE. The wt% profile of Cr shown in Figure 4-23 (c) exhibits a slight downward slope toward the oxide/LBE interface, supporting this assumption. On the other hand, oxygen ions migrate through the scale and combine with Cr to form chromium oxide at the metal-oxide interface. The mass transfer process of Cr ions beyond the oxide/LBE interface is not considered here, and only the diffusion of ions and electrons is considered as the rate-controlling process. The current application of Wagner's oxidation theory follows the derivation published in the ASM handbook [10].

For the migration of charged species such as ions and electrons, the chemical and electrical potential gradient together provide the net driving force for their migration. The force, f , acting on a particle, *i*, carrying a charge, z_i, is given by

$$f = -\frac{1}{N_A}\left(\frac{\partial \mu_i}{\partial x} + z_i F \frac{\partial \phi}{\partial x}\right) \text{ [J/m/particle]} \qquad (1)$$

where N_A is Avogadro's number, F is the Faraday constant, $\partial \mu_i / \partial x$ is the chemical potential gradient, and $\partial \phi / \partial x$ is the electrical potential gradient.

Thus, in describing the migration of ions and electrons through a growing oxide layer, a general Nernst-Planck flux form must be used because the flow of such charged species depends on their concentration, mobility, and the driving force for migration:

$$J_i = C_i B_i f = -\frac{C_i B_i}{N_A}\left(\frac{\partial \mu_i}{\partial x} + z_i F \frac{\partial \phi}{\partial x}\right) \tag{2}$$

where C_i is the concentration of species in particles/m^3 and B_i is defined as the absolute mobility of a diffusing species.

From the Nernst-Einstein relationship, the mobility and self-diffusion coefficient are related by:

$$D_i = B_i kT = \frac{B_i RT}{N_A} \tag{3}$$

where R is the gas constant and $k = R / N_A$.

Using Eq. (3), the flux of charged particles are given as follows,

$$J_c = -\frac{C_c D_c}{RT}\left(\frac{\partial \mu_c}{\partial x} + z_c F \frac{\partial \phi}{\partial x}\right) \tag{4}$$

$$J_a = -\frac{C_a D_a}{RT}\left(\frac{\partial \mu_a}{\partial x} + z_a F \frac{\partial \phi}{\partial x}\right) \tag{5}$$

$$J_e = -\frac{C_e D_e}{RT}\left(\frac{\partial \mu_e}{\partial x} + F \frac{\partial \phi}{\partial x}\right) \tag{6}$$

where the subscripts a, c, and e refer to anions, cations, and electrons, respectively.

Because no net current flows through the oxide layer, an electrical neutrality condition is imposed to maintain a local charge balance, as follows

$$z_c J_c + z_a J_a - J_e = 0 \tag{7}$$

By substituting Eq. (4)-(6) into Eq. (7), one can obtain:

$$\frac{\partial \phi}{\partial x} = \frac{1}{F}\frac{-C_c D_c z_c \frac{\partial \mu_c}{\partial x} - C_a D_a z_a \frac{\partial \mu_a}{\partial x} + C_e D_e \frac{\partial \mu_e}{\partial x}}{z_c^2 C_c D_c + z_a^2 C_a D_a + C_e D_e} \tag{8}$$

From the assumption that local thermodynamic equilibrium is established inside the oxide layer, the equilibria for the following reactions between ions, electrons and electrically neutral atoms of metal (Me) and oxygen (X) are established during the process.

$$Me = Me^{z_c+} + z_c e \tag{9}$$

$$X = X^{z_a+} - |z_a| e \tag{10}$$

Then, the chemical potentials for those species can be expressed as:

$$\mu_{Me} = \mu_c + z_c \mu_e \tag{11}$$

$$\mu_X = \mu_a - |z_a| \mu_e \tag{12}$$

Moreover, during isothermal and isobaric process for which the Gibbs-Duhem relation holds:

$$N_{Me} d\mu_{Me} + N_X d\mu_X = 0 \tag{13}$$

Using the previous assumption stating that the oxide has little deviation from stoichiometry, the ratio of molar concentrations can be expressed as:

$$N_{Me} / N_x = |z_a| / z_c \tag{14}$$

and Eq. (13) becomes

$$|z_a| d\mu_{Me} + z_c d\mu_X = 0 \tag{15}$$

From Eqs. (11)-(15), the Eq. (8) can be expressed by:

$$\frac{\partial \phi}{\partial x} = \frac{1}{z_c F}\left(-\frac{\partial \mu_c}{\partial x} + \frac{C_e D_e}{z_c^2 C_c D_c + z_a^2 C_a D_a + C_e D_e} \frac{\partial \mu_{Me}}{\partial x} \right) \tag{16}$$

By considering the nature of metal oxide, an electronic conductor with higher concentration of and diffusivity of electronic defect, Eq. (16) can be reduced further as

$$\frac{\partial \phi}{\partial x} = \frac{1}{z_c F}\left(-\frac{\partial \mu_c}{\partial x} + \frac{\partial \mu_{Me}}{\partial x} \right) = \frac{1}{F} \frac{\partial \mu_e}{\partial x} \tag{17}$$

Thus, the flux equations can be rewritten as simplified forms as following:

$$J_c = -\frac{C_c D_c}{RT} \frac{\partial \mu_{Me}}{\partial x} \tag{18}$$

$$J_a = -\frac{C_a D_a}{RT} \frac{\partial \mu_X}{\partial x} \tag{19}$$

According to Wagner's theory, in an oxide system where defects deviating from stoichiometry are observed in the cation-lattice (either cation-deficient or cation-excess), the activation energy for the oxide growth is the same as the activation energy for diffusion of cations in the oxide, indicating $D_c >> D_a$ [9]. Since Cr oxide is known to have this tendency though being very close

to stoichiometry, the growth of oxide layer is assumed to be solely controlled by the migration of Cr cation. Therefore, the cation flux in Eq. (18) is further considered in detail.

If the concentration of Cr in the oxide scale is C_{Cr} [mol/m^3], the flux of Cr cations is also expressed as

$$J_c = C_{Cr}\frac{dx}{dt} = C_{Cr}\frac{k'}{x} \tag{20}$$

where k' is the parabolic rate constant of $x^2=2k't$.

Eq. (18) can be represented as an internal form with respect to the measurable Cr chemical potentials by setting Me = Cr, μ'_{Cr} (at the metal-oxide interface) and μ''_{Cr} (at the oxide-LBE interface), respectively, i.e.

$$J_c = -\frac{C_c D_c}{RT}\frac{\partial \mu_{Cr}}{\partial x} \cong -\frac{C_c D_c}{xRT}\int_{\mu'_{Cr}}^{\mu''_{Cr}} d\mu_{Cr} \tag{21}$$

where the diffusion coefficient of cation in the oxide is assumed as constant for the chemical potential change. By equating Eqs. (20)-(21),

$$J_c = C_{Cr}\frac{dx}{dt} = C_{Cr}\frac{k'}{x} = -\frac{C_c D_c}{xRT}\int_{\mu'_{Cr}}^{\mu''_{Cr}} d\mu_{Cr} \tag{22}$$

The defect diffusion coefficient (D_c) and the self diffusion coefficient of Cr (D_{Cr}) in oxide are related with each other by the following equation [9]:

$$D_{Cr} = \frac{C_c D_c}{C_{Cr}} \tag{22}$$

The resulting parabolic rate constant for Cr oxidation can be obtained as follows

$$k' = -\frac{C_c D_c}{C_{Cr} RT}\int_{\mu'_{Cr}}^{\mu''_{Cr}} d\mu_{Cr} = -\frac{D_{Cr}}{RT}\left(\mu''_{Cr} - \mu''_{Cr}\right) \approx D_{Cr}\ln\left(\frac{X'_{Cr}}{X''_{Cr}}\right) \tag{23}$$

where $\mu_{Cr} = \mu^0_{Cr} + RT\ln a_{Cr} \approx \mu^0_{Cr} + RT\ln X_{Cr}$, X'_{Cr} is the mole fraction of Cr at the metal-oxide interface and X''_{Cr} is the mole fraction of Cr at the oxide-LBE interface.

If experimental results for Fe-18wt%Cr from Figure 4-27(b) are used, the values are given as X'_{Cr} = 0.1908 and X''_{Cr} =0.1642. From Figure 4-1, using x = 16.89μm = 16.89×10^{-6} m after 500 hours (1.8×10^6 sec), k' is obtained as 7.924×10^{-17} m^2/sec. From Eq. (23), the diffusion coefficient of Cr is calculated as 5.28×10^{-16} m^2/sec. It is smaller than the grain boundary

diffusion coefficient of Cr in α-Fe at 600°C (5.419×10^{-15} m^2/sec) but higher than the lattice diffusion coefficient of Cr in α-Fe at 600°C (9.496×10^{-19} m^2/sec) [10]. Comparison with other diffusion coefficients listed in Chapter 2 is shown in Figure 4-2. This high value of Cr diffusion coefficient can be explained postulating that the grain boundary diffusion was dominant as suggested by the Fe-9 & 12 wt% Cr results, showing that the oxygen diffusion might have been enhanced as reported by Kuroda et al.[7]

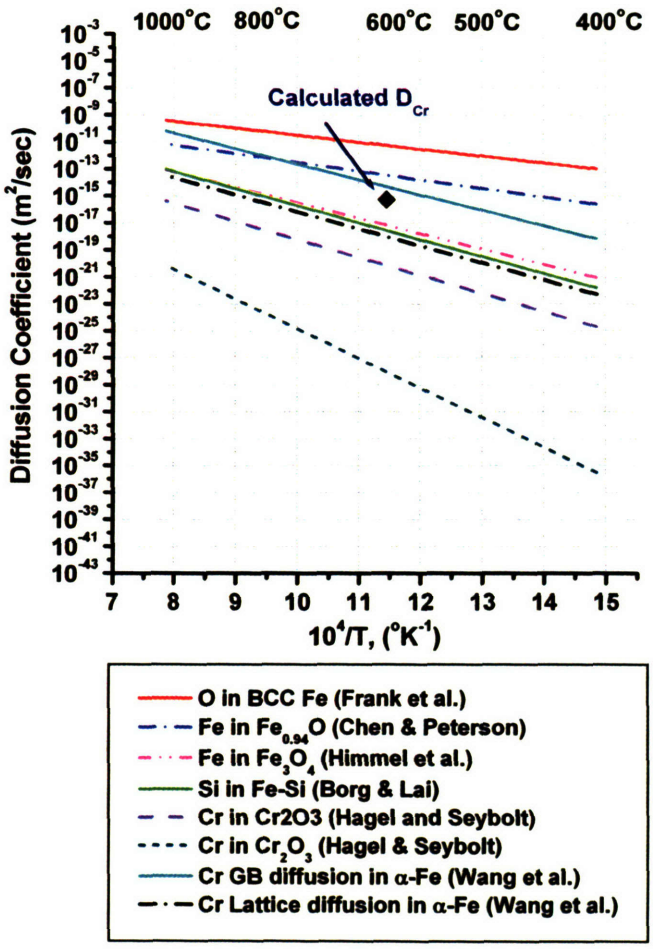

Figure 5-2. Comparison between the reported diffusion coefficients and the calculated diffusion coefficient of Cr in $(Fe,Cr)_2O_3$ oxide formed in Fe-18wt% Cr after 500-hour exposure at 600°C.

begins to serve as an effective diffusion barrier preventing further oxidation, the decrease in the interaction layer can be observed as such.

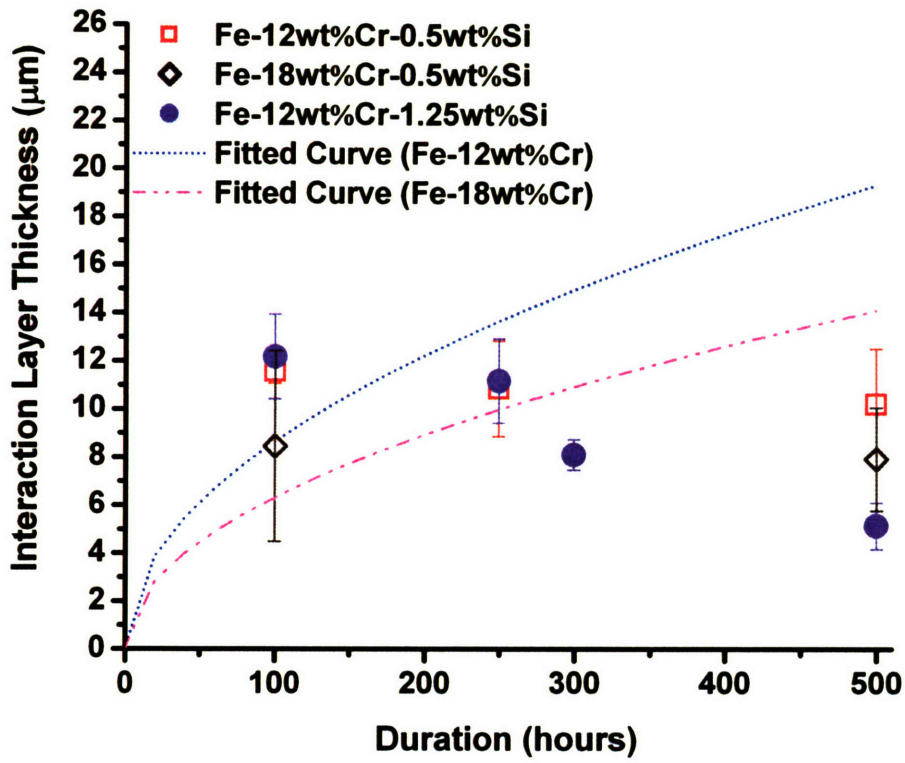

Figure 5-3. The growth of interaction layer thickness on Fe-Cr-Si with high Cr content compared to the parabolic rate fitting curves of Fe-12wt%Cr and Fe-18 wt% Cr.

Still, the extensive internal/grain boundary oxidation observed in the Fe-Cr-Si alloys containing only 2.25wt%Cr has not been accounted for in comparison to the Fe-Cr-Si alloys of higher Cr (>12wt%) showing the formation of a stable Cr-rich oxide on the top as well as Si-oxide network at the oxide/base metal interface as an effective diffusion barrier. To understand this discrepancy, it is necessary to re-visit the internal oxidation analysis performed in the previous section. As discussed earlier, the significant depth of internal/grain boundary oxidation resulted from the high oxygen diffusivity and its concentration at the surface, combined with the low concentration of active elements for oxidation in the alloy. In the case of Fe-Cr-Si alloys with high (>12wt%) Cr concentration, the fast diffusion of Cr forming Cr-rich oxide layer reduces surface the oxygen concentration from the value corresponding to that of FeO (low Cr

dominant process of oxidation under the testing condition is grain boundary diffusion. Therefore, the internal oxidation phenomena in Fe-Si alloys and (2.25wt%Cr) Fe-Cr-Si alloys can be regarded as a combined process of grain boundary diffusion as well as lattice diffusion including lateral diffusion connecting the precipitate network.

To understand relevant parameters concerning the observed internal oxidation, it is illustrative to further analyze the internal/grain boundary oxidation processes of Fe-Si and (2.25wt%Cr) Fe-Cr-Si alloys using the internal oxidation theory finalized by Rapp [12]. Although it is only applicable to an exclusive internal oxidation case in which the absence of any external layer is guaranteed, the current internal/grain boundary oxidation process can be treated as such because the external oxide layer formed at the very initial stages of exposure to LBE was incomplete and de-stabilized well before 100 hours. The following derivation for the internal oxidation process follows that by Rapp [13] and is applied for a planar specimen geometry using the quasi-steady state approximation.

In the absence of an external oxide scale and under diffusion controlled conditions, the depth, ξ, if the internal oxidation zone is a parabolic function of the time t, so that

$$\xi = 2\gamma(D_O t)^{1/2} \tag{24}$$

and the velocity of reaction front motion is

$$\frac{d\xi}{dt} = \gamma\left(\frac{D_O}{t}\right)^{1/2} \tag{25}$$

where D_O is the diffusion coefficient of oxygen in the base metal and γ is a dimensionless parameter which will be determined later. The parameter γ is assumed to be independent of time for isothermal oxidation at constant oxygen pressure.

Assuming that precipitated particles do not interfere with the diffusion of oxygen in the base metal, the diffusion equation for the one-dimensional diffusion of oxygen is expressed by Fick's second law as

$$\frac{\partial N_O}{\partial t} = D_O \frac{\partial^2 N_O}{\partial x^2} \tag{26}$$

with the boundary conditions

$$N_O = N_O^{(S)} \text{ for } x = 0,\ t > 0$$
$$N_O = 0 \quad \text{for } x \geq \xi, t > 0$$

where x is the distance from the outer surface, N_O is the mole fraction of oxygen in the base metal, and $N_O^{(S)}$ is the mole fraction of oxygen at the external surface.

The solution of Eq.(26) obtained by Rapp is

$$N_O(x,t) = N_O^{(S)}\left\{1 - \frac{\operatorname{erf}\left[x/2(D_O t)^{1/2}\right]}{\operatorname{erf}\gamma}\right\} \tag{27}$$

where erf is the error function.

Similarly, Fick's second law for the counter-diffusion of less noble alloying element, B, is

$$\frac{\partial N_B}{\partial t} = D_B \frac{\partial^2 N_B}{\partial x^2} \tag{28}$$

with the boundary conditions

$$N_B = N_B^{(0)} \text{ for } x > 0,\ t = 0$$
$$N_B = 0 \text{ for } x \leq \xi, t > 0$$

where D_B is the diffusion coefficient of B, N_B is the mole fraction of B, and $N_B^{(0)}$ is the mole fraction of B in the bulk alloy.

The solution to Eq. (28) becomes

$$N_B(x,t) = N_B^{(0)}\left[1 - \frac{\operatorname{erfc}\left(x/2(D_B t)^{1/2}\right)}{\operatorname{erfc}\left(\theta^{1/2}\gamma\right)}\right] \tag{29}$$

where $\theta = D_O / D_B$ and erfc is the complementary error function.

At the precipitation front of the internal oxidation zone, if an insoluble and stoichiometric oxide particle is precipitated, the flux of oxygen atoms arriving from the external surface must be equivalent to the flux of B atoms arriving from the bulk alloy, so that,

$$\lim_{\varepsilon \to 0}\left[-D_O\left(\frac{\partial N_O}{\partial x}\right)_{x=\xi-\varepsilon} = \nu D_B\left(\frac{\partial N_B}{\partial x}\right)_{x=\xi+\varepsilon}\right] \tag{30}$$

where ν is the stoichiometric ratio of oxygen to metal atoms in the oxide precipitate.

Substitution of Eqs. (27) and (29) into Eq. (30) yields

$$\frac{N_O^{(S)}}{N_B^{(0)}} = \frac{\nu \exp(\gamma^2)\operatorname{erf}(\gamma)}{\theta^{1/2}\exp(\gamma^2\theta)\operatorname{erfc}(\gamma\theta^{1/2})} \tag{31}$$

whereby the parameter γ may be obtain from a graphical or numerical solution.

If the following limiting case relationship is valid,

$$\frac{D_B}{D_O} << \frac{N_O^{(S)}}{N_B^{(0)}} << 1 \tag{32}$$

Eq. (31) may be simplified to

$$\gamma \approx \left[\frac{N_O^{(S)}}{2\nu N_B^{(0)}}\right]^{1/2} \tag{33}$$

whereupon Eq. (1) becomes

$$\xi \approx \left[\frac{2N_O^{(S)} D_O t}{\nu N_B^{(0)}}\right]^{1/2} \tag{34}$$

If a second limiting case is valid as following,

$$\frac{N_O^{(S)}}{N_B^{(0)}} << \frac{D_B}{D_O} << 1 \tag{35}$$

then Eq. (31) becomes

$$\gamma \approx \left[\frac{\pi^{1/2}\theta^{1/2} N_O^{(S)}}{2\nu N_B^{(0)}}\right] = \left[\left(\frac{D_O}{D_B}\right)^{1/2} \cdot \frac{\pi^{1/2} N_O^{(S)}}{2\nu N_B^{(0)}}\right] \tag{36}$$

and Eq.(1) is obtained as

$$\xi \approx \left[\frac{\pi^{1/2} D_O N_O^{(S)} t^{1/2}}{\nu (D_B)^{1/2} N_B^{(0)}}\right] \tag{37}.$$

In an effort to compare with the current experimental results, Fe-1.25wt% Si (2.45 at% Si) was chosen (as element B = Si), since its low Si at% can discourage continuous SiO_2 layer formation, and almost completely detached external oxide layer after 300-hour exposure was observed as can be seen in Figure 4-31. Although the expected Si precipitates in the internal oxidation zone are in the form of Fe_2SiO_4 and/or SiO_2, the more stable oxide of SiO_2 (ν=2) formation would be assumed. From the literature data for diffusion coefficients, as listed in Chapter 2, the following values are calculated: $D_O = D_{O\ in\ BCC\ Fe} = 5.59\times10^{-12}$ m/sec^2 and $D_{Si} = D_{Si\ in\ Fe\text{-}Si} = 6.934\times10^{-18}$ m/sec^2 at 600°C. Although the expected oxygen content in LBE, controlled by the ratio of $P(H_2)/P(H_2O)$, was 2.96×10^{-9} at% ($N_O^{(S)} = 2.96\times10^{-11}$), the presence of

iron oxides on the surface of tested samples made the $N_O^{(S)}$ value significantly higher than that. To explain the deeper internal oxidation zone size than expected, the maximum value of $N_O^{(S)}=3.16\times10^{-8}$ at 600°C [12] is chosen to use by assuming the mole fraction of oxygen on the surface is in equilibrium with FeO, based on the detection of remnant iron oxides on the surface, though being incomplete. FeO is selected because it is the innermost oxide layer when multiple iron oxides are formed. In this case, along with $N_{Si}^{(0)}=0.0245$,

$$\frac{D_{Si}}{D_O} << \frac{N_O^{(S)}}{N_{Si}^{(0)}} << 1 \tag{38}$$

Thus, using Eq. (33) to calculate only the internal oxidation zone size, ξ is estimated as 2.8 μm after 300-hour ($=1.08\times10^6$ sec) exposure. Therefore, a considerable discrepancy can be observed even with the assumption of maximum $N_O^{(S)}$, because the experimentally measured internal oxidation zone depth is $\xi = 10.4$ μm and the grain boundary oxidation depth is $\xi_{GB}=35.7$ μm. However, this more extended depth of internal oxidation zone can not be a result of higher $N_O^{(S)}$, because in such cases, a thick, stable external iron oxide films would have been detected on the surface without the extensive internal/grain boundary oxidation. Therefore, it must be concluded that the observed phenomena of extensive internal/grain boundary oxidation resulted from a diffusion coefficient of oxygen much higher than that used in the calculation. If so, the lattice diffusion coefficient of oxygen, D_O, in Eq. (34) needs to be replaced with the effective diffusion coefficient [14], D_{eff}, as following,

$$D_{eff} = D_O + (3\delta / s)D_{GB} \tag{39}$$

where δ is the width of grain (~1 nm) and s is the grain size of this material (82μm). Then, in the case of $\xi_{GB}=35.7$ μm, the grain boundary diffusion coefficient of oxygen, D_{GB} is obtained as 2.46×10^{-5} m^2/s. The similar explanation may be applied to Fe-Cr-Si with low Cr (2.25wt%) concentration (2.25wt%) which only showed a prominent internal/grain boundary oxidation phenomena without forming any protective layer on its surface.

A key point to be made in this section is that the depth of the internal/grain boundary oxidation zone increases with the surface oxygen concentration and the diffusion coefficient of

oxygen, while it is inversely related to the concentration of more active element and its diffusion coefficient. Therefore, when there is not enough concentration of more active element for external oxide formation in the alloy, the internal/grain boundary oxidation takes place to a great extent as a result. This observation will be re-visited in the next section while examining the high Cr alloyed Fe-Cr-Si alloys.

5.1.3 Effect of Si (Fe-Cr-Si with high Cr alloys)

There are common features among Fe-Cr-Si alloys containing high Cr associated with the behavior of interaction layer growth. Figure 5-3 represents the growth of interaction layer and depicts the reduction in the layer thickness with exposure time for Fe- 12wt%Cr-0.5wt%Si, Fe-18wt%Cr-0.5wt%Si and Fe-12wt%Cr-1.25wt%Si alloys. For comparison purposes with Fe-Cr alloys without Si, the fitted parabolic rate curves of Fe-12wt%Cr and Fe-18wt%Cr are shown along with the alloys specified above. Upon initial exposure up to 100 hours at 600°C, the (< 12wt% Cr) Fe-Cr-Si alloys formed interaction layers comparable in thickness to those formed on Fe-Cr alloys. On further exposure, the reduction of layer thickness was observed for all Fe-Cr-Si alloys with Cr content above 12wt%. Fe-12wt%Cr-1.25wt%Si showed the most reduced in the interaction layer thickness after 500-hour exposure, with Fe-12wt%Cr-0.5wt%Si the least. This can be explained as a result of the formation and the enrichment of Si and Cr-containing oxide precipitates at the interface of the oxide and the base metal, as evidenced from EDX analysis as shown in Figure 4-38. Therefore, the progressive formation of Fe_2SiO_4 and/or SiO_2 precipitates underneath Cr_2O_3 oxides may have played a major role in the reduction of interaction layer thickness by blocking the additional diffusion of Fe and Cr from adjoining the oxide layer. Since the process of forming Fe_2SiO_4 and/or SiO_2 precipitates at the oxide/metal interface is very slow, other elements can still diffuse through the interface. Moreover, due to a high interdiffusion coefficient in the Fe-Cr alloy, as well as the presence of short diffusion path aided by the grain boundaries, the Cr-rich oxide layer grows faster than Si-oxide layer. This explains the initial oxide growth rate comparable to that of Fe-Cr. While a Si-oxide network is being formed slowly at the interface of the oxide and the base metal, the dissolution of elements still takes place at the surface of the oxide in contact with LBE. When the Si-oxide network formed at the interface

begins to serve as an effective diffusion barrier preventing further oxidation, the decrease in the interaction layer can be observed as such.

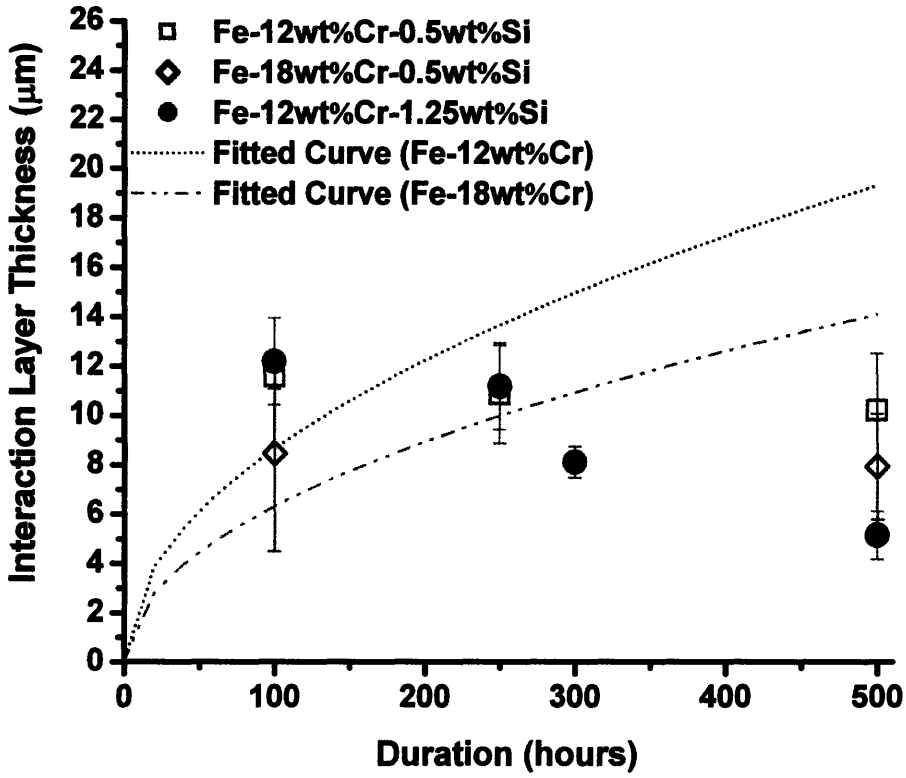

Figure 5-3. The growth of interaction layer thickness on Fe-Cr-Si with high Cr content compared to the parabolic rate fitting curves of Fe-12wt%Cr and Fe-18 wt% Cr.

Still, the extensive internal/grain boundary oxidation observed in the Fe-Cr-Si alloys containing only 2.25wt%Cr has not been accounted for in comparison to the Fe-Cr-Si alloys of higher Cr (>12wt%) showing the formation of a stable Cr-rich oxide on the top as well as Si-oxide network at the oxide/base metal interface as an effective diffusion barrier. To understand this discrepancy, it is necessary to re-visit the internal oxidation analysis performed in the previous section. As discussed earlier, the significant depth of internal/grain boundary oxidation resulted from the high oxygen diffusivity and its concentration at the surface, combined with the low concentration of active elements for oxidation in the alloy. In the case of Fe-Cr-Si alloys with high (>12wt%) Cr concentration, the fast diffusion of Cr forming Cr-rich oxide layer reduces surface the oxygen concentration from the value corresponding to that of FeO (low Cr

case) to the value corresponding to that of Cr_2O_3 (high Cr case). Therefore, the depth of internal oxidation is reduced greatly to facilitate only a localized SiO_2 precipitate formation, which consequently takes place beneath the Cr_2O_3 containing oxide layer. From this viewpoint, the main effect of Si being a diffusion barrier in high Cr Fe-Cr-Si alloys can be regarded as a result of the formation of Cr-containing oxide at the oxide/alloy interface, providing low oxygen concentration to promote a localized Si-oxide network in association with Eq. (33) and (37). Therefore, in order for the Si oxide network to serve as an effective diffusion barrier, the alloy should contain sufficient Cr concentration. In the present research, the apparent concentration of Cr needed to promote such synergetic effect with Si is observed as 12wt%.

In the same vain, it is clear that the increase in Si and Cr content in alloy will result in more reduced interaction layer thickness. However, with respect to Fe-18wt%Cr-1.25wt%Si and Fe-18wt%Cr-2.55wt%Si, the formation of a very thin interaction layer is rather a result of a large grain size, which separates grain boundaries further apart, making lattice diffusion as a major process of oxidation. At the same time, the high Cr and Si concentrations of both alloys might have played an important role by forming an efficient SiO_2 layer to block further oxidation. From the result shown in Figure 4-54, displaying the internal/grain boundary oxidation zone as well as a thin surface oxide layer observed in a sample of smaller grain size but with the same composition of Fe-18wt%-2.55wt%Si, the role of grain boundaries in the diffusion process can be again emphasized under present experimental condition.

5.2 Summary of Experimental Results

- For the conditions of this study, the oxygen control in the cover gas proved to be successful based on the observed oxidation behavior of a Fe-18wt%Cr-2.55wt%Si (forming only Cr_2O_3 and SiO_2 oxides) and a pure Fe specimens.

- The initial actual oxygen concentration in the LBE was in a transient state during the very initial stages of exposure because of residual oxygen in the system. Nevertheless, the observed kinetic processes on the interaction layer formation for the Fe-Cr and Fe-Cr-Si alloys (containing more than 9wt% Cr) were not affected by this initial condition, due to

the fast diffusion of Cr facilitated by its high activity in the alloy. Moreover, this situation provided some insights on the stability on the relevant oxide systems, by simulating a failure situation in the oxygen control system where the iron based oxide cannot sustain its protectiveness.

- The oxide forming process consists of a two-dimensional diffusion process, a combination of grain boundary diffusion with lateral diffusion.

- Low Cr alloyed (1~2.25wt%Cr) Fe-Cr alloys formed a duplex oxide scale of outer iron oxides and inner Cr containing oxides. Both oxides did not prevent LBE penetration from occurring under the present experimental condition.

- Increase in Cr concentration changes the mode of oxidation to the formation of a Cr-rich spinel or Cr_2O_3 oxide. Particles can precipitate in the internal oxidation zone. This phenomenon is observed in Fe-9wt%Cr and Fe-12wt%Cr. However, the surface oxide formed on the Fe-9wt%Cr did not provide adequate protection from the LBE penetration. The threshold Cr content when it is alloyed alone to Fe to prevent LBE penetration appeared to be 12wt%.

- A higher Cr concentration results in the further change in the oxide composition and morphology to incorporate the higher Cr activities in the alloy. Fe-18wt%Cr alloy showed a single oxide layer composed of Fe_2O_3-Cr_2O_3 solid solution $(Fe,Cr)_2O_3$.

- Alloying only Si to Fe developed internal/grain boundary oxidation zone without a detectable, continuous SiO_2 layer even in a Fe-3.82wt%Si alloy with Si concentration above the known threshold.

- There is a threshold Cr concentration for the synergetic effect of Si addition to be made possible. In Fe-Cr alloy with low Cr concentration, only internal/grain boundary oxidation was observed without providing any diffusion barrier to retard further transport in materials. However, with the higher Cr (>12wt%) concentration in an Fe-Cr-Si alloy,

the Si can serve as an efficient diffusion barrier by forming localized Si-oxide network beneath the Cr-rich oxide layer.

- The parabolic reaction rate constant becomes smaller with Cr addition (>9wt%) to Fe. But continuous growth in the interaction layer thickness was observed over time, as an indication of a continued diffusion process taking place for the relevant species to join the oxide.

- With addition of Si to higher Cr (>12wt%) Fe-Cr alloys, the reduction of interaction layer thickness was observed during the time of exposure, indicating that the transport of the elements in the base metal to the surface oxide through the interface between the oxide/the base metal was discouraged by the Si oxide network.

5.3 References

[1] N. Birks and G.H. Meier, Introduction to High Temperature Oxidation of Metals, Edward Arnold, 1983.

[2] D. Talbot, Corrosion Science and Technology, CRC, Boca Raton, 1998.

[3] A. U. Seybolt, "Observations on the Fe-Cr-O System" *Journal of the Electrochemical Society*, **107** (1960) pp.147-156.

[4] W. W. Smeltzer and D. P. Whittle, "The Criterion for the Onset of Internal Oxidation Beneath the External Scales on Binary Alloys", *Journal of the Electrochemical Society*, **125** (1978) pp.1116-1126.

[5] P. A. Labun et al., "Microstructural Investigation of the Oxidation of an Fe-3Pct Cr Alloy", *Metallurgical Transactions A*, **13A** (1982) pp.2103-2112.

[6] F. H. Stott, "Influence of Alloy Additions on Oxidation", *Materials Science and Technology*, **5** (1989) pp.734-740.

[7] K. Kuroda et al., "Oxide-Formation Characteristics in the Early Stages of Oxidation of Fe and Fe-Cr Alloys", *Oxidation of Metals*, **19** (1983) pp.117-127.

[8] Cited in [12] as C. Wagner, "Contributions to the Theory of the Tarnishing Process", *Z. Phys. Chem.*, B21 (1933) pp. 25–41.

[9] A. Atkinson, "Transport Processes during the Growth of Oxide Films at Elevated Temperature", *Reviews of Modern Physics*, **57** (1985) pp.437-470.

[10] M. Danielewski, "Kinetics of Gaseous Corrosion Processes", Corrosion: Fundamentals, Testing, and Protection, Vol 13A, *ASM Handbook*, ASM International, 2003, p 97–105.

[11] Z. B. Wang, et al., "Diffusion of Chromium in Nanocrystalline Iron Produced by Means of Surface Mechanical Attrition Treatment", *Acta Materialia*, **51** (2003) pp.4319-4329.

[12] A. Atkinson, "A Theoretical Analysis of the Oxidation of Fe-Si Alloys", *Corrosion Science*, **22** (1982) pp.87-102.

[13] R. A. Rapp, "Kinetics, Microstructures and Mechanism of Internal Oxidation-Its Effect and Prevention in High Temperature Alloy Oxidation" *Corrosion*, **21** (1965) pp.382-401.

[14] R. W. Balluffi, S. M. Allen and W. C. Carter, Kinetics of Materials, John Wiley & Sons, 2005.

CHAPTER 6

CONCLUSIONS AND FUTURE WORK

6.1 Overall Summary

A set of alloys based on the Fe-Cr-Si system have been developed that provide protection from accelerated corrosion in liquid Pb alloys over a wide range of oxygen potentials. This protection is achieved, on the one hand, by the formation of a protective film with a dual structure (Cr-oxide/Si-oxide) for Cr concentrations above 12 wt% and Si concentrations above 2.55wt% at oxygen potentials above the potential for the formation of these oxides. Protection is achieved at very low oxygen potentials (below the oxide formation potentials) by the enrichment of the surface in Si, a slowly dissolving, low solubility element.

The choice of this alloy system and the resulting investigations on the corrosion and mitigation mechanisms of iron based alloys in contact with high temperature lead-bismuth eutectic (LBE) was motivated by the critical need for developing advanced alloy systems for use of high temperature service. In an effort to achieve the goal, experimental studies on iron based materials alloyed with Cr and/or Si have been proposed as an effective interim approach, which minimizes the technical risks and complications associated with other alloys and exotic materials at the same time takes full advantage of the best known qualities of iron-based materials.

With the proposed model alloys based on iron, the corrosion and protection mechanisms in relation to the alloying effect of Cr and Si were investigated. In an effort to encourage accelerated corrosion processes, the experimental condition was best optimized for high temperature and low oxygen partial pressure environment.

As expected from the characteristics of iron oxides, they should not be regarded as protective, because of either their high temperature instability (wüstite transformation processes) or the potential for low oxygen partial pressure in the system making thermodynamic conditions

unfavorable for them. Without being affected by the failure in iron oxides, an increased corrosion resistance is observed with increase in Cr concentration in Fe-Cr alloys. The threshold Cr content of alloys in order to protect the base metal from eminent LBE penetration is observed as 12 wt% in Fe-Cr alloys. Such protection of the base metal is achieved by the formation of Cr rich Fe-Cr spinel oxide aided by the short circuit diffusion paths through the grain boundaries. Further increase in Cr concentration in alloy results in the change in oxide structure and composition, to accommodate the increased Cr_2O_3 concentration in the oxide. Fe-Cr-Si alloyed with high Cr (>12wt%) showed a marked reduction in the interaction layer thickness with increase in the exposure duration, indicating the role of Si serving as an effective diffusion barrier only when it is combined with sufficient Cr concentration in the alloy.

6.2 Conclusions

The primary objective of this study was to identify the key material issues encountered in the liquid Pb-alloy technology, and to demonstrate the feasibility of developing a new alloy system which is capable of use at high temperature service. In an effort to achieve the goal, comprehensive surveys on the possible material systems and the available corrosion mitigating techniques were conducted. Based on that initial evaluation and considering the fundamentals of alloy development and protective scale formation, iron based model alloys have been developed with a strong emphasis on the protective oxide formation in relation to the Cr and Si addition. The overall research goal was achieved by identifying the role of each element in terms of improving corrosion resistance of the base material through a high temperature testing with lead-bismuth eutectic under accelerated corrosion environment. An improved understanding of the kinetic process and its dependence on alloying elements was achieved.

6.3 Contributions

The work presented in this thesis established the basis and design guidelines for future development of advanced materials for the high temperature liquid Pb-alloy service, by demonstrating the feasibility of alloying elements optimization in a way to increase the corrosion

resistance of the base material. ***An alloy system was proposed, and then verified that allows for an increase in the operating temperature of Pb-alloy systems.***

The contributions of the present work include the following specific achievements:

- Conducted a thorough characterization of liquid Pb-alloy corrosion and mitigation mechanisms from the study of thermodynamic and kinetic aspects.
- Confirmed the effectiveness of oxygen control method which is crucial to the corrosion mitigating strategy.
- Identified key alloying elements to be used to increase the corrosion resistance of the base metal in high temperature liquid Pb-alloys.
- ***Proposed and developed a series of alloys based on the Fe-Cr-Si system that are resistant to corrosion in liquid Pb alloys.***
- Performed high temperature corrosion testing on the model alloys to assess their resistance to LBE corrosion under the accelerated corrosion environment.
- ***Verified the expected corrosion behavior improvement of these alloys***
- Identified and analyzed the change in the interaction modes of iron based model alloys in terms of their alloying elements effect.
- Identified the underlying mechanisms governing the corrosion resistance of Fe-Cr-Si alloys with respect to the Cr and/or Si compositions.

6.4 Future Work

This thesis represents comprehensive research effort to verify the feasibility of developing advanced alloys to be used for high temperature liquid Pb-alloy service, to take advantage of all the benefits of the coolants system while satisfying economic viability and overall system integrity. As such it should be viewed a solid foundation for future work.

Given the limitations of experimental study, associated with the limited dissolution process and the absence of enhanced material transport as a part of the testing regime, the time dependent behavior of the interaction layers may appear different in systems having actual mass transfer capability associated with a thermal gradient in the system. Future efforts should be focused on

longer term testing under such operational environment to fully assess the stability of protective films in terms of the materials' corrosion resistance.

The alloy development effort in this thesis has focused on the optimization of corrosion resistance. No effort has been made to address mechanical properties. In fact, it is a certainty that the strength of these alloys will be very low compared to current Fe-based structural materials. Thus, the application of the alloys developed in this thesis would be as a part of a functionally graded composite material in which the corrosion resistant material is used as a coolant-facing layer on top of a higher strength structural material. The developed alloys are perfectly suited for use as welding electrodes used to weld overlay such a layer. Also, using these alloys as a co-extruded cladding material either as the outer layer on a fuel pin or the inner clad on a system pipe can easily be achieved.

An additional limitation was associated with the time of exposure. While the exposure times were sufficient to develop a good "handle" on the effect of time on film thickness, exposures of several thousand hours are necessary for competent extrapolation to relevant system life cycle times. Additionally, longer exposure times would allow an evaluation of the overall stability of Si-based oxide films which, under some circumstances, can become non-adherent during high oxygen concentration, gas phase exposure at high temperatures where even a Si-based oxide may become quite thick.